CRISPR Interference Screening and Pharmacological Targeting of Sodium Channels in Triple-Negative Breast Cancer Cells

Rachael Moore

MSc by Research

University of York
Biomedical Sciences
Biology

June 2025

Abstract

Hypoxia is linked with more invasive forms of breast cancer, particularly triple negative breast cancer (TNBC). Elevated intratumoural sodium (Na^+) level in patients correlates with disease severity and Na^+ reduction predicts treatment response. Our *in vivo* data, using $^{23}Na^+$ MRI, suggest that the majority of this Na^+ is intracellular, implicating specific Na^+ channels and transporters in its accumulation and regulation in the tumour microenvironment. While hypoxia has been shown to upregulate various Na^+ channels, their combined involvement in hypoxia-driven breast cancer progression remains unclear.

Here, we performed the first systematic screen to identify Na^+ channels which support TNBC proliferation under hypoxia. Using a targeted CRISPR interference (CRISPRi) screen with a dCas9-KRAB transcriptional repression system, we repressed 181 Na^+ channel and transporter genes in two TNBC cell lines, MDA-MB-231 and MDA-MB-468, cultured under normoxic or hypoxic conditions for 7 days. The screen identified hypoxia-specific depletion of guide RNAs (gRNAs) targeting *SCN5A* (Nav1.5), *SLC10A5*, *SLC38A5*, and *SLC34A2* in MDA-MB-231 cells, and *GRIN3A*, *SLC22A12*, and *SLC34A3* in MDA-MB-468 cells. *FXYD5* was also exclusively depleted under hypoxia in both cell lines.

To evaluate the therapeutic potential, we tested the $Na_v1.5$ channel as a target in TNBC cells using propafenone, a clinically approved antiarrhythmic drug not previously studied in the cancer context. Electrophysiological analysis confirmed that propafenone (100 μM) significantly inhibited Na^+ currents in MDA-MB-231 cells.

Our findings highlight multiple Na^+ transporters involved in TNBC proliferation under hypoxia, with *SCN5A*/Nav1.5 as a promising therapeutic target in hypoxic TNBC. These results support the potential repurposing of existing Na^+ channel-targeting drugs to inhibit hypoxic TNBC progression.

Table of Contents

1. Introduction 15

1.1 Breast cancer 15

1.2 Hypoxia in TNBC 17

1.3 Na+ in breast cancer 21

1.3.1 Na+ homeostasis 21
1.3.2 Na^+ Channel expression in breast cancer 21
1.3.3 VGSC structure and subtypes 23
1.3.4 Functional consequences of Na^+ channel upregulation 25

1.4 Effect of Hypoxia on Na^+ transport in breast cancer 27

1.5 Therapeutic targeting of VGSCs in cancer 29

1.6 Propafenone 30

1.7 Hypothesis and aims 33

2. Materials and methods 34

2.1 Cell culture and hypoxic incubations 34

2.2 Freezing and thawing Cells 34

2.3 Pharmacology 35

2.3.1 Puromycin 35
2.3.2 Hygromycin 35
2.3.3. Propafenone 35

2.4 Determination of selection concentrations 37

2.5 Lentiviral transduction 37

2.5.1 Control lentivirus 37
2.5.2 dCas9-KRAB lentivirus 38
2.5.3 gRNA Library Lentivirus 38
2.5.4 Hypoxia screen 39

2.6 MOI determination by flow cytometry analysis of transduction efficiency 44

2.7 Fluorescence-activated cell sorting (FACS) of dCas9/KRAB-transduced cell lines 44

2.8 Microscopy 45

2.9 DNA extraction 46

2.10 PCR amplification **46**

2.11 Electrophoresis **49**

2.12 Library preparation and sequencing **49**

2.13 Electrophysiology **50**

2.13.1 Whole-cell patch-clamp recording 50
2.13.2 Voltage clamp protocols 50

2.14 Data and statistical analysis **51**

2.14.1 CRISPRi screen analysis 51
2.14.2 Statistical analysis 52

3. Results ***54***

3.1 Generating a target list of Na+ channel genes for a pooled gRNA library **54**

3.2 Establishing dCas9-KRAB expressing cell lines **54**

3.3 Transfection with gRNA library **62**

3.4 Selection under hypoxia **64**

3.5 Quality control report for the CRISPRi screen **64**

3.6 Depleted gRNAs under hypoxia in MDA-MB-231 ..... **68**

3.7 Depleted gRNAs under hypoxia in MDA-MB-468 ..... **76**

3.8 Clinical relevance **83**

3.9 Effect of propafenone on transient Na^+ current **86**

3.10 Effect of propafenone on persistent Na^+ current **86**

3.11 Effect of propafenone on voltage-current relationship **91**

3.12 Effect of propafenone on activation and inactivation kinetics **93**

4. Discussion ***94***

4.1 Summary of main findings **94**

4.2 Key CRISPRi screen findings **94**

4.2.1 Identification of Na^+ transporters which contribute to MDA-MB-231 cell proliferation under hypoxia 94
4.2.2 Fewer Na^+ transporters identified as contributor to MDA-MB-468 cell proliferation under hypoxia 97
4.2.3 Clinical relevance 98

4.3 *SCN5A* and TNBC cell proliferation under hypoxia **98**

4.4 Technical strengths and limitations **99**

4.4.1 gRNA representation and control performance 99
4.4.2 Timing of hypoxic culture 100
4.4.3 Cell line-specific effects 102

4.5 Pharmacological inhibition of $Na_V1.5$ with propafenone **102**

4.6 Future directions **103**

4.7 Clinical significance and conclusions **104**

References ***106***

Supplementary figures ***133***

List of tables

Table 2.1. The drugs utilised in this project. 36
Table 2.2. Lentiviral vectors utilised in this project. 40
Table 2.3. PCR primers utilised in this project. 48
Table 3.1. Effect of propafenone on Na^+ current characteristics in MDA-MB-231 cells. 89
Supplementary Table 1. Guide RNA library for CRISPRi screen 139

List of figures

Figure 1.1. Regulation and downstream effects of HIF-1α signalling in TNBC. 20
Figure 1.2. Na^+ channels and transporters. 22
Figure 1.3. Topology and architecture of mammalian Na_V channels. 24
Figure 1.4. Chemical structure of propafenone. 32
Figure 2.1. Plasmid map of the lentiviral expression vector pLV[Exp]-EGFP/Puro-CMV>dCas9/KRAB (VectorBuilder ID: VB900088-2936zvb). 41
Figure 2.2. Plasmid map of the lentiviral vector from the gRNA CRISPRi library (VectorBuilder ID: Lib231220-2041kcc). 42
Figure 2.3. Schematic overview of the CRISPRi screen workflow. 43
Figure 3.1. Dose-response experiments of puromycin. 57
Figure 3.2. Transduction efficiency with eGFP/mCherry control lentivirus. 58
Figure 3.3. FACS of dCas9/KRAB-expressing cell lines. 59
Figure 3.4. Established dCas9-KRAB cell lines. 60
Figure 3.5. dCas9-KRAB-expressing cell line validation. 61
Figure 3.6. Dose-response experiments of hygromycin. 63
Figure 3.7. FastQC analysis. 66
Figure 3.8. gRNA deviation vs. ranked SD. 67
Figure 3.9. Control gRNA depletion and enrichment in MDA-MB-231. 71
Figure 3.10. CRSIPR screen results in MDA-MB-231 considering all gRNAs. .. 72
Figure 3.11. CRSIPR screen results in MDA-MB-231 using top depleted gRNA. 73
Figure 3.12. Genes selectively depleted under hypoxia in MDA-MB-231. 74
Figure 3.13. Comparison of gRNA depletion between hypoxia and normoxia in MDA-MB-231 cells. 75
Figure 3.14. CRSIPR screen results in MDA-MB-468 considering all gRNAs. .. 78
Figure 3.15. Control gRNA depletion and enrichment in MDA-MB-468. 79
Figure 3.16. CRSIPR screen results in MDA-MB-468 using top depleted gRNA. 80
Figure 3.17. Genes selectively depleted under hypoxia in MDA-MB-468. 81
Figure 3.18. Comparison of gRNA depletion between hypoxia and normoxia in MDA-MB-468 cells. 82

Figure 3.19. Kaplan-Meier survival curves. 85
Figure 3.20. Effect of propafenone on Na^+ currents. 88
Figure 3.21. Dose-dependent inhibition of Na^+ currents by treatment with propafenone (1, 3, 10, 30, 100 µM). 90
Figure 3.22. Effect of propafenone on the current-voltage relationship. 92
Supplementary Figure 1. Flow Cytometry Analysis of MDA-MB-231 Cells Transduced with eGFP/mCherry Lentivirus. 135
Supplementary Figure 2. Flow Cytometry Analysis of MDA-MB-468 Cells Transduced with eGFP/mCherry Lentivirus. 137
Supplementary Figure 3. Gel electrophoresis analysis of CRISPRi screen PCR products. 138

List of abbreviations

$[Na^+]_e$ — Extracellular Sodium Concentration

$[Na^+]_i$ — Intracellular Sodium Concentration

2-HG — 2-hydroxyglutarate

AhR — Aryl hydrocarbon receptor

APC-A750 — Allophycocyanin-Alexa Fluor 750

ARNT — Aryl hydrocarbon receptor nuclear translocator

ASIC — Acid-Sensing Ion Channel

ASIC1 — Acid-Sensing Ion Channel 1

ATP — Adenosine triphosphate

BAGEL2 — Bayesian Analysis of Gene EssentiaLity, version 2

BC — Breast Cancer

BET — Bromodomain and extraterminal

BL1 — Basal-like 1

BL2 — Basal-like 2

bp — Base Pairs

BP — Bandpass (filter)

BRD — Bromodomain-containing protein

CAIX — Carbonic Anhydrase IX

Cas9 — CRISPR-associated protein 9

CBioPortal — cBioPortal for Cancer Genomics

CDK — Cyclin-Dependent Kinase

CMV — Cytomegalovirus (promoter)

CRISPRi — Clustered Regularly Interspaced Short Palindromic Repeats Interference

CsCl — Cesium chloride

CytoFLEX — Beckman Coulter CytoFLEX (flow cytometer)

DAPI — 4′,6-diamidino-2-phenylindole

dCas9 — Dead (catalytically inactive) Cas9

D-glucose — Dextrose (Glucose)

DMEM — Dulbecco’s Modified Eagle Medium

DMSO — Dimethyl sulfoxide

DNA — Deoxyribonucleic acid

DNMT — DNA methyltransferase

EDTA — Ethylenediaminetetraacetic acid

EGFP — Enhanced green fluorescent protein

EMT — Epithelial-mesenchymal transition

ENaC — Epithelial Sodium Channel

ER — Oestrogen Receptor / Estrogen Receptor

FACS — Fluorescence-Activated Cell Sorting

FBS — Foetal bovine serum

FGF — Fibroblast Growth Factor

FDR — False Discovery Rate

FIH — Factor Inhibiting HIF

FITC — Fluorescein Isothiocyanate

GABA — Gamma-Aminobutyric Acid

GDC — Genomic Data Commons

GLS — Glutaminase

GLUT — Glucose Transporter

GFP — Green fluorescent protein

gRNA — Guide RNA

HAF — Hypoxia-Associated Factor

HDACs — Histone Deacetylases

HEPES — 4-(2-hydroxyethyl)-1-piperazineethanesulfonic acid

HER2 — Human Epidermal Growth Factor Receptor 2

HIF — Hypoxia-Inducible Factor

HIF-1α — Hypoxia-Inducible Factor 1 Alpha

HIF-2α — Hypoxia-Inducible Factor 2 Alpha

HIF1A / HIF2A — Hypoxia-Inducible Factor 1-alpha / 2-alpha

HRE — Hypoxia-Responsive Element

HR+ — Hormone Receptor-Positive

HRm — High-resolution monochrome (camera)

IC — Class IC (Antiarrhythmic Drug Classification)

IDH — Isocitrate dehydrogenase

IFM motif — Isoleucine–Phenylalanine–Methionine motif

iPSC — Induced Pluripotent Stem Cell

i7/i5 — Illumina Index Adapter Sequences

KRAB — Krüppel-associated box

LME — Linear Mixed Effects model

$\log_2$FC — Log_2 Fold Change

MAGeCK — Model-based Analysis of Genome-wide CRISPR-Cas9 Knockout

MAGeCKFlute — MAGeCK Follow-Up Toolbox

MeCP2 — Methyl-binding protein 2

MLE — Maximum Likelihood Estimation

MOI — Multiplicity of Infection

MRI — Magnetic Resonance Imaging

mTOR — mammalian target of rapamycin

MDA-MB-231 — Human breast cancer cell line

Na^+ — Sodium ion / Sodium Ion

NaCT — Sodium-Coupled Citrate Transporter

NALCN — Na^+ Leak Channel Non-Selective

NBC — Na^+-Bicarbonate Cotransporter

NBCn1 — Na^+-Bicarbonate Cotransporter (SLC4A7)

NCX — Na^+-Ca^{2+} Exchanger

NHE1 — Sodium-Hydrogen Exchanger 1

NHE10 — Sodium/Hydrogen Exchanger 10

NF-core — Nextflow Core

NKCC — Na^+-K^+-Cl^- Cotransporter

NKA — Na^+/K^+-ATPase

NaPi-IIa / IIb / IIc — Sodium-dependent Phosphate Transporter Type IIa / IIb / IIc

$Na_v1.5$ — Voltage-gated sodium channel alpha subunit 1.5 (encoded by SCN5A)

NMDA — N-Methyl-D-Aspartate

NMDA-R — N-Methyl-D-Aspartate Receptor

PBS — Phosphate-buffered saline

PB450-A — Pacific Blue 450 Area

PCR — Polymerase Chain Reaction

PFA — Paraformaldehyde

PD1 — Programmed Cell Death Protein 1

PD-L1 — Programmed Death-Ligand 1

PDGF — Platelet-Derived Growth Factor

PDH — Pyruvate Dehydrogenase

PDK1 — Pyruvate Dehydrogenase Kinase 1

PFS — Progression-Free Survival

PHD — Prolyl Hydroxylase Domain Protein

PR — Progesterone Receptor / Progesterone receptor

Propafenone — A class 1C antiarrhythmic drug used to block sodium channels

PSS — Physiological Saline Solution

Rb — Retinoblastoma Protein

RRA — Robust Ranking Aggregation

ROS — Reactive Oxygen Species

RT — Room Temperature

RT-qPCR — Reverse Transcription Quantitative Polymerase Chain Reaction

SEM — Standard Error of the Mean

SGLT — Sodium-Glucose Linked Transporter

SNAT / SLC38A2 — Sodium-Coupled Neutral Amino Acid Transporter 2

SSC-A — Side Scatter Area

SLC4A4 — Solute Carrier Family 4 Member 4

SLC4A5 — Solute Carrier Family 4 Member 5

T0 — Time zero (baseline sample)

T2A — Thosea asigna virus 2A self-cleaving peptide

T25/T75 — Tissue culture flask (25/75 cm^2)

TCA — Tricarboxylic Acid

Tie2 — Tunica Intima Endothelial Kinase 2

Tp — Time to peak current

TTX — Tetrodotoxin

TU/mL — Transducing units per millilitre

τf — Fast time constant of inactivation

τs — Slow time constant of inactivation

VGSC — Voltage-Gated Sodium Channel

VHL — Von Hippel-Lindau

Acknowledgements

I would like to express my deepest gratitude to my primary supervisor, Prof. William Brackenbury, for his support and invaluable guidance throughout my postgraduate research journey. I am also grateful to my secondary supervisor, Dr. Andrew Holding, for his insightful advice and encouragement.

Special thanks to all members of the Brackenbury lab group Jodie Mason, Alina Capatina, Nat Sajjaboontawee, Lucy Gregg, Mahari Rodrigo, Serife Yerlikaya, Vinayak Thattaruparambil, Affaf Khelil, Dario Guglietta, Mary Catacutan, Rumesha Siriwardena, Alca Revalova, and Pete Boxall for their help and support both inside and outside the lab.

I would also like to acknowledge the Technology Facility staff at the University of York, including the Imaging and Cytometry teams (Karen Hogg, Karen Hodgkinson, Graeme Park, and Grant Calder) and the Genomics teams (Sally James and Lesley Gilbert), for their expertise and invaluable assistance.

Finally, I am deeply thankful to my family and friends for their encouragement and for helping me navigate the many ups and downs of this degree.

Declaration

I declare that this thesis is a presentation of original work and I am the sole author. This work has not previously been presented for a degree or other qualification at this University or elsewhere. All sources are acknowledged as references.

1. Introduction

1.1 Breast cancer

Breast cancer (BC) is the most frequently diagnosed cancer in women worldwide, affecting 1 in 7 women. Meanwhile, metastatic breast cancer has the highest cancer-related mortality in women (Breast Cancer Now, 2023; Bray et al., 2018). BC is a heterogeneous disease; the tumour microenvironment includes a range of cell types including epithelial, immune, stromal, and endothelial (Wagner et al., 2019).

BC is commonly stratified based on the expression of molecular markers; oestrogen receptor (ER), progesterone receptor (PR) and human epidermal growth factor receptor 2 (HER2). Clinically, these markers are used to guide therapy, with ER and/or PR positivity defining hormone receptor-positive (HR^+) disease, and HER2 amplification identifying HER2-enriched tumours. Triple-negative breast cancer (TNBC) is defined by the absence of ER, PR, and HER2 expression.

Beyond receptor status, intrinsic gene expression profiling using the PAM50 classifier identifies five molecular subtypes: luminal A, luminal B, HER2-enriched, basal-like, and normal-like. These molecular subtypes provide greater prognostic and therapeutic insight than receptor status alone, as they capture differences in tumour biology, proliferation, and treatment response (Perou et al., 2000; Parker et al., 2009). TNBCs predominantly fall within the basal-like group but remain molecularly heterogeneous (Jiang et al., 2019). In 2011, Lehmann's group further subdivided TNBC into six subtypes: two basal-like (BL1 and BL2), immunomodulatory, mesenchymal, mesenchymal-stem-like and luminal androgen receptor (Bonotto et al., 2014; Lehmann et al., 2011).

TNBC accounts for 10-15% of all breast cancer cases and is more frequently overrepresented in younger (under the age of 50), premenopausal women, particularly black women (Carey et al., 2006; Morris et al., 2007). Compared with hormone receptor-positive (HR+) breast cancer, TNBC generally has a worse prognosis, with higher rates of early recurrence and shorter overall survival, particularly in the metastatic setting. In this context, overall survival, defined as the time from the start of treatment for metastatic disease to death or last follow-up, has been reported as a median of 10.2 months (Bonotto et al., 2014).

Relative to other subtypes, TNBC is associated with increased aggressiveness, risk of local recurrence, and likelihood visceral metastasis. The risk of relapse is highest within the first 3 years after diagnosis, with a significant decline thereafter (Cai et al., 2023). Comparatively, TNBC recurs more rapidly than other subtypes, with a relapse time of 19-40 months compared to 35-67 months in non-TNBC patients (Steward et al., 2014). TNBC is highly invasive with a higher likelihood of distant metastasis (Dent et al., 2007).

The absence of defined molecular targets for TNBC makes treatment particularly difficult. Non-surgical therapies largely rely on broad-spectrum chemotherapy, like taxanes or anthracyclines (Brouckaert et al., 2012). While TNBC often shows initial sensitivity to standard chemotherapies, recurrence and mortality remains high. In addition, residual metastatic lesions following postoperative adjuvant chemoradiotherapy eventually lead to recurrence (Chaudhary et al., 2018). Targeted treatments, such as bromodomain and extra-terminal domain (BET) inhibitors, have demonstrated effectiveness but resistance quickly develops (Ge et al., 2020). Therefore, it is urgent to develop novel approaches that can target TNBC (Lobbezoo et al., 2013).

Aberrant proliferation is a hallmark of cancer (Fouad and Aanei, 2017). In healthy cells, the CDK4/6-Cyclin D1 complex controls progression of the G1 phase of the cell cycle through phosphorylating the Retinoblastoma (Rb) protein. When Rb is phosphorylated, it can no longer bind E2F, allows transcription of E2F target genes responsible for progression into S phase, such as CDK2 and Cyclin E (Rocca et al., 2017; O'Leary et al., 2016; Goel et al., 2018; Hu et al., 2021). Loss of control over the G1 checkpoint often occurs in cancer cells, including breast cancer (Pardee, 1989). Selective CDK4/6 inhibitors, such as palbociclib and abemaciclib, have demonstrated success particularly in HR+ breast cancers (Eggersmann et al., 2019; Turner et al., 2018). Palbociclib inhibits Rb phosphorylation, blocking the G1/S phase transition, halting the cell cycle (Finn et al., 2009). While CDK4/6 inhibitors are effective treatments in HR+ breast cancer, efficacy in TNBC is still being investigated. RB1 is mutated or deleted approximately 20% of TNBC cases (Ciriello et al., 2012). Studies have shown that while some Rb-positive TNBC cell lines are sensitive to CDK4/6 inhibitors, loss-of function Rb mutations lead to resistance (Finn et al., 2009; Gong et al., 2017; Condorelli et al., 2018).

Combining CDK4/6 inhibitors with agents targeting compensatory survival pathways such as PI3K/AKT/mTOR enhances efficacy (Yamamoto et al., 2019). Clinical data shows poor progression-free survival in TNBC patients treated with CDK4/6 inhibitors alone. Patients treated with palbociclib experienced rapid disease progression with a median progression-

free survival of only 1.5 months compared to 4.5 months in ER-positive patients (DeMichele et al., 2015). However, another study has reported progression-free survival of 6 months in 30% of patients and no unexpected toxicity (Gucalp et al., 2020).

Tumours with high levels of tumour-infiltrating lymphocytes (TILs), defined as occupying more than 50% of the stromal area in histological sections, are generally associated with better prognoses (Stanton et al., 2016). In TNBC, elevated TILs correlate with the immune-checkpoint receptor, PD1, and its ligand, PD-L1 (Pardoll., 2012; West et al., 2011). When PD-L1 on tumour cells binds to PD1 receptors on activated T-cells, it inhibits their cytotoxic activities on the tumour. PD-L1 is expressed in 20% of TNBC cases (Mittendorf et al., 2014). PD1 inhibitors, such as pembrolizumab, effectively treat lung and bladder cancers (Garon et al., 2015; Bellmunt et al., 2017). Pembrolizumab has demonstrated antitumor activity in TNBC (Nanda et al., 2016). Pembrolizumab, particularly when combined with chemotherapy, reduces disease progression and mortality (Cortes et al., 2020).

1.2 Hypoxia in TNBC

Hypoxia is common in solid tumours, including TNBC, and is strongly linked to poorer outcomes (Li et al., 2022; Sun et al., 2021; Liu et al., 2022). In tumours, oxygen levels drop to 1–2%, compared to 4–9% in normal tissues. Rapid cell proliferation in tumours increases distances between blood vessels and cells, leading to reduced oxygen perfusion, and impairing oxygen supply to cells (Muz et al., 2015; Emami Nejad et al., 2021; Shi et al., 2021; Zhang et al., 2021).

Acute hypoxia involves transient disruptions in blood flow, typically lasting less than 72 hours. It is reversible and prompts adaptive responses such as metabolic changes, autophagy activation, and resistance to apoptosis. Chronic hypoxia is persistent low oxygen which causes genetic instability through increased DNA replication errors and breaks (Muz et al., 2015; Shi et al., 2021). Hypoxia reduces protein synthesis and promotes cell death through apoptosis or necrosis in normal tissues (Kozal and Krześlak, 2022). However, cancer cells have increased proliferation and invasiveness under hypoxia. This selective pressure leads to a more aggressive tumour phenotype that can survive in low oxygen (Kozal and Krześlak, 2022).

Hypoxia-inducible factors (HIFs) regulate the hypoxic response. HIFs are transcription factors composed of an oxygen-sensitive α-subunit (HIF-1α, -2α, or -3α) and a stable β-subunit (HIF-1β, -2β, -3β), also known as ARNT (Cavadas et al., 2013; Kozal and Krześlak, 2022). In normoxia, the HIF-α is hydroxylated on specific proline residues by oxygen-dependent prolyl hydroxylases (PHDs), which allows recognition by the Von Hippel-Lindau (VHL) E3 ubiquitin ligase complex and subsequent proteasomal degradation (Figure 1.1) (Cavadas et al., 2013). Regulation also occurs through asparaginyl hydroxylase factor inhibiting HIF (FIH), which stops HIF recruiting transcriptional coactivators p300/CBP (Cavadas et al., 2013). Under hypoxia, HIF-α is stabilised, allowing it to accumulate, and translocate to the nucleus where it dimerises with HIF-β. The active HIF complex activates gene expression through binding to hypoxia-responsive elements (HRE) with P300/CBP (Figure 1.1) (McKeown, 2014).

In TNBC, HIF-1 activity is increased and is associated with worse prognosis (Wang et al., 2014; Mori et al., 2020). Knocking down HIF-1α impairs TNBC cell viability under hypoxia, whereas silencing HIF-2α increases survival, likely due to its pro-apoptotic role (Mori et al., 2020). HIF-3α acts as a negative regulator of HIF-driven transcription (Yang et al., 2015).

HIFs regulate the expression of over 150 genes including genes involved in glycolysis, angiogenesis, invasion and immune evasion (Semenza, 2007; Pugh and Ratcliffe, 2003; Muñoz-Nájar et al., 2006; Ward et al., 2015). HIF-1 induces angiogenesis through upregulation of vascular endothelial growth factor (VEGF), fibroblast growth factor (FGF), platelet-derived growth factor (PDGF), angiopoietins, and tunica intima endothelial kinase 2 (Tie2) (Liu et al., 1995; Srivastava et al., 2023). Angiogenesis can facilitate tumour progression and, in some contexts, may increase tumour invasiveness. Disorganised and leaky tumour vasculature may also impair drug delivery and immune responses (de Heer et al., 2020; Saman et al., 2020).

HIF activation shifts tumour cell metabolism from oxidative phosphorylation to glycolysis to meet cellular demands, the Warburg effect (de Heer et al., 2020; Warburg, 1956). The shift to glycolysis occurs through increasing the expression of glucose transporters (GLUT-1 and GLUT-3) and glycolytic enzymes like hexokinase 1 and 2 and PDK1. PDK1 inhibits PDH which converts pyruvate to acetyl-CoA (Ikeda et al., 2020; Mamun et al., 2020; Srivastava et al., 2023). As a result, pyruvate is used in lactate production instead of mitochondrial respiration (Figure 1.1). Accumulated lactate leads to extracellular acidification promoting tumour cell proliferation, survival and invasiveness (Kim et al., 2006; Marchiq and Pouysségur., 2016; Chen et al., 2021). Elevated glycolytic activity also enhances reactive

oxygen species (ROS) scavenging, increases resistance to radiotherapy, and promotes migration in breast cancer cells (Zois and Harris, 2016). HIF-1 also upregulates immunosuppressive molecules such as PD-L1, VEGF, prostaglandin E2 (PGE2). PD-L1 inhibits T cell responses, facilitating immune evasion (Kozal and Krześlak., 2022; You et al., 2021; Wu et al., 2022).

In addition to transcriptional and metabolic changes, hypoxia also drives epigenetic regulation that tightly interacts with tumour metabolism. For example, in TNBC, hypoxia-driven accumulation of lactate promotes histone H4K12 lactylation, enhancing expression of genes that drive glycolysis, angiogenesis, and invasion (Li et al., 2024; Cui et al., 2024). Lactate accumulation from increased glycolysis inhibits histone deacetylases (HDACs), thereby enhancing transcription of oncogenes such as *c-Myc* and *SRSF10* (Latham et al., 2012; San-Millán et al., 2019; Pandkar et al., 2023). Acetyl-CoA, a central metabolic intermediate, fuels histone acetylation and lipogenesis, with the latter being a recognised driver of malignant transformation (Menendez and Lupu, 2007; Messier et al., 2016). Mutations in tricarboxylic acid (TCA) cycle enzymes further connect metabolism and epigenetics. Isocitrate dehydrogenase (IDH) mutations are associated with depletion of α-ketoglutarate and accumulation of the oncometabolite 2-hydroxyglutarate (2-HG), which inhibits histone demethylation and promotes HIF-1α signalling (Lu et al., 2012; Liu et al., 2023; Zhao et al., 2009; Zhang et al., 2013). In addition, metabolic receptors not directly involved in energy metabolism, such as the aryl hydrocarbon receptor (AhR), also promote epigenetic regulation in breast cancer. AhR has been linked to hypermethylation of CpG islands in oncogenes like *BRCA1*, increased trimethylation and deacetylation of H3K9, elevated DNA methyltransferase (DNMT1/3a/3b) expression, and higher levels of methyl-binding protein 2 (MeCP2) (Hockings et al., 2006; Papoutsis et al., 2012; Thakur et al., 2022).

Together, these metabolic–epigenetic interactions reinforce hypoxia-driven TNBC progression by supporting proliferation, angiogenesis, metastasis, and the acquisition of stem-like properties. Figure 1.1 summarises these mechanisms, highlighting how hypoxia stabilises HIF-1α and activates gene expression programs that promote glycolytic reprogramming, angiogenesis, and apoptotic evasion in TNBC (Srivastava et al., 2023).

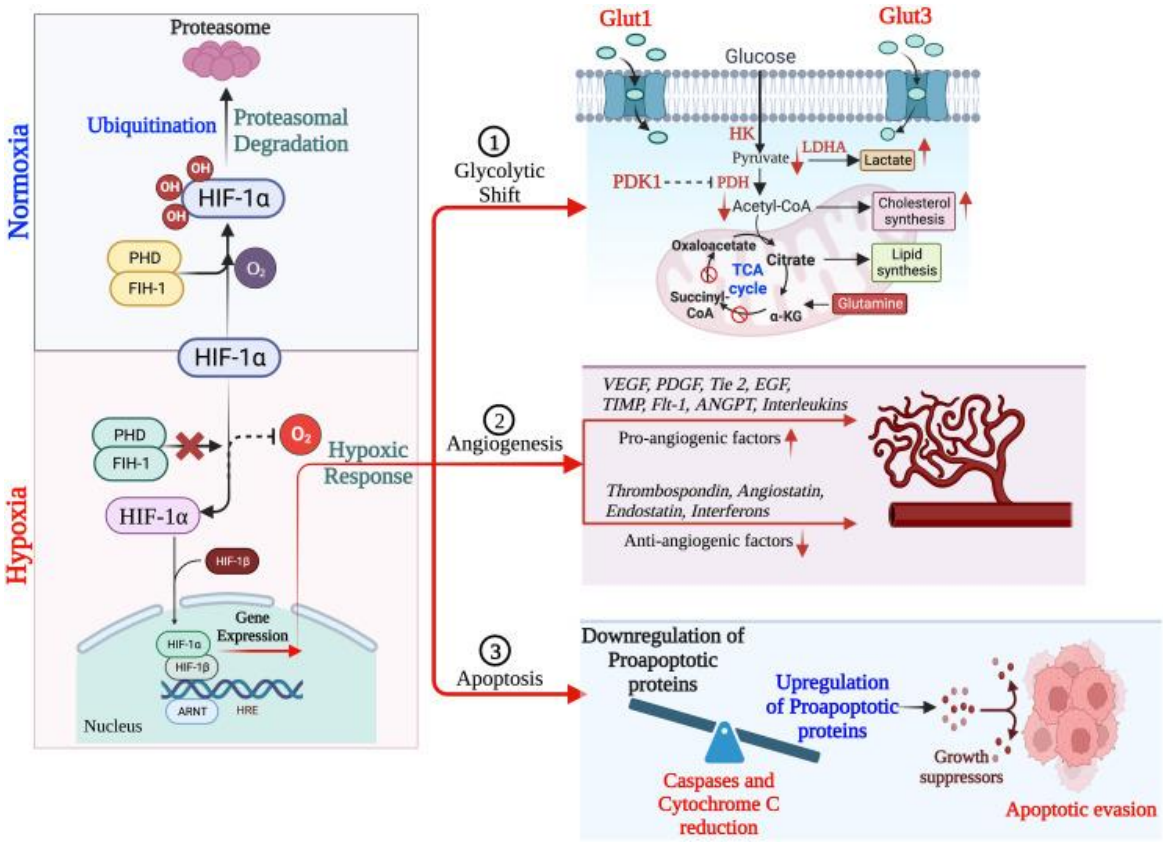


Figure 1.1. Regulation and downstream effects of HIF-1α signalling in TNBC.

Under normoxia, HIF-1α is hydroxylated by PHDs and targeted for ubiquitin-mediated proteasomal degradation by the VHL E3 ligase complex. Under hypoxia, this degradation pathway is inhibited, leading to HIF-1α stabilisation, nuclear translocation, and dimerisation with HIF-1β, which drives the transcription of genes promoting glycolysis, angiogenesis, and evasion of apoptosis. Reproduced from Srivastava et al., 2023.

1.3 Na+ in breast cancer

1.3.1 Na+ homeostasis

Breast tumours, particularly TNBC, show changes in ion homeostasis, including elevated levels of Na^+, protons (H^+), potassium (K^+), and dysregulated calcium (Ca^{2+}) signalling (Ouwerkerk et al., 2003; Webb et al., 2011; Pardo and Stühmer, 2014; Monteith et al., 2017). Na^+ is critical in maintaining cell homeostasis (Strazzullo and Leclercq, 2014; Laubitz et al., 2017). Na^+/K^+-ATPase (NKA) maintains the Na^+ gradient with a higher extracellular Na^+ concentration ($[Na^+]_e$) (~145 mM) and a lower intracellular Na^+ $[Na^+]_i$ (~12 mM) (Leslie et al., 2019; Bernal et al., 2023). NKA inhibition with ouabain leads to an increase in $[Na^+]_i$, highlighting the role of the pump in Na^+ transport (Leslie et al., 2024). NKA exports Na^+ and imports K^+ using ATP as an energy source (Clausen and Poulsen, 2013). Inhibition of mitochondrial respiration using an ATP synthase inhibitor did not significantly alter $[Na^+]_i$, however, glycolysis inhibition increased $[Na^+]_i$ (Leslie et al., 2024). These findings indicate that NKA relies on glycolytic ATP in breast cancer cells, linking Na^+ regulation to tumour metabolism (Epstein et al., 2014). Disruption of Na^+ homeostasis is associated with acute inflammation, ischaemia, and cancer (Leslie et al., 2019).

Using 23Na MRI, researchers have observed that Na^+ levels are elevated in breast, brain, uterine, and prostate cancers (James et al., 2022; Jacobs et al., 2009; Barrett et al., 2018; Ouwerkerk et al., 2003, 2007; Marino et al., 2018). The $[Na^+]_i$ is elevated in cancer cells while $[Na^+]_e$ remains the same (Cameron et al., 1980; James et al., 2022). Increased expression of Na^+ channels is believed to cause elevated $[Na^+]_i$ (Roger et al., 2015; Leslie et al., 2022).

1.3.2 Na^+ Channel expression in breast cancer

Various Na^+ channels are upregulated in TNBC (Figure 1.2) and promote Na^+ influx into cancer cells (Leslie et al., 2022). The physiological reason for this upregulation is unclear. The elevated $[Na^+]_i$ increases proliferation, invasion, and inflammation which promotes tumour progression (Leslie et al., 2019).

Voltage-gated sodium channels (VGSCs) are upregulated in multiple solid tumours, including breast, prostate, lung, and colon cancer, promoting invasion (Leslie and Brackenbury, 2023; Lopez-Charcas et al., 2021; Djamgoz et al., 2019).

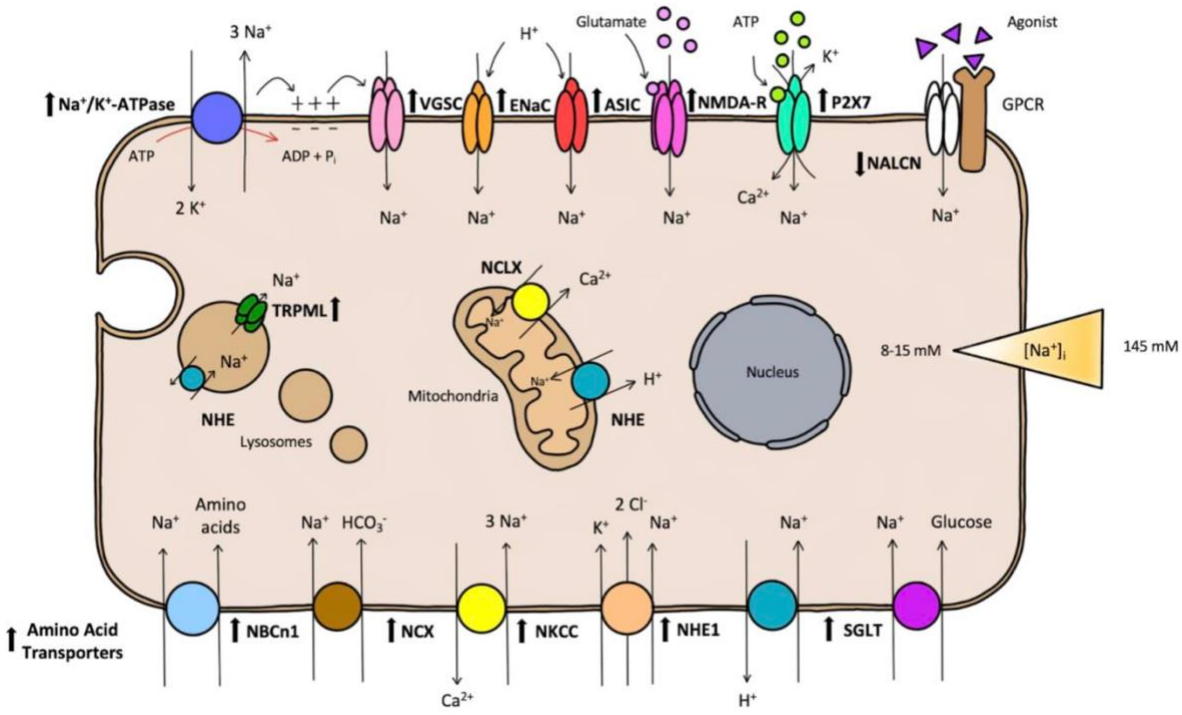


Figure 1.2. Na^+ channels and transporters.

Various Na^+ channels and transporters, many of which can demonstrate altered expression in cancer, the nature of their expression is represented by the direction of the arrow, channels without arrows have unaltered expression. Channels that allow for influx of Na^+ are VGSCs, ENaC, acid-sensing ion channel (ASIC), N-methyl-D-aspartate receptor (NMDA-R), Na^+ leak channel non-selective (NALCN), Na^+-glucose co-transporter (SGLT), NHE1, Na-K-Cl cotransporter (NKCC), NBCn1, and the amino acid transporters. Na^+/K^+ ATPase is involved in transport of Na^+ out of the cell. The Na^+- Ca^{2+} exchanger (NCX) can work towards Na^+ influx or efflux based upon the membrane potential and the concentrations of Ca^{2+} and Na^+ ions.

Reproduced with permission from: Plunkett-Jones, C. (2023). *Characterising the effect of sodium channel inhibitors on viability and intracellular sodium content in triple-negative breast cancer cells* (MSc by Research thesis, University of York).

1.3.3 VGSC structure and subtypes

VGSCs generate and propagate action potentials in electrically excitable cells such as nerve and muscle cells (Hille, 1978). VGSCs consists of a pore-forming α subunit associated with one or more auxiliary β subunits which modulates channel gating and kinetics (Catterall, 2000; Catterall, 2014; O'Malley and Isom, 2015). There are nine α subunits ($Na_v1.1$-$Na_v1.9$) and four β subunits (β1-4) (Brackenbury and Isom, 2011; Catterall, 2000; Goldin et al., 2000). The α-subunit consists of four homologous domains (D1-4), each containing six transmembrane segments (Figure 1.3A). The S1-4 segments enable voltage sensing while the S5-6 segments and the P-loop between them comprise the pore domain. The intracellular ends of the S6 segments serve as the activation gate, which rapidly opens the pore, and the intracellular loop connecting D1 and D4 forms the fast inactivation gate, which closes the pore. Flow of Na^+ through the pore is mediated by the ion selectivity filter, the P-loop, which ensures Na^+ selectivity over other ions (Catterall, 2000; Goldin, 2003)

The predominant α subunits in BC are $Na_v1.5$ and $Na_v1.7$ (Fraser et al., 2005). The most studied, $Na_v1.5$, expressed in the MDA-MB-231 cell line, increases cell invasiveness, proliferation and migratory ability (Brackenbury et al., 2007; Brisson et al., 2011; Fraser et al., 2005). Upregulation of $Na_v1.5$ at the mRNA level in breast cancer tissue is associated with metastasis (Yang et al., 2012). Silencing $Na_v1.5$ in BC cells using shRNA suppresses tumour growth and metastasis in a mouse orthotopic xenograft BC model (Nelson et al., 2015). $Na_v1.5$ is also upregulated in breast cancers at the protein level (Nelson et al., 2015). Survival and migration of TNBC cell lines, as well as their $Na_v1.5$ expression has been linked with HIF-1α expression, with both HIF-1α and $Na_v1.5$ being upregulated in TNBC cell lines, compared to other BC subtypes (Dewadas et al., 2019). $Na_v1.5$, encoded by *SCN5A*, is upregulated in breast cancer and promotes metastasis (Yang et al., 2012)

Various Na^+ channels are upregulated in cancers, including breast, brain, uterine, and prostate tumours (Leslie et al., 2019; James et al., 2022; Jacobs et al., 2009; Barrett et al., 2018) (Figure 1.2).

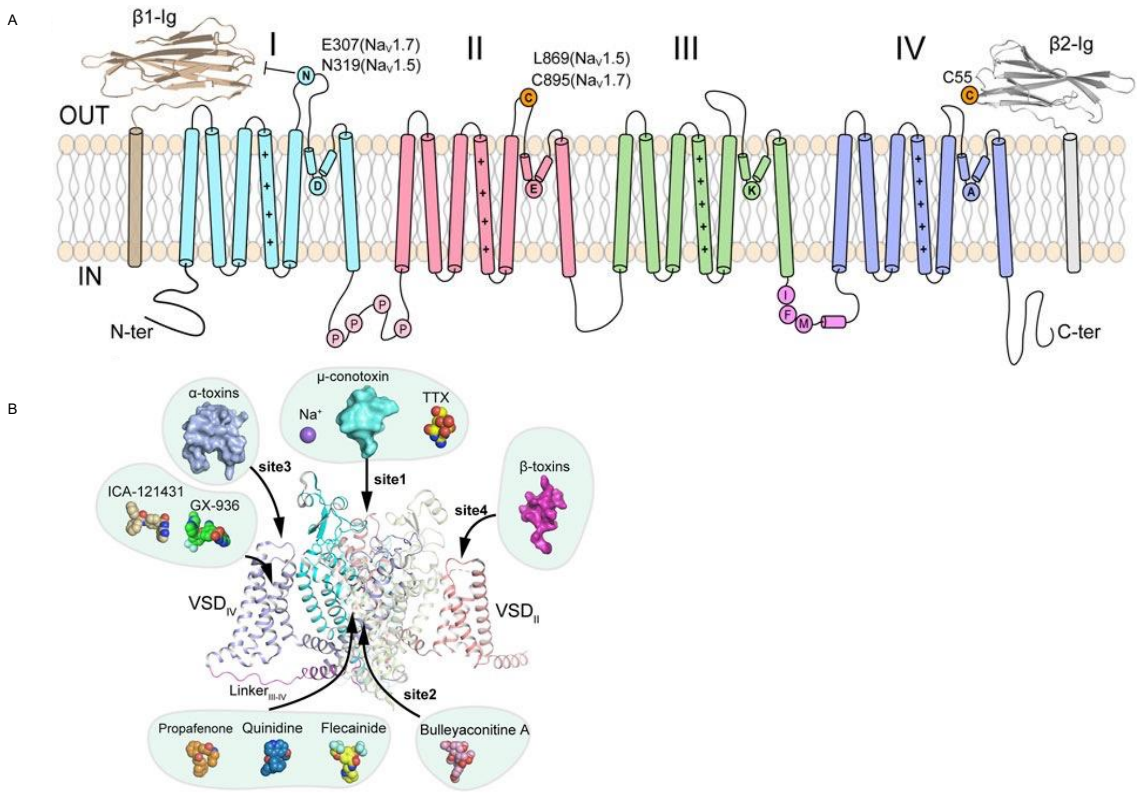


Figure 1.3. Topology and architecture of mammalian Na_V channels.

(A) Topology of mammalian Na_V channels. D_I, D_{II}, D_{III}, IFM-motif and D_{IV} of α-subunit, β1 and β2 subunit are coloured in cyan, red, green, purple, blue, brown and grey, respectively. A unique N-glycosylation site in $Na_V1.5$ and the cysteine residue for linking β2 are highlighted. P represents phosphorylation sites. (B) Multiple ligand binding sites in mammalian Na_V channel α-subunit. Sodium ion and small-molecule modulators shown in spheres; polypeptide toxins shown in surface. Reproduced from Jiang et al., 2022.

1.3.4 Functional consequences of Na^+ channel upregulation

Upregulation of Na^+ channels, such as $Na_v1.5$, and increased Na^+ influx has several downstream effects that contribute to cancer progression, particularly migration, invasion, metabolism and inflammation.

One of the most studied consequences of Na^+ influx is increased migration. Migration is facilitated through several mechanisms involving Na^+ channels and transporters. Various Na^+-permeable channels contribute to Na^+ influx, including epithelial Na^+ channels (ENaC), Na^+-glucose transporters (SGLTs), the Na^+-hydrogen exchanger (NHE1), and VGSCs (Supplementary Table 1). VGSCs are upregulated in breast cancer including $Na_v1.5$, encoded by *SCN5A*, which is upregulated in breast cancer and promotes metastasis (Yang et al., 2012). $Na_v1.5$ facilitates Na^+ influx, leading to membrane depolarisation which triggers Rac1 signalling, lamellipodia formation and cell migration (Brisson et al., 2013; Yang et al., 2020). $Na_v1.5$ is also co-localised with NHE1 which increases H^+ efflux, causing acidification of the extracellular matrix (ECM). Acidification activates cathepsins and promotes ECM degradation, further facilitating cell invasion (Besson et al., 2015; Yadati et al., 2020). Increased invasiveness of cancer cells leads to metastasis (Di Martino et al., 2021).

$Na_v1.5$ activity also influences tumour metabolism. Na^+ influx through $Na_v1.5$ increases demand on the NKA, which maintains the ionic gradient and depends on glycolytic ATP (Nyblom et al., 2013; Leslie et al., 2024). Elevated persistent Na^+ currents under low pH conditions in breast cancer cells reflect increased $Na_v1.5$-mediated glycolysis, likely driven by increased ATP demand through Na^+/K+ ATPase activity (Leslie et al., 2023; Nyblom et al., 2013; Epstein et al., 2014). The metabolic shift increases proton production, contributing to extracellular acidification. Acidification promotes persistent Na^+ influx through $Na_v1.5$, establishing a positive feedback mechanism. This feedback loop supports invasiveness in breast cancer cells (Leslie et al., 2023; 2024). This metabolic shift to glycolysis is consistent with the pH levels observed in solid tumours. Highly proliferative solid tumours maintain a more alkaline intracellular pH (Pedersen and Stock, 2013; Leslie et al., 2019; Lu et al., 2020). These cancers have increased expression of acid-extruding Na^+ transporters such as NHE1 and NBCn1 (Pedersen and Stock, 2013; Lee et al., 2015; Chen et al., 2019). NHE1 is upregulated in many tumours to maintain more alkaline intracellular pH and promote cell growth. However, in certain contexts like gastric cancer, NHE1 downregulation is associated with a poorer prognosis, (Chen et al., 2019).

In addition to regulating migration and metabolism, Na^+ influx can influence inflammatory signalling in tumours. Elevated Na^+ in the tumour microenvironment has been associated with chronic inflammation (Amara et al., 2016). One mechanism for this association involves the ENaC γ-subunit (γENaC). γENaC is linked to release of reactive oxygen and nitrogen species (ROS and RNS) which stimulate release of pro-inflammatory cytokines like IL-6 and TNFα (Xu et al., 2016; Leslie et al., 2019; Sudarikova et al., 2022; Chen et al., 2023). Furthermore, knock down of γENaC reduces RNS and ROS (Amara et al., 2016). Other Na^+ channels may be involved in inflammation within tumours, including breast cancer, where inflammation increases metastasis and tumour progression (Müller et al., 2001; Hibino et al., 2021)

Together, these findings illustrate how Na^+ channel and transporter upregulation influence multiple hallmarks of cancer including altered metabolism, inflammation, migration and invasion.

1.4 Effect of Hypoxia on Na^+ transport in breast cancer

While a general mechanism for hypoxic regulation of VGSCs in cancer has not been established, evidence from human iPSC-derived cardiomyocytes demonstrates that hypoxia can increase $Na_v1.5$-mediated Na^+ currents, specifically by increasing the late Na^+ current, highlighting the potential for hypoxia to regulate VGSC function (Plant et al., 2020). Hypoxia increasing $Na_v1.5$ expression in cardiomyocytes raises the possibility of similar effects in tumour cells. In addition to voltage-gated sodium channels (VGSCs), other Na^+ transporters are regulated by hypoxia and may contribute to cancer progression. For example, hypoxia increases the expression and activity of NHE1 in breast cancer cells, promoting migration and epithelial-mesenchymal transition (EMT) (Takatani-Nakase et al., 2022). Similarly, Na^+-dependent bicarbonate transporters such as SLC4A4 and SLC4A5 are upregulated in hypoxic TNBC cell lines, including MDA-MB-231, and knockdown of SLC4A4 and SLC4A5 reduces invasion and metastasis (Carroll et al., 2022).

Hypoxia leads to acidification of the tumour microenvironment, which activates acid-sensing ion channels such as ASIC1. ASIC1 activation is driven by HIF-1 upregulating carbonic anhydrase IX (CAIX), an enzyme that facilitates acid extrusion via anion exchange. The activation of ASIC1 is associated with the regulation of autophagy in cancer cells (Yingjun and Xun, 2013; Chen et al., 2021). Furthermore, hypoxia upregulates NHE1 at the protein level in breast cancer (Takatani-Nakase et al., 2022). During lactic acidosis, NHE1 is localised to the basal membrane to regulate intracellular pH, supporting cell survival (Jun et al., 2017; Takatani-Nakase et al., 2022). The presence of a HRE in its promoter supports NHE1 as a HIF-1 target (Lucien et al., 2011). Na^+-bicarbonate cotransporters (NBCs), including SLC4A4 and SLC4A5, are upregulated in hypoxic breast cancer cells. Their knockdown reduces proliferation and increases apoptosis (Carroll et al., 2022). SLC38A2 (SNAT2), a Na^+-coupled amino acid transporter, is upregulated by HIF-1α in hypoxic breast cancer cells and is linked to therapy resistance. Hypoxia also alters glycosylation, promoting localisation of SNAT2 to the cell membrane (Morotti et al., 2019). SNAT2 also contains a binding site for HIF-2α, suggesting it contributes to both early and late hypoxic responses. However, not all transporter activity is increased under hypoxia. In ischemic heart disease, NKA activity is reduced which conserves ATP. The downregulation of activity occurs through ROS-mediated endocytosis of the pump's α-subunit (Comellas et al., 2006; Baloglu, 2023).

These findings suggest that hypoxia effects various Na^+ transporters, influencing tumour pH regulation, survival, invasion, and therapy resistance. While elevated $[Na^+]_i$ has been shown

in tumours, the mechanisms driving this accumulation are only partially understood (Fraser et al., 2014; Leslie et al.,2022). Expression of Na^+ channels and transporters such as ASIC1, NHE1, NBCs, SLC38A2, and NKA is associated with hypoxia (Comellas et al., 2006; Leslie et al., 2019; Morotti et al., 2019; Chen et al., 2021; Carroll et al., 2022; Takatani-Nakase et al., 2022). Na^+ channels may be viable therapeutic targets due to their involvement in cancer progression (Brisson et al., 2013; Besson et al., 2015; Amara et al., 2016). However, how these Na^+ transporters lead to cancer progression in hypoxic TNBC remains underexplored**,** particularly how they influence metastasis.

Hypoxia regulates VGSCs, including $Na_v1.5$, leading to an increase in persistent inward Na^+ current (Plant et al., 2020; Ju et al., 1996; Hammarström and Gage, 2002). Hypoxia-driven Na^+ influx is particularly relevant in solid tumours, such as breast cancer, in which hypoxia is common and associated with worse outcomes. In cardiac tissue, hypoxic regulation of VGSCs, particularly $Na_v1.5$, has been studied. Under hypoxia, $Na_v1.5$ channel expression and activity can be modulated by HIF-1α, which influences not only the number of channels expressed but also their biophysical properties. These mechanisms may be conserved in cancer cells but are not yet fully characterised. Despite the growing interest in $Na_v1.5$, the many other Na^+ channels may also be regulated by hypoxia and contribute to invasion, metastasis and tumour progression in hypoxic TNBC, although their specific roles remain unclear. Understanding these potential contributions could reveal new targets for hypoxic TNBC treatments.

In summary, hypoxia modulates Na^+ channel and transporter activity primarily through the HIF-1α pathway, which alters both expression and functional properties of these proteins. In TNBC, HIF-1α upregulation under low oxygen can increase $Na_v1.5$-mediated persistent Na^+ currents, promoting membrane depolarisation and activating Rac1 signalling, which drives lamellipodia formation and enhances cell migration (Brisson et al., 2013; Plant et al., 2020). Similarly, HIF-1α induces NHE1 and NBC expression, supporting intracellular alkalinisation and extracellular acidification, which promotes ECM degradation and invasion via activation of proteases like cathepsins (Takatani-Nakase et al., 2022; Carroll et al., 2022). Acid-sensing channels such as ASIC1 are also activated by hypoxia-induced acidification, triggering autophagy and cell survival pathways (Yingjun and Xun, 2013; Chen et al., 2021).

These hypoxia-driven Na+ transport adaptations occur downstream of HIF-1α and complement a broader network of metabolic and signalling adaptations in TNBC. Figure 1.1 summarises HIF-1α stabilisation under hypoxia and its consequences on metabolic reprogramming, angiogenesis, and apoptotic evasion in TNBC (Srivastava et al., 2023).

Collectively, these processes support TNBC progression by enhancing proliferation, migration, invasion, and therapy resistance.

1.5 Therapeutic targeting of VGSCs in cancer

Given the upregulation of Na^+ channels such as $Na_v1.5$ in hypoxic tumours, targeting these channels could be a promising therapeutic strategy and may be useful for reducing metastasis. $Na_v1.5$ is pharmacologically Tetrodotoxin (TTX)-resistant, whereas other VGSCs such as $Na_v1.7$ are TTX-sensitive (Fraser et al., 2005). Down-regulation of $Na_v1.5$ expression significantly reduces tumour growth, invasion and metastasis in BC models (Nelson et al., 2015). Antiepileptic and antiarrhythmic drugs, which inhibit VGSCs, could also potentially be repurposed in cancer therapy. Pharmacological inhibition of $Na_v1.5$ with clinically available VGSC blockers, such as phenytoin and ranolazine, has been shown to reduce invasiveness of cancer cells *in vitro* and metastasis *in vivo* (Driffort et al., 2014; Nelson et al., 2015; Nelson et al., 2015). Ranolazine, a Na^+ current inhibitor used to treat angina, reduces the activity of the neonatal $Na_v1.5$ isoform, which is the only functional isoform expressed in human breast cancer cells (Driffort et al., 2014; Fraser et al., 2005). Ranolazine inhibits $Na_v1.5$-related invasion in breast cancer cells and significantly reduces lung colonisation *in vivo* in mouse models (Driffort et al., 2014). These approved medications could potentially target VGSCs in the context of cancer to reduce invasiveness and metastasis.

While these findings are promising, more work is needed to evaluate the clinical efficacy and long-term safety of VGSC inhibitors in cancer patients. A significant challenge is that VGSCs are also critical in excitable tissues, raising concerns about potential off-target effects, especially cardiac and neurological side effects.

Treatment with VGSC inhibiting antiarrhythmics is associated with reduced cancer-specific mortality in breast cancer patients. These antiarrhythmics have been shown to correlate with improved patient survival (Fairhurst et al., 2023). While the inhibitory effect of the antiarrhythmic propafenone on VGSCs has been well-established in cardiomyocytes, other VGSC-inhibiting drugs, such as the antiepileptic phenytoin, have been shown to significantly suppress invasion, migration, and metastasis of cancer cells (Fraser et al., 2003; Nelson et

al., 2015; Yang et al., 2012). These findings suggest that VGSC-inhibiting drugs could potentially be repurposed to reduce breast cancer metastasis.

1.6 Propafenone

While phenytoin and ranolazine have been more extensively studied, propafenone**,** another antiarrhythmic drug, has not yet been evaluated in the context of cancer. Propafenone is a class IC Na^+ channel-blocking drug in the antiarrhythmic family which also includes flecainide (Funck-Brentano et al., 1990; Bryson et al., 1993; Kishore & Camm, 1995; UK Propafenone PSVT Study Group, 1995) (Figure 1.4). Propafenone blocks VGSCs, including $Na_v1.5$, by binding to a high-affinity site within the inner pore of the α-subunit, near the S6 segments of domains III and IV, which line the inner cavity of the channel (Catterall et al., 2020; Hille, 1977; 1978; Hondeghem and Katzung, 1984; Jiang et al., 2021) (Figure 1.3B). Propafenone's binding site overlaps with the local anaesthetic receptor site, shared by other blockers like lidocaine and flecainide (Ragsdale et al., 1994) (Figure 1.3B). Propafenone binds in a state-dependent manner, favouring the open state of the channel, which is common in rapidly depolarising or proliferating cells such as cancer cells (Edrich et al., 2005; O'Leary and Chahine, 2018).

Administered orally, propafenone has been widely used in establishing and maintaining sinus rhythm in patients with atrial fibrillation (Gentili et al., 1992; Kirchhof et al., 2016; Porterfield and Porterfield, 1989). While also blocking L-type Ca^{2+} currents, K^+ currents and beta-adrenergic receptors, propafenone treats arrhythmia through its main effect of blocking fast Na^+ currents in cardiac cells in a use-dependent manner (Fei et al., 1993; McLeod et al., 1984; Slawsky and Castle, 1994; Williams, 1984).

In summary, there is an emerging role of VGSCs, particularly $Na_v1.5$, in regulating cancer cell invasion and metastasis. VGSCs are upregulated in hypoxic tumours, including TNBC. The upregulation of $Na_v1.5$ and various other Na^+ channels under hypoxia has been linked to increased invasiveness and metastatic potential. Pharmacological inhibition of $Na_v1.5$ using clinically approved drugs such as phenytoin and ranolazine has demonstrated promising anti-invasive effects, supporting the idea that VGSCs may be viable therapeutic targets in cancer. However, other VGSC inhibitors, such as the antiarrhythmic propafenone, remain largely unstudied in the cancer context. Moreover, while $Na_v1.5$ has been a focus, multiple Na^+ channels may also be upregulated in hypoxia and contribute to tumour progression.

Therefore, this study aimed to investigate whether additional Na^+ channels are involved in TNBC proliferation under hypoxic conditions, and to evaluate the potential of propafenone to inhibit $Na_v1.5$ activity in this context.

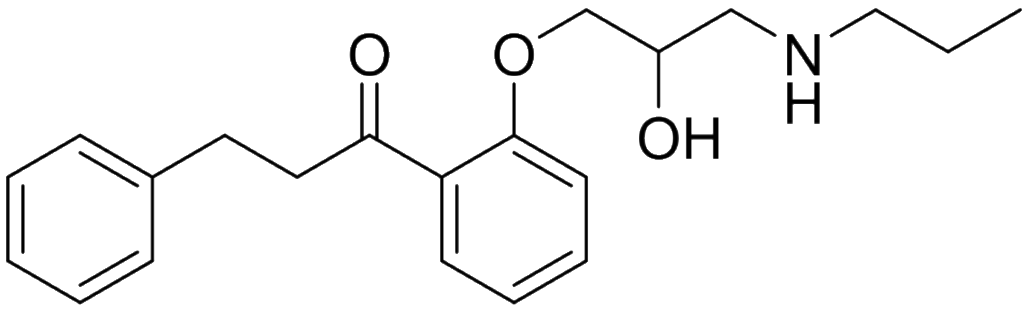


Figure 1.4. Chemical structure of propafenone.

1-[2-[2-hydroxy-3-(propylamino)propoxy]phenyl]-3-phenyl-1-propanone. Structure was drawn using ChemDraw software.

1.7 Hypothesis and aims

We hypothesise that there are multiple Na^+ channels that have a role in increasing cancer cell proliferation during hypoxia. This study aimed to investigate the importance of Na^+ transporters in hypoxic TNBC cell proliferation through a targeted CRISPR interference (CRISPRi) screen to identify potential therapeutic targets. We also aimed to evaluate the therapeutic potential of targeting the well-established channel $Na_v1.5$ in TNBC cells using propafenone, a clinically approved antiarrhythmic drug that has not yet been studied in the cancer context. This aimed to determine whether propafenone could be repurposed to therapeutically inhibit $Na_v1.5$ in TNBC, reducing metastasis and disease progression.

The first objective was to generate TNBC cell lines, MDA-MB-231 and MDA-MB-468, which stably expressed dCas9/KRAB. dCas9 is a catalytically dead version of the CRISPR-associated protein 9 (Cas9).

The second objective was to compile an exhaustive list of genes involved in Na^+ transport based on literature and database searches, and subsequently to design and generate a guide RNA (gRNA) library targeting these genes (Table S1).

The third objective was to perform a functional CRISPRi screen in hypoxia against normoxia to identify Na^+ channels and transporters genes that are important for TNBC cell proliferation under hypoxia.

The fourth objective was to evaluate the inhibitory effects of propafenone on VGSC current in TNBC. We used whole-cell patch clamping to investigate the electrophysiological effects of propafenone, a VGSC inhibitor, on VGSCs endogenously expressed in the MDA-MB-231 metastatic TNBC cell line. MDA-MB-231 endogenously express $Na_v1.5$.

2. Materials and methods

2.1 Cell culture and hypoxic incubations

MDA-MB-231 and MDA-MB-468 cell lines were used which are classified as TNBC due to their lack of ER, PR and HER2 expression (Chavez et al., 2011). Cells were grown in Dulbecco's modified Eagle medium (DMEM, high glucose, with L-glutamine (4 mM); Sigma-Aldrich, Cat. No. D6429) supplemented with 5% foetal bovine serum (FBS; Sigma-Aldrich, Cat. No. F7524) (Nelson et al., 2015). Cells were confirmed as mycoplasma-free using the DAPI method (Uphoff et al., 1992) with ProLong™ Gold Antifade Mountant with DAPI (Fisher Scientific, Cat. No. 11569306).

Cells were kept in a humidified incubator at 37°C with 5% CO_2 for normoxia conditions and in a hypoxic humidified workstation at 37°C with 1% O_2 and 5% CO_2 with N_2 balance for hypoxia conditions.

2.2 Freezing and thawing Cells

Freezing medium consisted of DMEM (Sigma, with 4 mM L-glutamine) supplemented with FBS (Sigma; 5:1) and tissue culture–grade dimethyl sulfoxide (DMSO; PanReac AppliChem, Cat. No. A3672) at a ratio of 10:1. Medium was aspirated and 1 mL of 1x trypsin-EDTA was added (prepared from 10× stock; Gibco, Thermo Fisher Scientific, Cat. No. 15400-054). Once cells began to lift off, they were washed in culture medium to ensure complete detachment. The cell suspension was centrifuged at 300g for 5 minutes, and the supernatant was aspirated. Cells were gently resuspended in freezing medium (1 ml for a T25 flask), and 200 µL aliquots were dispensed into each cryovial. The cryovials were placed upright in a polystyrene freezing box and stored at -80°C before being transferred to liquid nitrogen storage within one week.

To thaw the cells, a cryovial of cells was rapidly thawed in a 37°C water bath. The cell suspension (200 µL) was gently pipetted into a T25 flask containing 5ml culture medium. The following day, the medium was changed to remove DMSO.

2.3 Pharmacology

2.3.1 Puromycin

Puromycin dihydrochloride (Santa Cruz, Cat. No. sc-108071) was prepared at a stock concentration of 10 mg/mL in water. Working concentrations were prepared fresh in complete culture medium prior to use. The final concentrations used were 0.1-10 µg/mL made up with fresh complete culture media.

2.3.2 Hygromycin

Hygromycin B (Invitrogen, Thermo Fisher Scientific, Cat. No. 10687010) was supplied as a 50 mg/mL solution in sterile phosphate buffered saline (PBS). For selection, hygromycin was added to the culture medium at final concentrations of 50-800 µg/mL.

2.3.3. Propafenone

Propafenone hydrochloride (Cayman Chemical, Cat. No. 21871) was dissolved to stock concentration of 1mM in extracellular physiological saline solution (PSS) which contained (in mM): 144 NaCl (Fisher Scientific, Product Code S/3160/65), 5.4 KCl (Fisher Scientific, Product Code 10375810; Code P/4280/53), 1 $MgCl_2$, 2.5 $CaCl_2$, 5.6 D-glucose (Sigma, Cat. No. G8270), and 5 HEPES (Thermo Scientific, Cat. No. H3375), adjusted to pH 7.2 with NaOH (Fisher Scientific, Product Code S/4929/53) (Brackenbury & Djamgoz, 2006). The propafenone stock was diluted to working concentrations of 1-100 µM in extracellular PSS.

All drugs used in the experiments are detailed in Table 2.1.

Table 2.1. The drugs utilised in this project.

Drug	Stock Concentration	Working Concentration	Vehicle	Notes
Puromycin	10 mg/mL	0.1-10 µg/mL	H_2O	Selection of transduced cells
Hygromycin	50 mg/mL	50-800 µg/mL	PBS	Selection of transduced cells
Propafenone	1 mM	1-100 µM	PSS (NaOH pH 7.2)	VGSC inhibitor

2.4 Determination of selection concentrations

Cells were harvested using 1x trypsin-EDTA, resuspended in complete medium and seeded in 24-well plates at 5 x 10^4 cells per well in 0.5 mL of medium. Plates were incubated overnight to allow adherence and cell confluency was approximately 50% on the day of antibiotic treatment.

For puromycin selection, the antibiotic was added to the culture at various concentrations: 0, 0.5, 1, 5, 10 µg/ml for both cell lines and additionally 0, 0.1, 0.2, 0.3, 0.4, 0.5 µg/ml for the MDA-MB-468 cell line. Medium containing puromycin was changed every two days. Images were taken daily over 7-8 days at 10x magnification using a Brightfield microscope. Cell numbers were counted by eye in 3 fields of view with 4 technical replicates.

Following lentiviral transduction and puromycin selection, hygromycin selection concentrations were determined for cells expressing dCas9/KRAB. The medium in each well was replaced with fresh medium containing a range of hygromycin concentrations: 0, 50, 100, 200, 400, and 800 µg/ml. Cells were cultured for up to 14 days with medium changes every two days. Daily images were taken at 10x magnification using a Brightfield microscope. Cell confluency was established by eye in 3 fields of view with 4 technical replicates.

2.5 Lentiviral transduction

2.5.1 Control lentivirus

MDA-MB-231 and MDA-MB-468 cells were plated at 1 x 10^5 cells per well in a 12-well plate to achieve 30-50% confluency at the time of transduction. The control lentivirus, pLV[Exp]-EGFP/Puro-EF1A>mCherry (Table 2.2), was diluted in medium at various multiplicity of infection (MOI) values to determine the optimal MOIs of the MDA-MB-231 and MDA-MB-468 cell lines. MOI values were set to 0, 1, 5, and 10 and 0, 1, 3 and 5 respectively (Wei et al., 2022; Gholami et al., 2013). To maximise transduction efficiency, 350µl of medium, the

minimum volume necessary to cover the surface of the plate, was used. After incubation overnight, the virus-containing medium was removed and replaced with fresh, complete culture medium. Cells were cultured for a further 2 days to allow for the appearance of fluorescence. Lentivirally delivered genes are typically expressed within 24-72 hours after transduction (Weber et al., 2025; Xu et al., 2021). Transduction efficiency was then analysed using flow cytometry to quantify eGFP and mCherry expression (Section 2.6).

2.5.2 dCas9-KRAB lentivirus

dCas9 is a catalytically dead version of the CRISPR-associated protein 9 (Cas9). Instead of cutting DNA, dCas9 is employed to bind specifically to target DNA sequences without inducing double-strand breaks which is especially useful when working with cancer cells. The KRAB is a transcriptional repression domain. The dCas9/KRAB complex can be directed to specific DNA sequences, leading to the repression of gene expression at those locations. TNBC cell lines, MDA-MB-231 and MDA-MB-468, were transduced with lentiviral vector to generate dCas9-KRAB expressing cell lines with a selective marker.

Cells were plated as above (1 x 10^5 cells per well, 30-50% confluency) in 12-well plates. On day 1, the dCas9-KRAB vector, pLV[Exp]-EGFP:T2A:Puro-CMV>dCas9/KRAB (Table 2.2, Figure 2.1) was diluted in an appropriate amount of medium and added to both MDA-MB-231 and MDA-MB-468 cell lines at an MOI of 10. Non-transduced cells were maintained in parallel as negative controls. As before, 350 µL of viral medium was used per well, and cells were incubated overnight. On Day 2, the virus-containing medium was replaced with fresh, complete medium. Antibiotic selection began on Day 4 using puromycin at 0.5 µg/ml for MDA-MB-231 and 0.3 µg/ml for MDA-MB-468. Medium was changed every two days during the 5-day selection process. The cells were then maintained in their respective selection dose of puromycin until FACS sorting (Section 2.7)

2.5.3 gRNA Library Lentivirus

On Day 1, MDA-MB-231 and MDA-MB-468 cells were seeded at 1.5 × 10^6 cells per T25 flask in complete medium containing the appropriate puromycin maintenance concentration

(50% of selection concentration). Three flasks were seeded per cell line: a negative control and 2 replicate flasks. Transduction of dCas9-KRAB-expressing cells with the pooled gRNA library (functional viral titre 1.12 x 10^9 TU/mL; Table 2.2, Figure 2.2) occurred on Day 2 using MOI of 0.3 and coverage of 500 (Figure 2.3). The medium was replaced with fresh medium containing 8µg/ml polybrene (Sigma, H9268), and 0.41 µL of lentiviral particles was added per flask. Negative control flasks received no virus.

After 24 hours, the virus-containing medium was removed and replaced with fresh complete medium. On Day 4, hygromycin selection was initiated at 400 µg/mL for MDA-MB-231 and 50 µg/mL for MDA-MB-468, alongside continued puromycin maintenance. Selection continued from Days 5–10, with medium replacement every other day. Cells were transferred to T75 flasks on Day 6. Non-transduced control cells were fully eliminated by Day 7.

On Day 12, the hygromycin concentration was reduced by 50%, and cells were expanded to maintain 300-500x library coverage. The two remaining replicate cultures for both cell lines were then split into three in preparation for the downstream CRISPRi screen under hypoxia.

2.5.4 Hypoxia screen

On Day 13 following transduction with the gRNA library, cells from one flask per replicate were harvested using EDTA-trypsin. Genomic DNA was extracted from this flask per cell line to serve as the baseline (T_0) reference for downstream sequencing analysis (Section 2.9). The remaining two flasks per replicate were cultured under normoxia or hypoxia for 7 days, two experimental replicates per cell line (Figure 2.3). Media changes were performed after 3 days, and dCas9/KRAB-MDA-MB-231 cells were split 1:6 at this point to prevent over-confluency. To ensure effective oxygen depletion, media designated for hypoxia treatment was pre-equilibrated in a hypoxic workstation prior to use. On Day 20, cells from all conditions were collected, washed with PBS (Invitrogen, 14200-067), pelleted, and stored dry at –80°C until genomic DNA extraction (Section 2.9).

Table 2.2. Lentiviral vectors utilised in this project.

Vector Name	Purpose	Selection Markers	Reporter Markers	Plasmid ID
pLV[Exp]-EGFP/Puro-EF1A>mCherry	Optimise transduction efficiency	Puromycin resistance	EGFP, mCherry	VB010000-9298rtf
pLV[Exp]-EGFP/Puro-CMV>dCas9/KRAB	Generate dCas9-KRAB-expressing cell lines	Puromycin resistance	EGFP	VB900088-2936zvb
Single-gRNA CRISPRi Lentivirus Library Targeting 181 Human Genes	Pooled gRNA library for CRISPRi screen	Hygromycin B resistance	None	Lib231220-2041kcc

All lentiviral constructs were designed, pre-packaged in lentivirus and supplied by VectorBuilder.

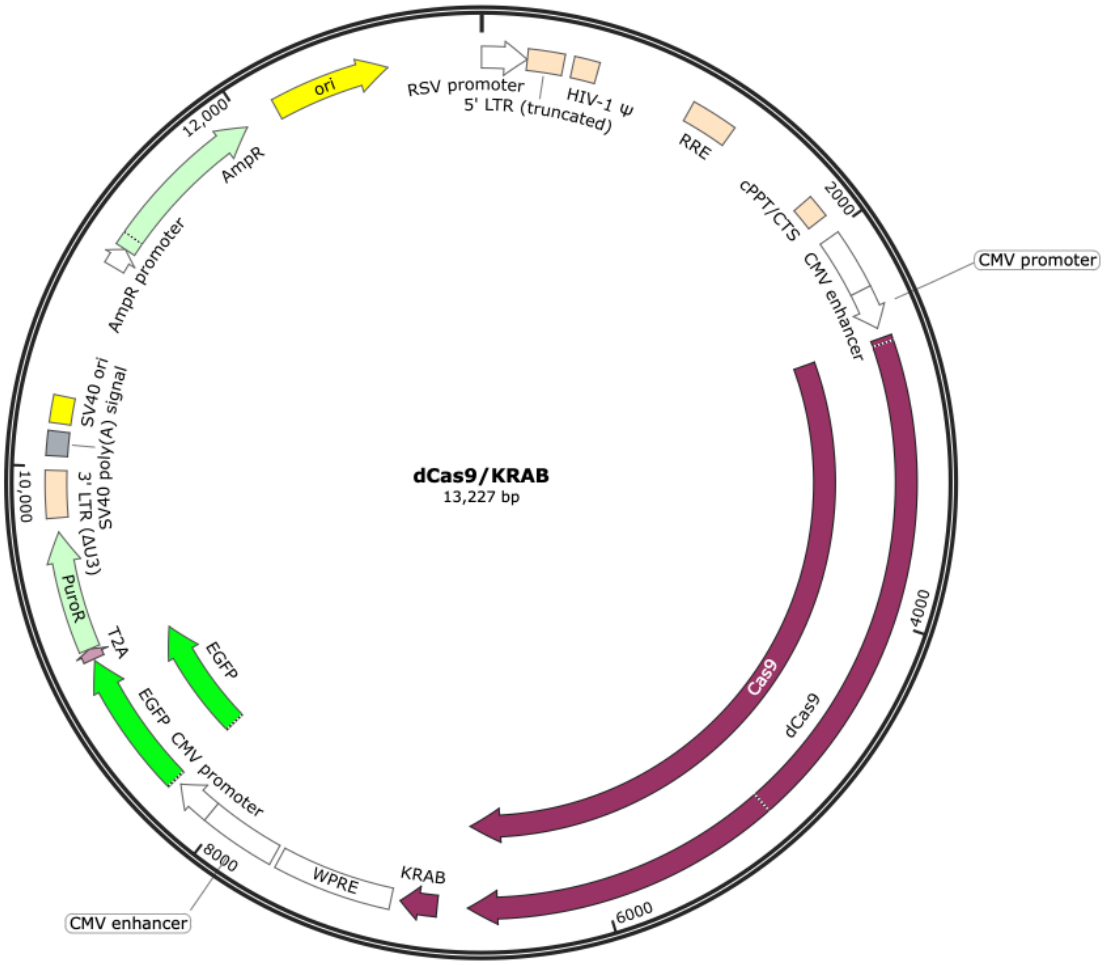


Figure 2.1. ***Plasmid map of the lentiviral expression vector pLV[Exp]-EGFP/Puro-CMV>dCas9/KRAB (VectorBuilder ID: VB900088-2936zvb).***

Mammalian gene expression vector (13,227 bp) designed for lentiviral delivery. Expresses dCas9/KRAB under the control of a CMV promoter. The vector includes an EGFP:T2A:Puro selection marker for fluorescent visualisation and puromycin resistance. The vector was visualised using SnapGene v8.0.2.

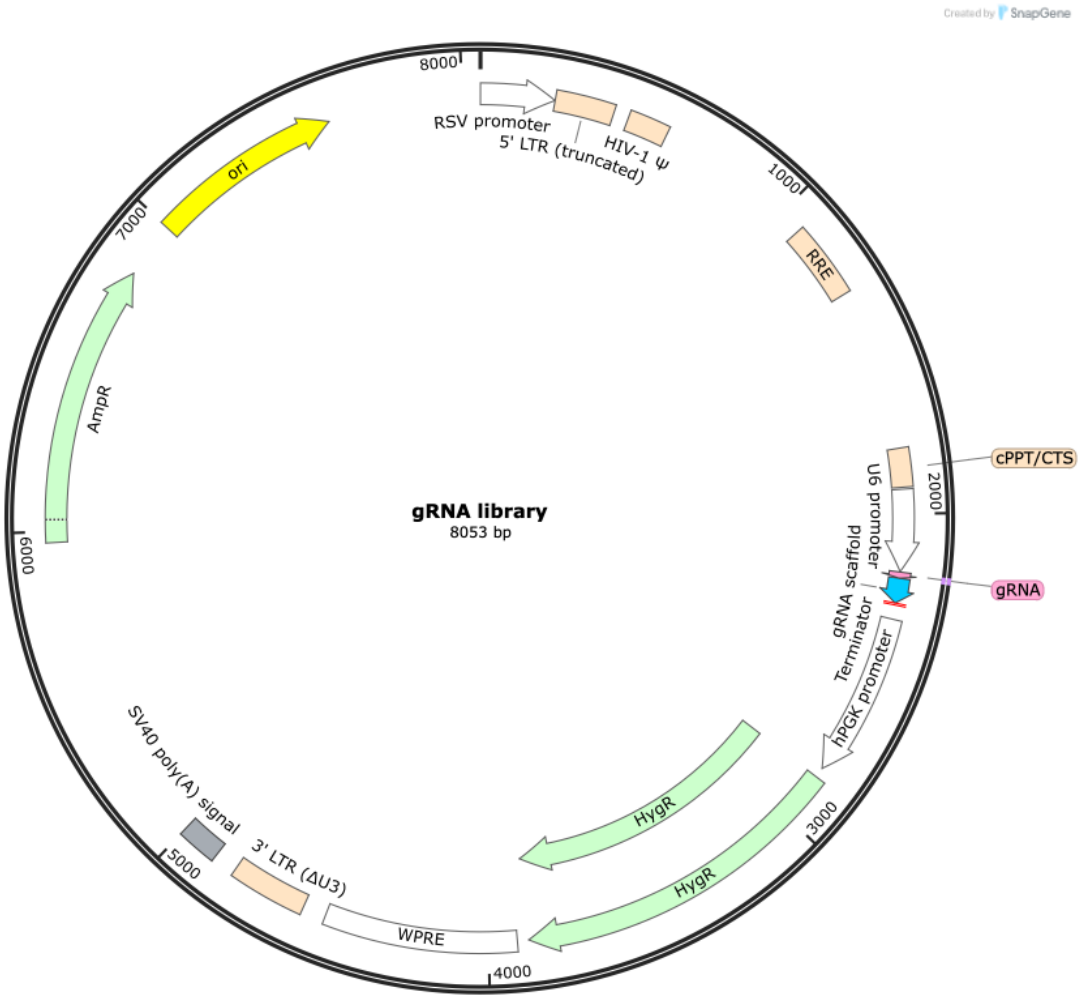


Figure 2.2. ***Plasmid map of the lentiviral vector from the gRNA CRISPRi library (VectorBuilder ID: Lib231220-2041kcc).***

Mammalian lentiviral vector (8,053 bp) expresses gRNAs for CRISPRi screen. The vector is part of a pooled library designed to target 181 human genes. Map generated using SnapGene v8.0.2.

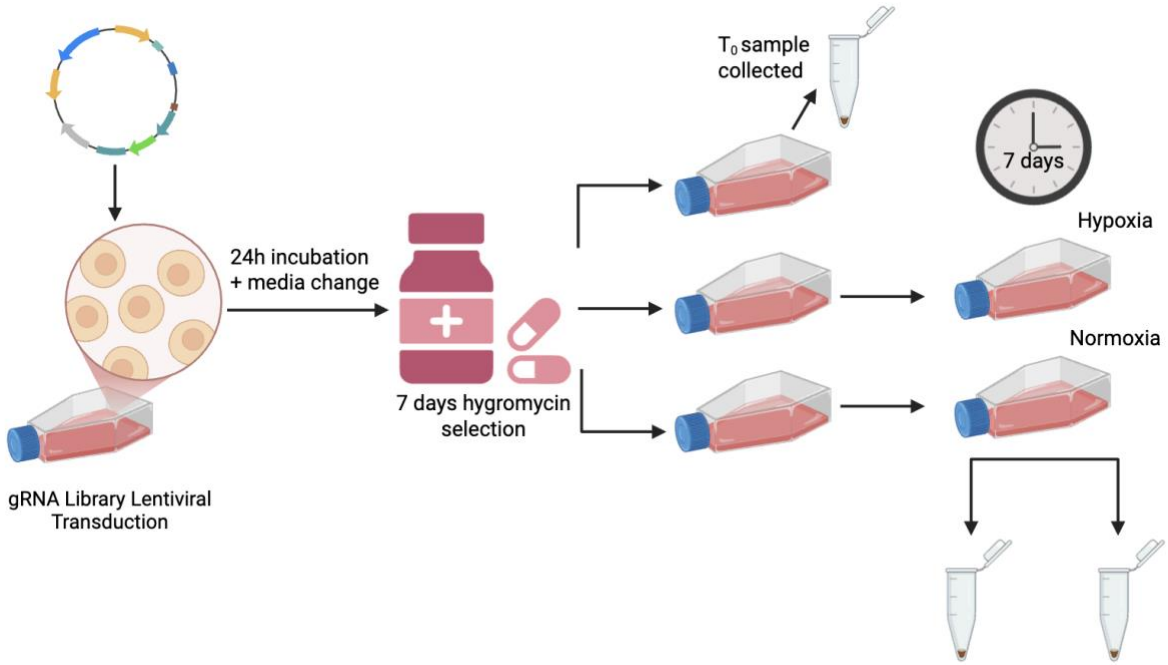


Figure 2.3. Schematic overview of the CRISPRi screen workflow.

Cells were transduced with the lentiviral gRNA library, followed by antibiotic selection with hygromycin. Post-selection, cells were incubated under hypoxic or normoxic conditions before being harvested for downstream DNA extraction and PCR amplification. One replicate shown. Full experimental details are provided in Sections 2.5.3–2.5.4. Figure created in BioRender.

2.6 MOI determination by flow cytometry analysis of transduction efficiency

Three days following transduction with control lentivirus, MDA-MB-231 and MDA-MB-468 cells were rinsed with 1x PBS and harvested from 12-well plates using 1x trypsin-EDTA into falcon tubes for flow cytometry sample preparation; at least 0.5 x 10^6 cells per tube with 0.5 ml 1x PBS. Cells were centrifuged at 300g for 5 minutes then resuspended in 1x PBS and stained with Far Red 638 Fixable Live Dead dye (Beckman Coulter) at 1µl per ml. Cells were incubated at room temperature and protected from light for 30 minutes. Cells were washed in PBS and then fixed in 4% paraformaldehyde (PFA; gift from Genever Lab, University of York), incubated at 4^{o}C and protected from light for 15 minutes. Samples were then washed and resuspended in PBS. Samples were analysed on a Beckman Coulter CytoFLEX S flow cytometer. Green eGFP fluorescence was collected after a 530/30-nm bandpass (BP) filter. mCherry fluorescence was collected after a 610/20 BP filter. Far Red fluorescence from the Live/Dead staining was collected after a 780/60 BP filter. On each sample, a minimum of 10,000 events were collected within the singlet gate. Data was analysed using CytExpert software. Transduction efficiency of the control lentivirus was measured as the percentage of live cells expressing the relevant fluorescent marker.

2.7 Fluorescence-activated cell sorting (FACS) of dCas9/KRAB-transduced cell lines

To prepare for FACS, cells were expanded to a T75 flask, maintaining the appropriate puromycin concentration. Once cultures reached 80% confluence, cells were rinsed with 1x PBS then stained with a sterile DAPI solution (1 µg/mL; gift from Genever Lab, University of York) for 1-5 minutes while protected from light, to distinguish live from dead cells. Cells were then rinsed twice with PBS and harvested using trypsin-EDTA. The trypsin was neutralised with culture medium, and cells were collected by centrifugation, and resuspended in PBS at a concentration of at least 1 x 10^6 cells/mL. Control samples included unstained cells and a tube of culture medium for background control.

The samples were then subjected to FACS:

- The dCas9-KRAB-transduced MDA-MB-231 cells were analysed on the Beckman Coulter Moflo Astrios equipped with four laser lines (405nm, 488nm, 561nm and 633nm). DAPI was detected using the 405nm laser with a 448/59 filter and GFP was detected using a 488nm laser with a 526/52 filter.

- The dCas9-KRAB-transduced MDA-MB-468 cells were analysed on the Beckman Coulter CytoFlex SRT using channel V450-PB 405/45 for DAPI and channel B525-FITC 525/40 for GFP expression.

Gating based on cell size and granularity identified intact, single cells. Live cells from the single cell gate were then gated based on DAPI staining. Live cells were sorted based on their GFP expression, with the top 30% highest GFP-expressing cells collected into FACS tubes containing pre-warmed culture medium. Sorted cells were then cultured in T25 flasks with a maintenance dose of 0.3 µg/mL puromycin. Post-sorting, working cell stocks were frozen. One vial was thawed to test viability and confirm the absence of mycoplasma contamination.

2.8 Microscopy

Following transduction with the dCas9-KRAB lentivirus and FACS, expression of eGFP was captured using a Zeiss AxioVert 200M microscope with a 10×/0.5 NA air objective lens. GFP fluorescence was excited using a filter set with an excitation range of 450–490 nm, and emission was collected between 513–565 nm. Images were captured with a Zeiss AxioCam HRm monochrome camera, and the microscope was controlled using Zeiss AxioVision software. Captured images were analysed using ImageJ2 (version 2.14.0/1.54f). Basic adjustments to brightness and contrast were performed uniformly across images. In addition, rolling ball background subtraction was applied to correct uneven illumination and scale bars were added using the ImageJ scale bar tool.

2.9 DNA extraction

Genomic DNA was purified from each sample using the Monarch® Genomic DNA Purification Kit (New England Biolabs, #T3010) following the manufacturer's instructions. DNA concentration and purity were assessed using a NanoDrop spectrophotometer. Absorbance at 260 nm was used to estimate total nucleic acid content, while the A260/A280 ratio was used to assess protein contamination. All samples showed A260/A280 ratios within acceptable purity ranges (typically ~1.8 for DNA). Some samples had A260/A230 ratios >3.0, which can result from residual EDTA present in the elution buffer. EDTA may chelate divalent cations such as Mg^{2+} and Ca^{2+} associated with DNA, but this is not expected to interfere with downstream applications, such as PCR or Illumina sequencing.

2.10 PCR amplification

To prepare gRNA sequences for Illumina sequencing, nested PCR amplification of the integrated gRNA cassettes was performed. Genomic DNA extracted from cell pellets was used as the template for PCR amplification. An initial PCR was carried out using gRNA_Fwd and gRNA_Rev primers targeting sequences flanking the gRNA region within the lentiviral cassette (Table 2.3). These primers were designed and validated using the NCBI Primer-BLAST tool. step amplified the integrated gRNA region from genomic DNA. A second PCR was performed using Illumina-compatible adapter primers, adding Illumina adapter sequences to the gRNA amplicons, and enabling downstream indexing and library construction. The Adapter_Fwd and Adapter_Rev primers (Table 2.3) contained standard Illumina overhangs as well as degenerate barcode regions (NNNHNNNWNNNH) to allow for sequence diversity during sequencing cluster generation. The adapter sequences were based on designs provided by the Biology Technology Facility at the University of York.

PCR amplification was performed in a 25 µL reaction volume containing nuclease-free water, 1× Q5® High-Fidelity 2X Master Mix (New England Biolabs, cat. #M0492), 0.5 µM of each primer (forward and reverse), and up to 250 ng of template DNA.

The PCR was performed using a Bioer LifePro Thermal Cycler. The thermal cycler was programmed for an initial denaturation of 30 seconds at 98°C, followed by 30 or 15 cycles (for the initial and second rounds of PCR respectively) of 10 seconds at 98°C for

denaturation, 30 seconds at an annealing temperature of 61°C, and 30 seconds at 72°C for extension. A final extension step was carried out at 72°C for 2 minutes, followed by a hold at 10°C.

Table 2.3. PCR primers utilised in this project.

Primer Name	Sequence (5' → 3')	Purpose
gRNA_Fwd	GTGGAAAGGACGAAACACCG	First-round PCR (gRNA-specific) – forward
gRNA_Rev	CGACTCGGTGCCACTTTTTC	First-round PCR (gRNA-specific) – reverse
Adapter_Fwd	TCGTCGGCAGCGTCAGATGTGTATAAGAGACAG ANNNHNNNWNNNHGTGGAAAGGACGAAACACCG	Second-round PCR (Illumina adapter) – forward
Adapter_Rev	GTCTCGTGGGCTCGGAGATGTGTATAAGAGAC AGTCGACTCGGTGCCACTTTTTC	Second-round PCR (Illumina adapter) – reverse

All primers were synthesised by Integrated DNA Technologies.

2.11 Electrophoresis

PCR products were examined by electrophoresis in a 3% (w/v) low-gelling agarose gel (Sigma, A9414) containing SybrSafe (Invitrogen, S33102) in 0.5x TBE buffer (prepared by diluting a premade 10X stock solution; gift from Dr. Malcolm, Brackenbury Lab, University of York). The marker used was a Quick-Load® 1 kb DNA Ladder (New England Biolabs, N0468S). electrophoresis ran at 50V for 2 hours. The electrophoresis gel was examined under blue light. Following each successful PCR amplification, products were cleaned up using the NEB Monarch PCR & DNA Cleanup kit Monarch® PCR & DNA Cleanup Kit (5 µg; NEB, T1030). The purity of PCR products was assessed using a Nanodrop spectrophotometer measuring absorbance at 260 nm, 280 nm, and 230 nm. A260/280 and A260/230 ratios were calculated to evaluate purity and contamination, respectively. Samples with A260/280 ratios between 1.8–2.0 and A260/230 ratios 2.0-2.2 were considered pure. Nuclease-free water (Invitrogen, AM9937) was used as the blank. Samples with a A260/230 ratio outside 2.0-2.2 should not have any negative effect on downstream applications as discussed earlier.

2.12 Library preparation and sequencing

The amplified products were processed by the Genomics Laboratory at the Bioscience Technology Facility, University of York. To enable sample multiplexing for Illumina sequencing, the Genomics team performed an additional 6-cycle PCR to add unique i5 and i7 index sequences using Nextera XT indices (Illumina) and NEBNext Q5 Hot Start HiFi PCR Master Mix (New England Biolabs, M0543). Final PCR products were cleaned using AMPure XP beads (Beckman Coulter) and pooled at equimolar ratios.

Sequencing was performed on an Illumina NovaSeq 6000 platform with short-read technology (2×150 bp paired-end reads). A target read depth of approximately 10 million reads per sample was achieved, covering the gRNA sequences. Sequencing reads were demultiplexed using the i5 and i7 indices for downstream analysis. Sequencing and library preparation were carried out according to the facility's standard protocols. The Genomics Laboratory at the University of York's Bioscience Technology Facility is gratefully acknowledged for technical support and sequencing services.

2.13 Electrophysiology

2.13.1 Whole-cell patch-clamp recording

Cells were seeded onto 13mm glass coverslips 24-96 hours before electrophysiological recording. Whole-cell patch-clamp recordings were used to measure plasma membrane Na^+ currents, following established methods (Nelson et al., 2015; Yang et al., 2012). Borosilicate glass pipettes were pulled using a P-97 pipette puller (Sutter Instrument) and fire-polished to a resistance of 8–10 MΩ when filled with the intracellular recording solution. The intracellular solution consisted of (in mM): 5 NaCl, 145 CsCl, 2 $MgCl_2$, 1 $CaCl_2$, 10 HEPES, and 11 EGTA, with the pH adjusted to 7.4 using CsOH (Alfa Aesar,13233); this solution was prepared as a premade shared stock within the laboratory. The extracellular PSS contained (in mM): 144 NaCl, 5.4 KCl, 1 $MgCl_2$, 2.5 $CaCl_2$, 5.6 D-glucose, and 5 HEPES, adjusted to pH 7.2 with NaOH (Brackenbury & Djamgoz, 2006).

Voltage-clamp experiments were conducted at room temperature using an Axopatch 200B amplifier (Molecular Devices), with series resistance compensation set between 40–60%. Currents were digitized via a Digidata interface (Molecular Devices), low-pass filtered at 10 kHz, and sampled at 50 kHz and analysed using pCLAMP 10.7 software (Molecular Devices) (Leslie et al., 2020). Leak currents were corrected using a P/6 subtraction protocol (Armstrong & Bezanilla, 1977).

Extracellular PSS ± propafenone (1, 3, 10, 30, 100 uM) was perfused into the recording bath at ~2 ml/min using a ValveLink 4-channel gravity perfusion system (AutoMate Scientific). After switching solutions, an equilibration period was allowed before recording to ensure steady-state recordings.

2.13.2 Voltage clamp protocols

Two voltage clamp protocols were used (detailed in Figure legends) (Leslie et al., 2020):

1. To assess the effect of drug perfusion and wash-out on peak current, a simple one-step protocol was used. Cells were held at -120 mV for 250 ms, followed by a single depolarising step to -10 mV for 50 ms.
2. To assess the voltage-dependence of activation, cells were held at -120 mV for 250 ms and then depolarised from -120 mV and +30 mV in 10 mV increments for 50 ms.

To analyse channel inactivation, current traces were fitted with a double exponential function using GraphPad Prism 9.0.2.:
$I = A_f \exp(-t/\tau_f) + A_s \exp(-t/\tau_s) + C$, where A_f and A_s are maximal amplitudes of the slow and fast components of the current, τ_f and τ_s are the fast and slow decay time constants and C is the asymptote (Leslie et al., 2020).

2.14 Data and statistical analysis

2.14.1 CRISPRi screen analysis

The sequencing data (FASTQ files) generated from Illumina short-read sequencing were analysed using the nf-core CRISPRseq v2.3.0 pipeline (https://nf-co.re/crisprseq/2.3.0/), designed for CRISPR-Cas9 screening data analysis (Ewels et al., 2020; Sanvicente-García et al., 2023). The pipeline supports three algorithms for detecting gene essentiality: MAGeCK RRA (Robust Ranking Aggregation) (Kolde et al., 2012), MAGeCK MLE (Maximum Likelihood Estimation) (Li et al., 2015), and BAGEL2 (Hart et al., 2014). For this study, MAGeCK RRA was used to identify gene essentiality from the CRISPRi screen data.

MAGeCK RRA is a robust statistical method that ranks genes based on the enrichment or depletion of their gRNAs across multiple samples and identifies genes significantly affected by the enrichment treatment. The pipeline was executed using a design matrix we set up which conducted three separate comparisons of the three samples (hypoxia, normoxia and T0 baseline). gRNA counts from each condition were normalised and statistically compared against scrambled negative control gRNAs using the MAGeCK RRA algorithm, which employs a robust ranking aggregation method that ranks gRNAs based on their depletion, aggregates these ranks across replicates, and calculates $\log_2$ fold changes and associated

p-values. Genes with gRNA depletion in hypoxia compared to normoxia were interpreted as positive contributors to proliferation under hypoxia.

An additional data analysis of gRNA depletion was performed by the Data Science team at the Bioscience Technology Facility, University of York, to complement the initial gRNA depletion analysis. The initial analysis focused on comparing the normoxia and hypoxia conditions independently, using the nf-core CRISPRseq v2.3.0 pipeline (https://nf-co.re/crisprseq/2.3.0/). The baseline T_0 samples were used as a reference to control for initial gRNA representation and potential technical biases. By analysing normoxia and hypoxia samples separately against the T_0 baseline, the analysis aimed to identify condition-specific effects on gene essentiality. Following processing with the MLE algorithm, results comparing hypoxia versus normoxia were visualised using the MAGeCKFlute ScatterView tool. A ninesquare model was applied to categorise genes into nine distinct groups based on their relative enrichment or depletion across conditions. Classification into the nine groups distinguishesd hypoxia-specific, normoxia-specific, and condition-independent gene effects on proliferation.

2.14.2 Statistical analysis

Data are presented as mean and SEM unless stated otherwise. Statistical analysis was performed on the raw (non-normalized) data using GraphPad Prism 9.0.2 or R (R Core Team, 2023) via RStudio 2023.03.0+386 (Posit, 2023).

Kaplan–Meier survival analyses were performed in R using the survival (Therneau, 2023) and survminer (Kassambara et al., 2021) packages, and statistical differences between survival curves were assessed using the log-rank (Mantel–Cox) test.

Electrophysiological data were analysed in GraphPad Prism. Multiple comparisons were made using ANOVA and Tukey post-hoc tests, unless stated otherwise. Pairwise statistical significance was determined with Student's paired t-tests. Where data were missing or unbalanced, a Linear Mixed Effects (LME) model was implemented in R using the lme4 package (Bates et al., 2015).

For exploratory and visualisation analyses in R, the following packages were used:

- ggplot2 (Wickham, 2016) for scatter plots, boxplots, volcano plots, and threshold line visualisation.
- ggrepel (Slowikowski, 2023) for improved label readability.
- dplyr (Wickham et al., 2023) and tidyr (Wickham & Girlich, 2023) for data wrangling, filtering, ordering, and summary statistics.
- VennDiagram (Chen & Boutros, 2011) and grid (R Core Team, 2023) for Venn diagram plotting.

Results were considered significant at $P < 0.05$.

3. Results

3.1 Generating a target list of Na+ channel genes for a pooled gRNA library

To investigate the effects of hypoxia on Na^+ channels in the context of TNBC cell proliferation, a pooled gRNA library was curated for a CRISPRi screen. An exhaustive list of genes encoding Na^+ channels and their auxiliary subunits was generated through a comprehensive literature search (Leslie et al., 2019; Nishimura and Naito, 2008; Andrejew et al., 2020; Chang et al., 2019; Samanta et al., 2018) (Table S1). Genes were included if they encoded channel subunits with a known or putative role in Na^+ transport, regardless of whether they function as pore-forming α-subunits or auxiliary/regulatory subunits. Both voltage-gated and non-voltage-gated Na^+ channel genes were considered. Inclusion criteria extended to genes supported by experimental evidence, sequence homology, or annotated functional roles in Na^+ permeability or channel assembly (Leslie et al., 2019; Nishimura and Naito, 2008; Andrejew et al., 2020; Chang et al., 2019; Samanta et al., 2018).

A set of controls was included in the library design. Three scrambled gRNA sequences served as negative controls (Table S1). As positive controls for hypoxia-dependent cell fitness, gRNAs targeting *HIF1A* and *HIF2A* were included. Both genes encode transcription factors that mediate the cellular response to hypoxia (Walmsley et al., 2005; Befani and Liakos, 2018; Cavadas et al., 2013; Kozal and Krześlak, 2022). Therefore, under hypoxic culture conditions, knockdown of these genes was expected to reduce proliferation and/or viability, leading to gRNA depletion over time. For positive controls, genes identified as essential for survival of MDA-MB-231 and MDA-MB-468 cell lines were included (DepMap, 2024). Specifically, *SLC16A3*, *AP2B1, NAMPT* and *FKBP9, GNB2, GNG5* respectively (Table S1).

3.2 Establishing dCas9-KRAB expressing cell lines

To generate MDA-MB-231 and MDA-MB-468 cell lines expressing the dCas9-KRAB fusion protein, a lentiviral vector containing dCas9-KRAB fusion protein, puromycin resistance and eGFP cassettes was used (Table 2.2, Figure 2.1). In preparation for selection following

transfection, dose-response experiments were conducted to identify the lowest concentration of puromycin needed to kill all cells within five days. The MDA-MB-231 cell line exhibited complete cell death at the lowest effective dose of 0.5 µg/ml (Figure 3.1A). For the MDA-MB-468 cell line, 0.3 µg/ml was the lowest effective dose (Figure 3.1B). These puromycin concentrations were employed for selecting transduced cells expressing the dCas9/KRAB vector following transfection.

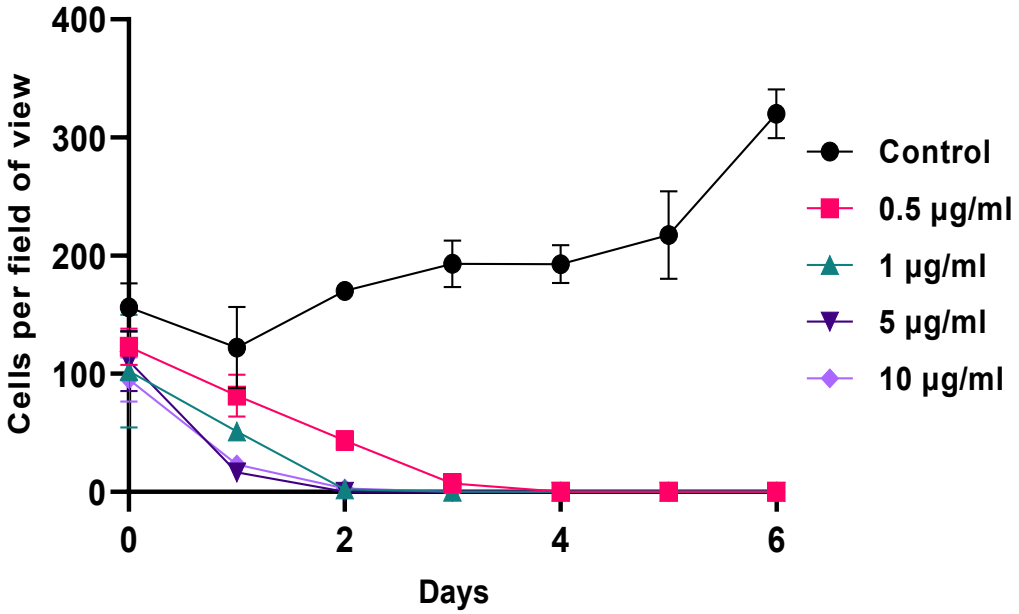
The determination of the multiplicity of infection (MOI) using a control lentiviral vector including eGFP and mCherry selection markers in MDA-MB-231 and MDA-MB-468 cells aimed to assess the influence of varying MOIs on transduction efficiency. The goal was to strike a balance between achieving a high transduction rate and avoiding potential cytotoxicity. Flow cytometry analysis, looking at eGFP and mCherry expression and utilising a Far Red 638 fixable Live Dead dye, showed that across all MOIs, the lentiviral transduction process did not negatively impact viability of either cell line (Figures 3.2A-C, S1, S2). An MOI of 10 emerged as the optimal condition for MDA-MB-231 cells, achieving approximately 70% transduction efficiency, which was used for future lentiviral transductions (Figures 3.2D, S1). Due to limited control lentivirus, the largest MOI value tested in MDA-MB-468 cell line was 5. The highest transduction efficiency achieved in MDA-MB-468 was 15% (Figures 3.2E, S2). Low transduction efficiency could be explained by the large titre drop commonly observed after repeated freeze-thaw cycles of lentivirus. A transduction efficiency of ≥30% was targeted to ensure expression of dCas9-KRAB across the cell population. Low efficiencies (<30%) can result in uneven selection and clonal bias, whereas higher efficiencies facilitate the generation of a stable, representative population (Sanson et al., 2018). With plenty of dCas9/KRAB-lentivirus remaining but limited control lentivirus, MDA-MB-468 cells were transfected at an MOI of 10.

dCas9-KRAB expressing MDA-MB-231 and MDA-MB-468 cells were generated for subsequent CRISPRi screens. Both cell lines were individually transduced at MOI 10 with a lentiviral vector containing the dCas9/KRAB construct (Table 2.2, Figure 2.1). Following antibiotic selection with the optimal concentration of puromycin, the dCas9-KRAB expressing cell lines were further refined using FACS to collect the top 30% of cells expressing dCas9-KRAB (Figure 3.3). In summary, two TNBC cell lines stably expressing dCas9/KRAB were generated to be used in the CRISPRi screens (Figure 3.4).

Functional expression of the dCas9-KRAB fusion protein in MDA-MB-231 and MDA-MB-468 cell lines was indirectly confirmed by Dr. Weiye Zhao (Holding Lab, University of York) using a commercial validation kit (Merck) (W. Zhao, personal communication, 24 February 2025).

dCas9-KRAB-expressing cells were transduced with lentivirus encoding a gRNA targeting the RAB1A gene. RAB1A is a well-established reference gene, making it a reliable indicator of dCas9-KRAB-mediated transcriptional repression (Xu et al., 2019). RT-qPCR analysis of cDNA from these cells showed reduced RAB1A expression levels in both MDA-MB-231 and MDA-MB-468 dCas9-KRAB-expressing lines, indicating successful knockdown and thus functional dCas9-KRAB activity (Figure 3.5). This confirmed that the dCas9-KRAB fusion protein was functional in both cell lines. Knockdown was not observed in the MDA-MB-231 cells transduced at MOI 1, likely due to inefficient transduction. However, knockdown was successful at other MOI values (Figure 3.5) (W. Zhao, personal communication, 24 February 2025).

A



B

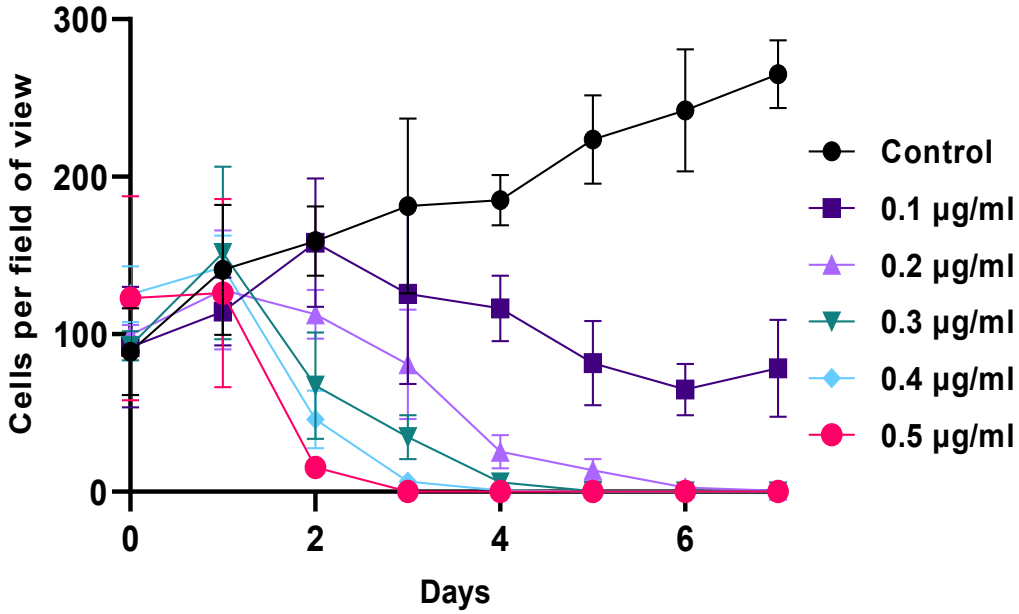


Figure 3.1. Dose-response experiments of puromycin.

(A) Total number of MDA-MB-231 cells per field of view plotted against days of treatment with drug. (B) MDA-MB-468 cells per field of view plotted against days of treatment with puromycin. Data are presented as mean ± SEM (n = 1, 4 technical replicates).

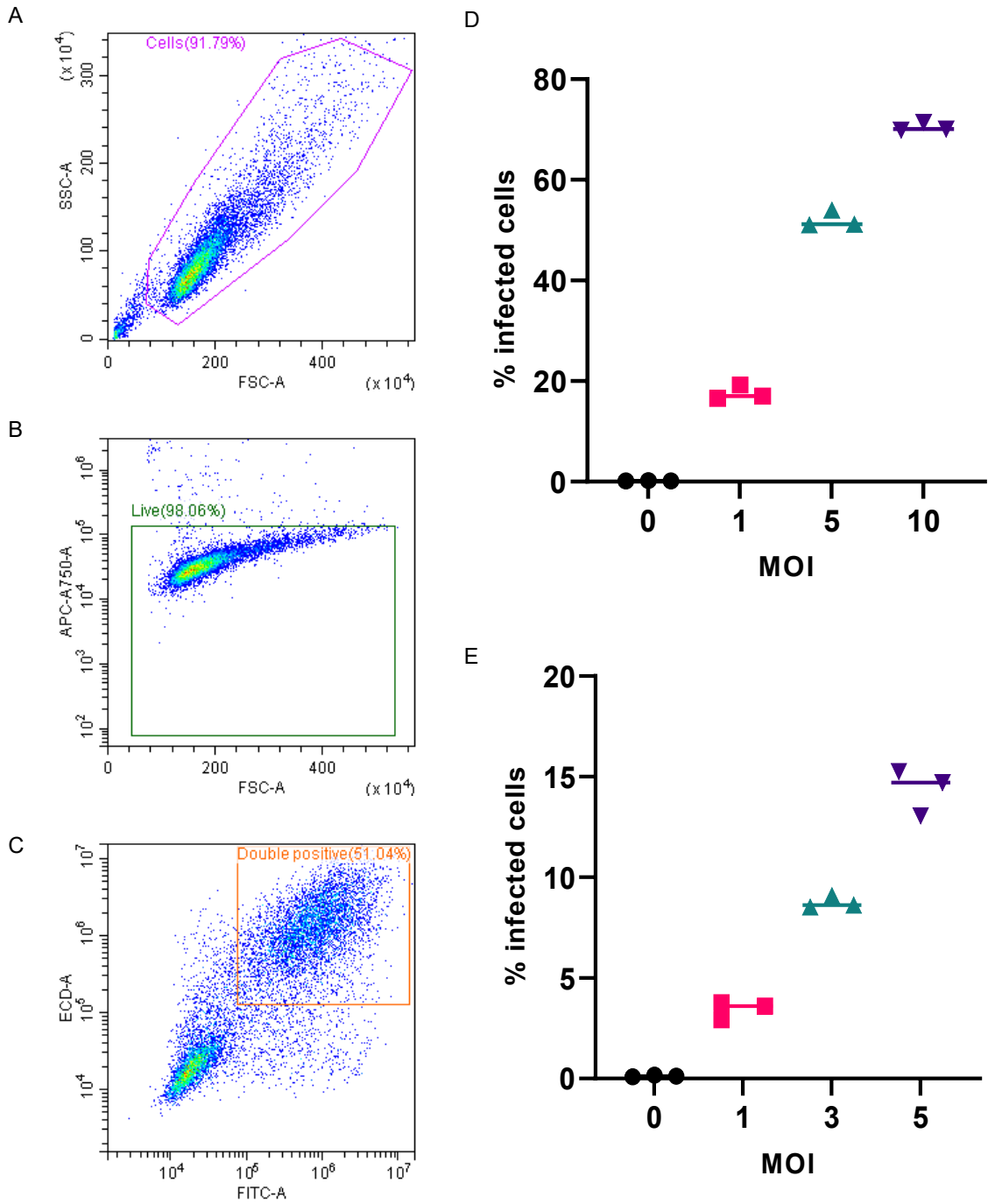


Figure 3.2. Transduction efficiency with eGFP/mCherry control lentivirus.

(A-C) Representative gating strategy. (A) The cells were gated based on cell size and granularity (forward-scatter-area (FSC-A); side-scatter-area (SSC-A)). (B) Live cells were then gated from FSC-A and APC-A750 (Far Red 638 fixable Live Dead dye). (C) The live cells were then displayed on a dot plot, with FITC-A and EDC-A intensity to gate cells positive for both e-GFP and mCherry expression respectively. (D) Percentage of MDA-MB-231 cells infected when transfected at MOIs of 0, 1, 5 and 10. (E) Percentage of MDA-MB-468 cells infected when transfected at MOIs of 0, 1, 3 and 5. Double positive e-GFP and mCherry expression indicates infected cells. The data are presented as the mean (n = 1, 3 technical replicates).

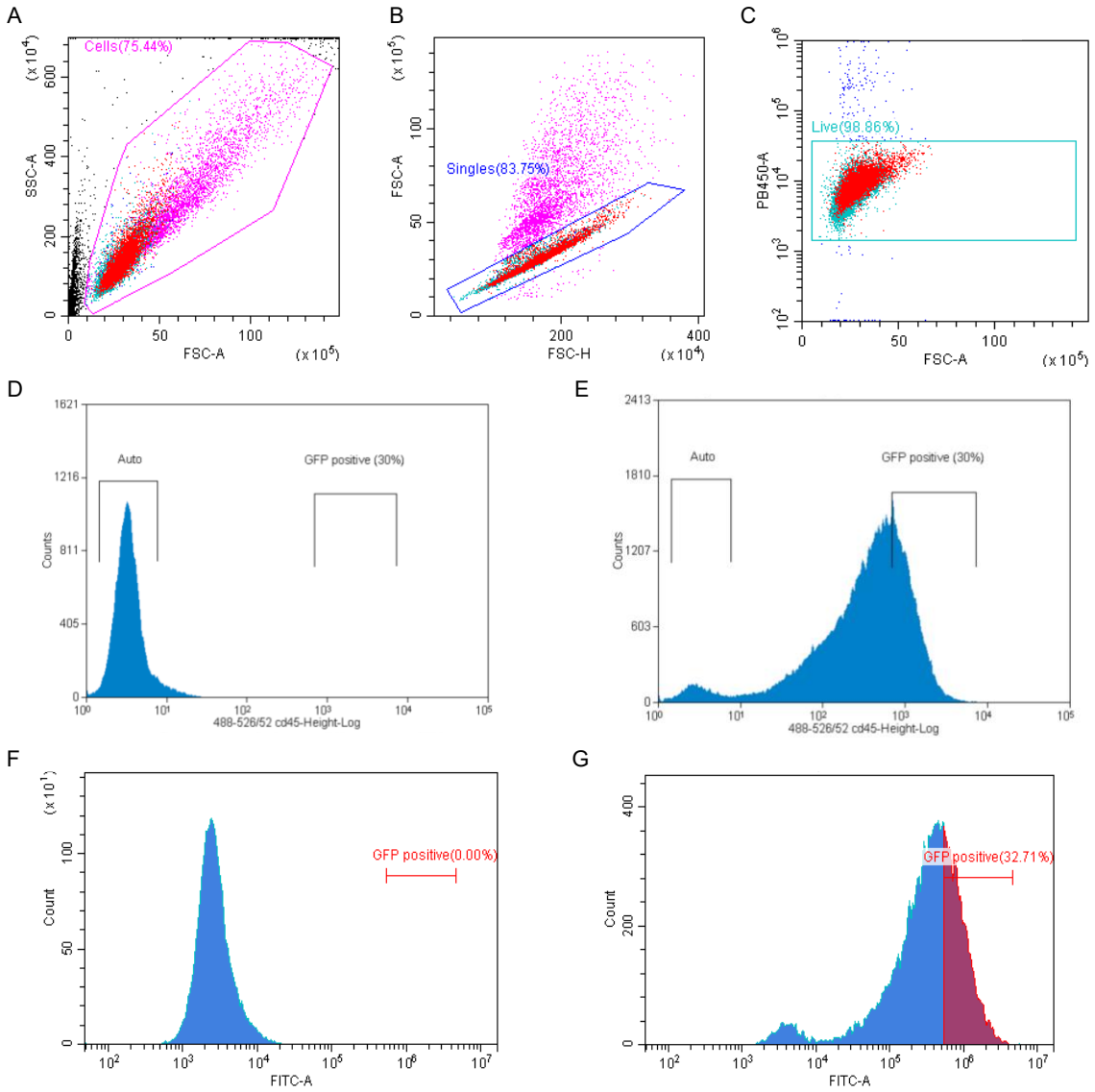


Figure 3.3. FACS of dCas9/KRAB-expressing cell lines.

(A-C) Representative gating strategy for FACS after transduction with dCas9/KRAB lentiviral vector. (A) Cells were gated based on cell size and granularity (forward-scatter-area (FSC-A); side-scatter-area (SSC-A)). (B) Single cells gated from FSC-A and forward-scatter-height (FSC-H). (C) Single cells then displayed on a dot plot, with FSC-A and Live/Dead dye (PB450-A) intensity, to gate live cells. (D-G) Live, single cells sorted by FACS based on GFP expression. (D) Non-transduced and (E) transduced MDA-MB-231 cells analysed through 488-526/52 filter to identify top 30% GFP positive cells and autofluorescence (Auto). GFP expression of (F) non-transduced and (G) transduced MDA-MB-468 cells analysed through FITC filter to gate top 30% GFP positive cells and autofluorescence (Auto).

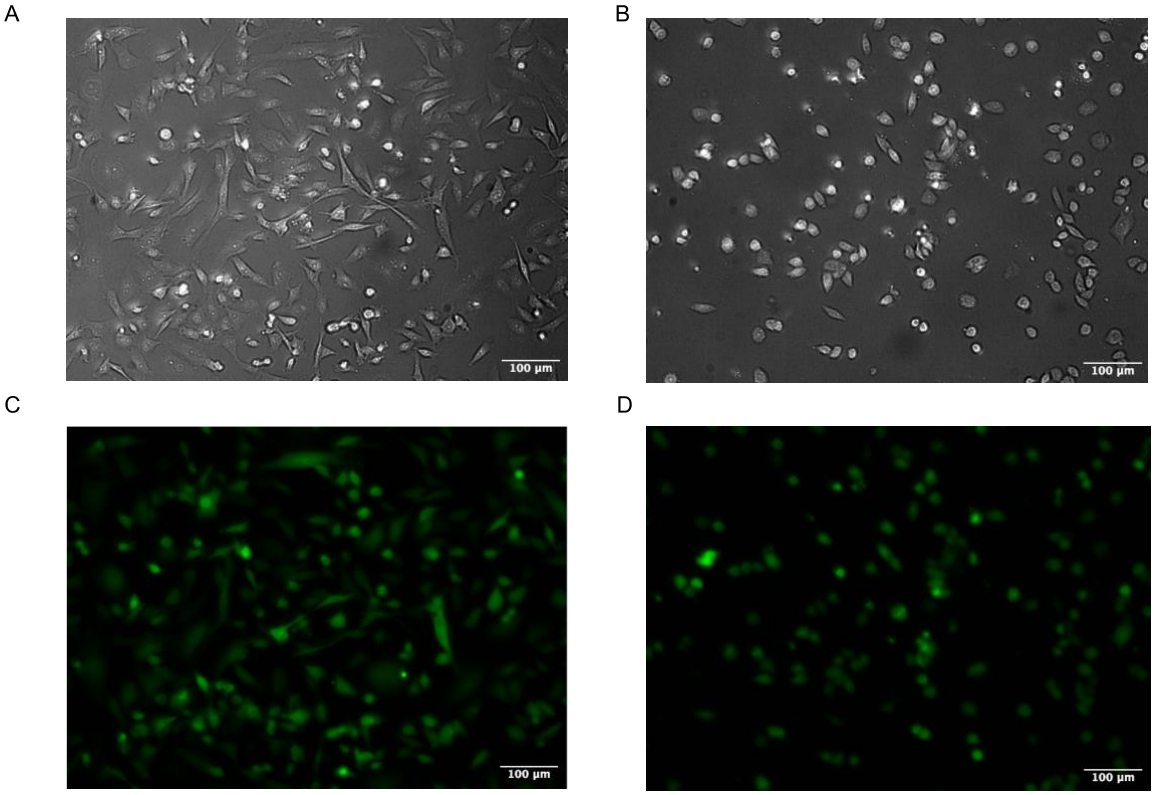


Figure 3.4. Established dCas9-KRAB cell lines.

Brightfield images of dCas9/KRAB-expressing (A) MDA-MB-231 and (B) MDA-MB-468 cells. e-GFP expression in (C) MDA-MB-231 and (D) MDA-MB-468 cells visualized using the FITC channel.

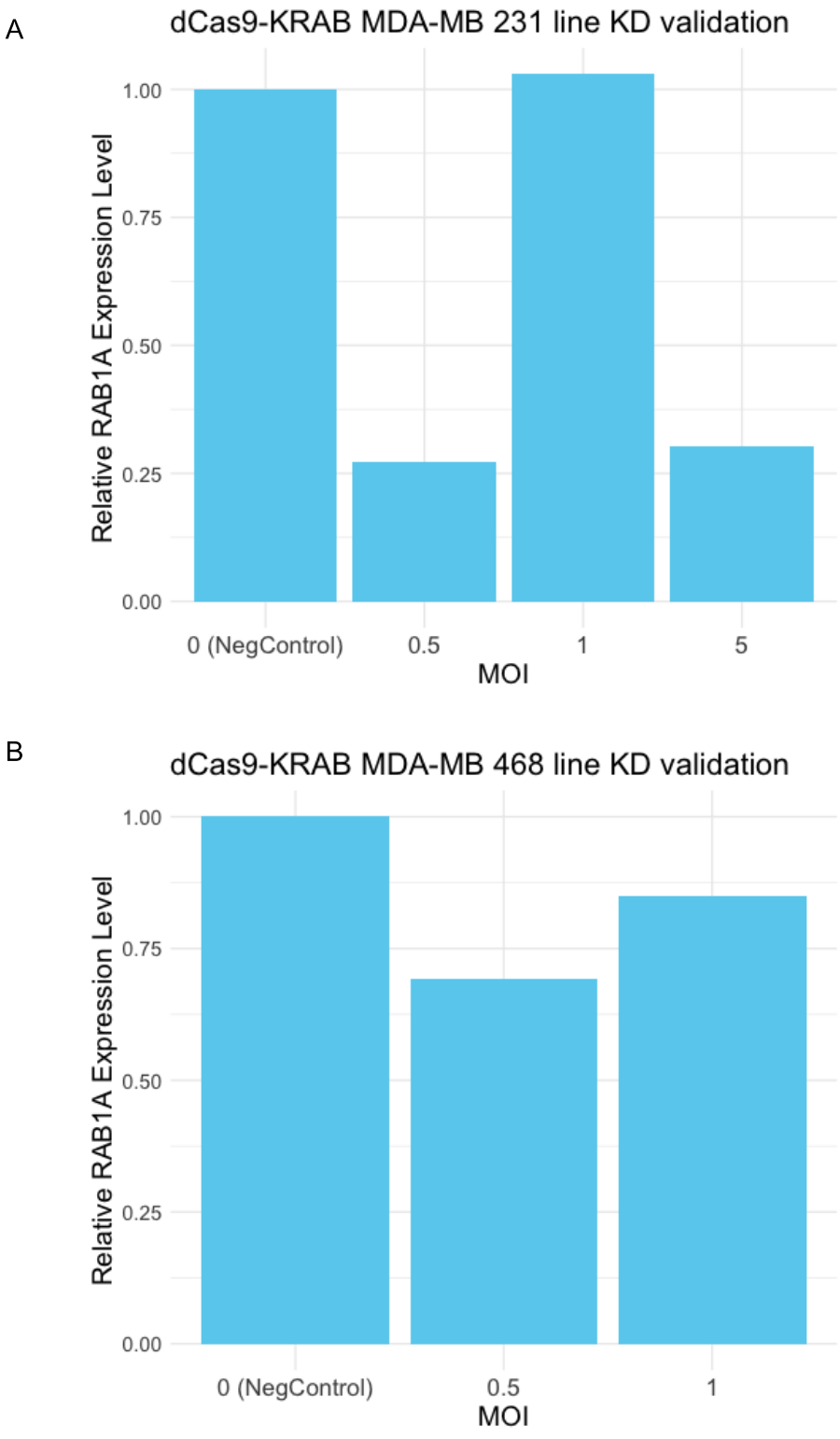


Figure 3.5. dCas9-KRAB-expressing cell line validation.

RAB1A knockdown in (A) MDA-MB-231 and (B) MDA-MB-468 cells using Merck testing kit. Both cell lines expressing dCas9-KRAB were transduced using the same RAB1A-targeting gRNA lentiviral constructs. Cells were transduced with varying multiplicities of infection (MOIs): 0, 0.5, 1, and 5. Knockdown efficiency was assessed by measuring relative RAB1A expression level. Data from a single experiment (N = 1).

3.3 Transfection with gRNA library

The gRNA library lentiviral vector contained a hygromycin resistance cassette for selection of cells transduced with gRNA library (Table 2.2, Figure 2.2). To establish the selection conditions needed following transduction of the gRNA library into the dCas9-KRAB-expressing cell lines, dose-response experiments were conducted to determine the lowest concentrations of hygromycin to elicit complete cell death within 7 days. The lowest effective dose in the MDA-MB-231 cell line was 400 µg/ml (Figure 3.6A). For the MDA-MB-468 cell line, all doses induced cell death within 7 days with 50 µg/ml being the lowest effective dose (Figure 3.6B). These hygromycin concentrations were used to select cells transduced with the gRNA library.

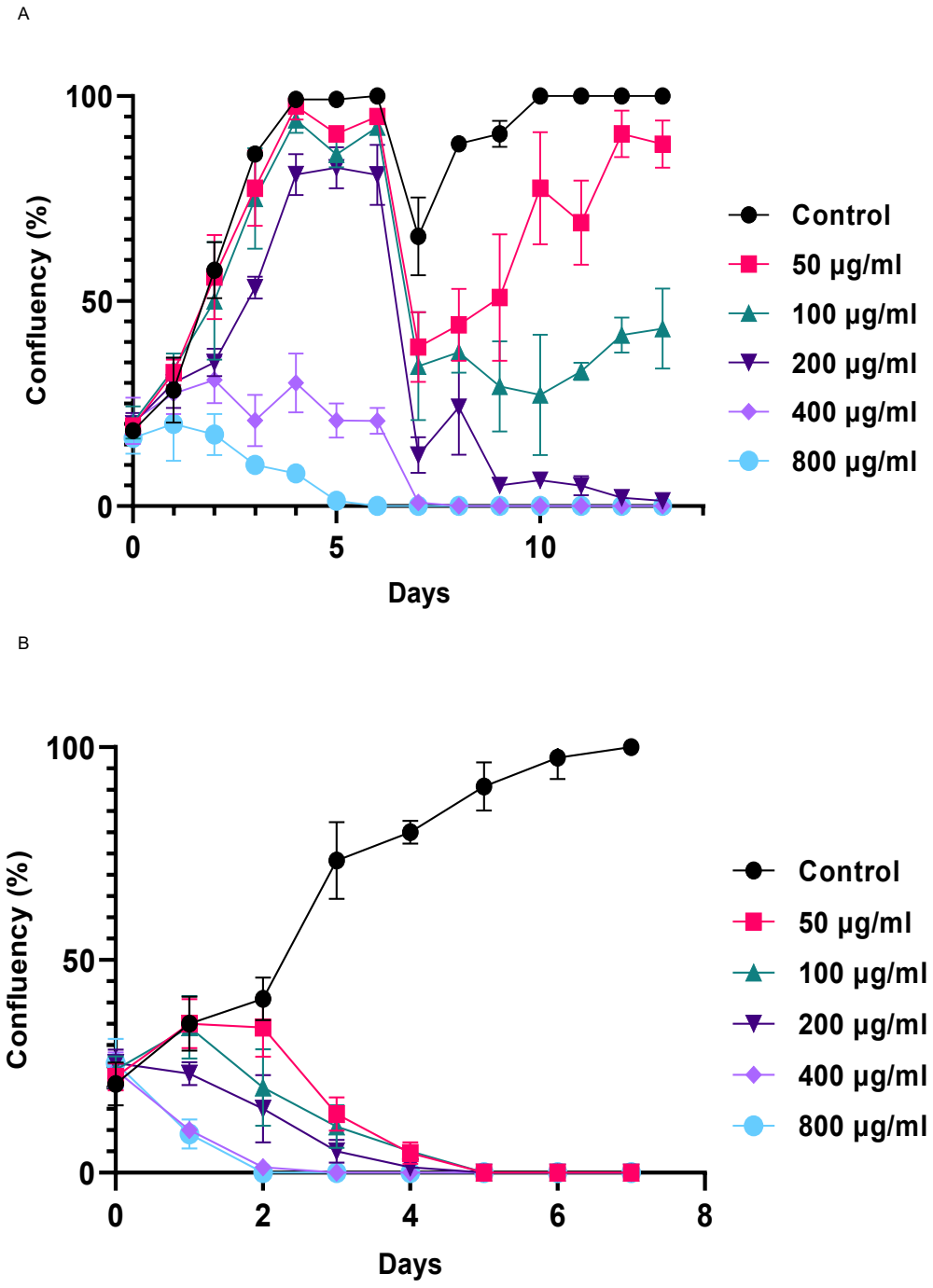


Figure 3.6. Dose-response experiments of hygromycin.

(A) Confluency of MDA-MB-231 cells plotted against days of treatment with drug. (B) Confluency of MDA-MB-468 cells plotted against days of treatment with drug. Data are presented as mean ± SEM (n = 1, 4 technical replicates).

3.4 Selection under hypoxia

Following transduction with the gRNA library and selection with hygromycin for 7 days, both cell lines underwent 7-day selection in either hypoxia or normoxia incubation conditions as outlined in Figure 2.3. DNA was harvested from both conditions, as well as day 0 samples, and nested PCR was performed. The initial round of PCR amplified the gRNA cassettes (Supplementary Figure 3A-B). The second round of PCR added Illumina adapter sequences to the products (Supplementary Figure 3C-D). These PCR products were then sent for indexing, adding barcode sequences and i7/i5 sequences, before Illumina sequencing. The products from the first round of PCR appeared smaller than expected, approximately 118 bp instead of the expected 151 bp (111 bp region being amplified and two primers, both 20 bp). However, the second round PCR product is 232 bp as expected, 151 bp plus the 81 bp from Illumina adapters, suggesting the end product and was not affected and that the first product appearing smaller than expected is likely an artefact of the gel running.

3.5 Quality control report for the CRISPRi screen

The quality control analysis of the sequencing data demonstrated low technical bias, as reflected by the proportion of unique and duplicate read counts. Approximately 3% of sequencing reads corresponded to duplicate counts with the remaining 97% of sequencing reads corresponding to unique counts (Figure 3.7). A high percentage of unique reads indicates that most of the sequencing data represents unique gRNAs, suggesting robust diversity within the library and comprehensive coverage of the gRNAs, enabling accurate measurement of gRNA abundance. The remaining 3% of duplicate reads are typically a result of PCR amplification during library preparation. A low level of duplicate reads is standard amplification bias, confirming that the PCR step did not over-represent specific sequences. The 45–50% GC content suggests that sequencing quality is unlikely to be affected by GC bias (Figure 3.7).

To identify potential outliers, the gRNA deviation (gRNA count normalised to the gene mean) was plotted against the ranked standard deviation (SD), sorted from largest to smallest (Figure 3.8). The distribution seen across all samples (hypoxia, normoxia and day 0) for both MDA-MB-231 (Figure 3.8A-C) and MDA-MB-468 (Figure 3.8D-F) cell lines is typical and does not raise any concern of outliers.

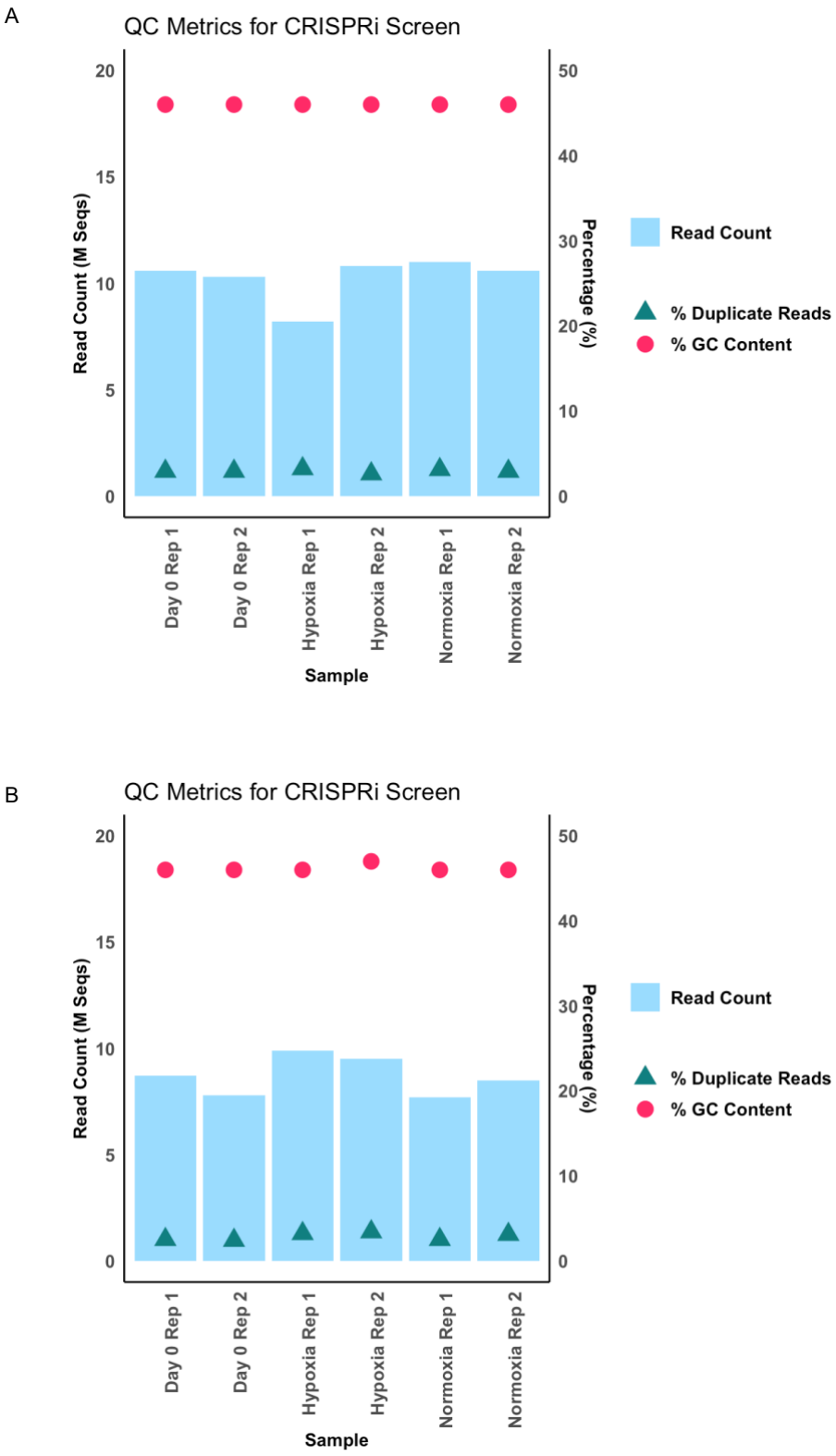


Figure 3.7. FastQC analysis.

QC data for each sample in (A) MDA-MB-231 and (B) MDA-MB-468 cell lines. Overall read counts are shown as well as duplicate reads and GC content shown as percentage. Duplicate read counts are an estimate only. Figure generated using data obtained through the Nextflow-core pipeline FastQC for CRISPR screening. Two replicates per condition are shown as individual bars.

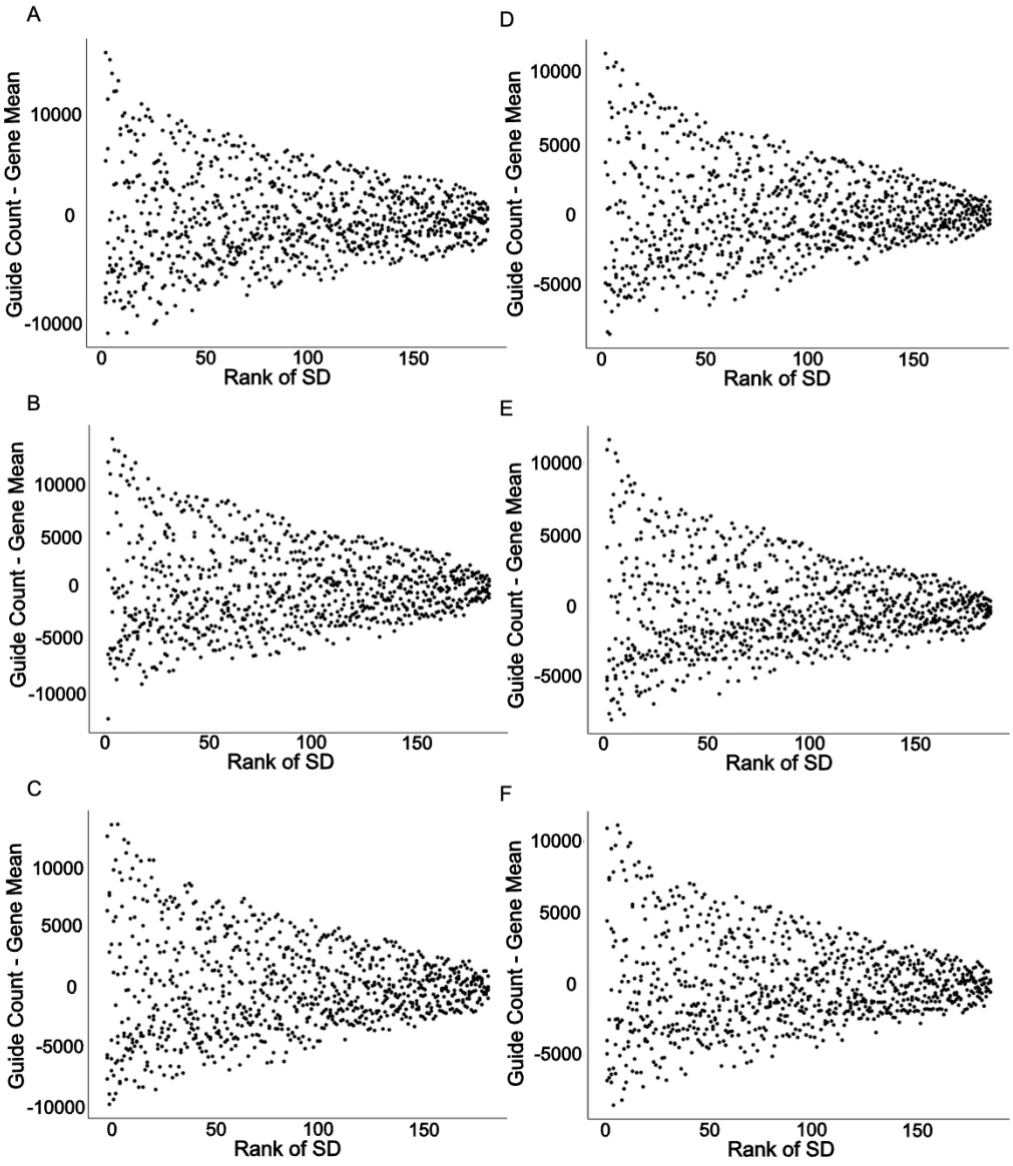


Figure 3.8. gRNA deviation vs. ranked SD.

gRNA deviation (gRNA count normalised to gene mean) is plotted against the ranked SD, sorted from largest to smallest. gRNA deviation data shown for MDA-MB-231 cells from (A) hypoxia, (B) normoxia, and (C) day0 samples as well as MDA-MB-468 cells from (D) hypoxia, (E) normoxia, and (F) day0 samples. Each plot represents combined data from two replicates per condition.

3.6 Depleted gRNAs under hypoxia in MDA-MB-231

A three-way comparison of gRNA sequence representation observed between hypoxia, normoxia and day 0 samples in MDA-MB-231 was conducted. Significant hits were determined by a p-value below 0.05 and an FDR value below 0.05. FDR is a type of adjusted p-value. FDR was used to determine significance, then p-value was used if the FDR gave no results.

Before analysing candidate hits, we first examined control gene performance to evaluate the reliability of the screen. gRNAs targeting essential genes should show consistent depletion over time, while non-targeting controls should remain stable. However, gRNAs were not consistently depleted under either condition against day 0 (when plotted individually and as mean of all 5 gRNAs) (Figure 3.9). Interestingly, HIF1α and HIF2α, included as hypoxia-specific controls, were not depleted under hypoxia (Figure 3.9). Lack of depletion may reflect that *HIF1α* and *HIF2α* are regulated at the protein level rather than at the transcriptional level (Wang et al., 1995; Semenza, 2003). Thus, *HIF1α* and *HIF2α* may not be strongly affected by CRISPRi transcriptional repression. These surprising patterns in the control genes suggest issues with gRNA library design, off-target effects or possibly compensatory issues, particularly between HIF1a and HIF2a. There could potentially be issues with the experimental design such as insufficient selection pressure during enrichment. These results highlight caveats when interpreting screen outcomes.

With this context, we next examined gRNA depletion at the gene level. When all five gRNAs per gene were considered, no genes exhibited significant gRNA depletion under hypoxic conditions compared to under normoxia or under normoxia compared to day 0 (Figure 3.10A,C). Only *SLC34A1* encoding for sodium-dependent phosphate transporter 2A (NaPi-IIa), which is involved in phosphate homeostasis, was significantly depleted in hypoxia compared to day 0 (Figure 3.10B).

Since there were no significant results for gRNA depletion data grouped at the gene level when all 5 gRNAs were considered, we plotted the $\log_2$ fold change and -log10(p-value) of the most depleted gRNA for each gene, similar to the approach employed by Tsung et al. (2024), where the top three sgRNAs out of ten targeting each lncRNA were used to identify screen hits. Using the top three gRNAs highlights the most impactful gRNAs to identify significant perturbations, avoiding dilution from less effective gRNAs (Figure 3.11). However, this approach assumes that the most depleted gRNA is a reliable indicator of the gene's

impact, which may not always be the case due to potential off-target effects. Using the top-depleted gRNA, more genes were identified as screen hits in the hypoxia against normoxia comparison (Figure 3.11A). *SCN5A* was identified with a significantly depleted gRNA under hypoxia compared to normoxia in the MDA-MB-231 cell line. *SCN5A* encodes $Na_v1.5$ and is upregulated by hypoxia with increased inward Na^+ current under hypoxic conditions (Plant et al., 2020; Ju et al., 1996; Hammarström and Gage, 2002). Other hits include solute carrier genes such as *SLC10A5* and *SLC38A5*. *SLC38A5* encodes for SN2/SNAT5, a sodium-coupled neutral amino acid transporter which transports asparagine, histidine, glutamine, glycine, serine, and methionine and is involved in regulating the glutamate and glutamine cycle in the brain, (Nakanishi et al., 2001; Nakanishi et al., 2001; Ayka and Şehirli, 2020). *SLC10A5* encodes for a member of the SLC10 family also known as the sodium/bile acid cotransporter family (Fernandes et al., 2007). The top-depleted gRNA targeting *SLC10A5* was also depleted under hypoxia compared to day 0 (Figure 3.11B). Other members of the SLC38 family, *SLC38A8* and *SLC38A10* had gRNA depletion under normoxia compared to day 0 (Figure 3.11C). *SLC38A8* encodes a putative glutamine transporter (Kuht et al., 2020) and *SLC38A10* encodes another member of the SNAT family which is also involved in regulating the glutamate and glutamine cycle in the brain, similarly to *SLC38A5* (Sundberg et al., 2008; Ayka and Şehirli, 2020).

To identify gRNAs exclusively depleted under hypoxia, a Venn diagram was generated using the top depleted gRNA for each gene. To focus on hypoxia-specific effects, we restricted this analysis to gRNAs depleted in the hypoxia vs day 0 comparison but not in the normoxia vs day 0 comparison, aiming to exclude general time-dependent depletion unrelated to hypoxia. However, we recognise that this filtering approach may exclude relevant hits if gRNAs are strongly depleted under hypoxia vs normoxia but also show weaker depletion under normoxia vs day 0. To address this, we have presented both filtered and unfiltered analyses for transparency. gRNAs were considered depleted based on a negative log_2FC and a p-value less than 0.05. Applying an FDR threshold yielded no gRNAs that were uniquely depleted under hypoxia. Therefore, unadjusted p-values were used to identify potentially relevant hits. The hit genes identified had their gRNA depleted in the hypoxia against normoxia comparison but not depleted in the normoxia against the day 0 comparison. From the MDA-MB-231, 64 hits were identified (Figure 3.12A). These genes were then ranked based on their log2FC. gRNAs targeting *SCN5A*, *SLC10A5*, *SLC38A5* and *SLC34A2* were identified as depleted under hypoxic conditions exclusively (Figure 3.12B). *SLC34A2* encoding the sodium-dependent phosphate transport protein 2B, NaPi-2b (Feild et al., 1999; Xu et al., 1999; Corut et al., 2006)

To further investigate changes in gRNA abundance between hypoxic and normoxic conditions, a ninesquare model was carried out by the Data Science team at the University of York (Bioscience Technology Facility). The ninesquare model categorised genes based on their relative depletion or enrichment across each condition and incorporated all five gRNAs per gene (Figure 3.13). No significant hits were identified however *SLC9A10, SLC34A2* and *GNG5* showed gRNA depletion under hypoxia. *SLC34A2* was exclusively depleted under hypoxia (Figure 3.12B). *SLC9A10* encodes for NHE10 which is involved in sperm motility (Wang et al., 2003) while *GNG5* was included as an essential gene for MDA-MB-468 cells.

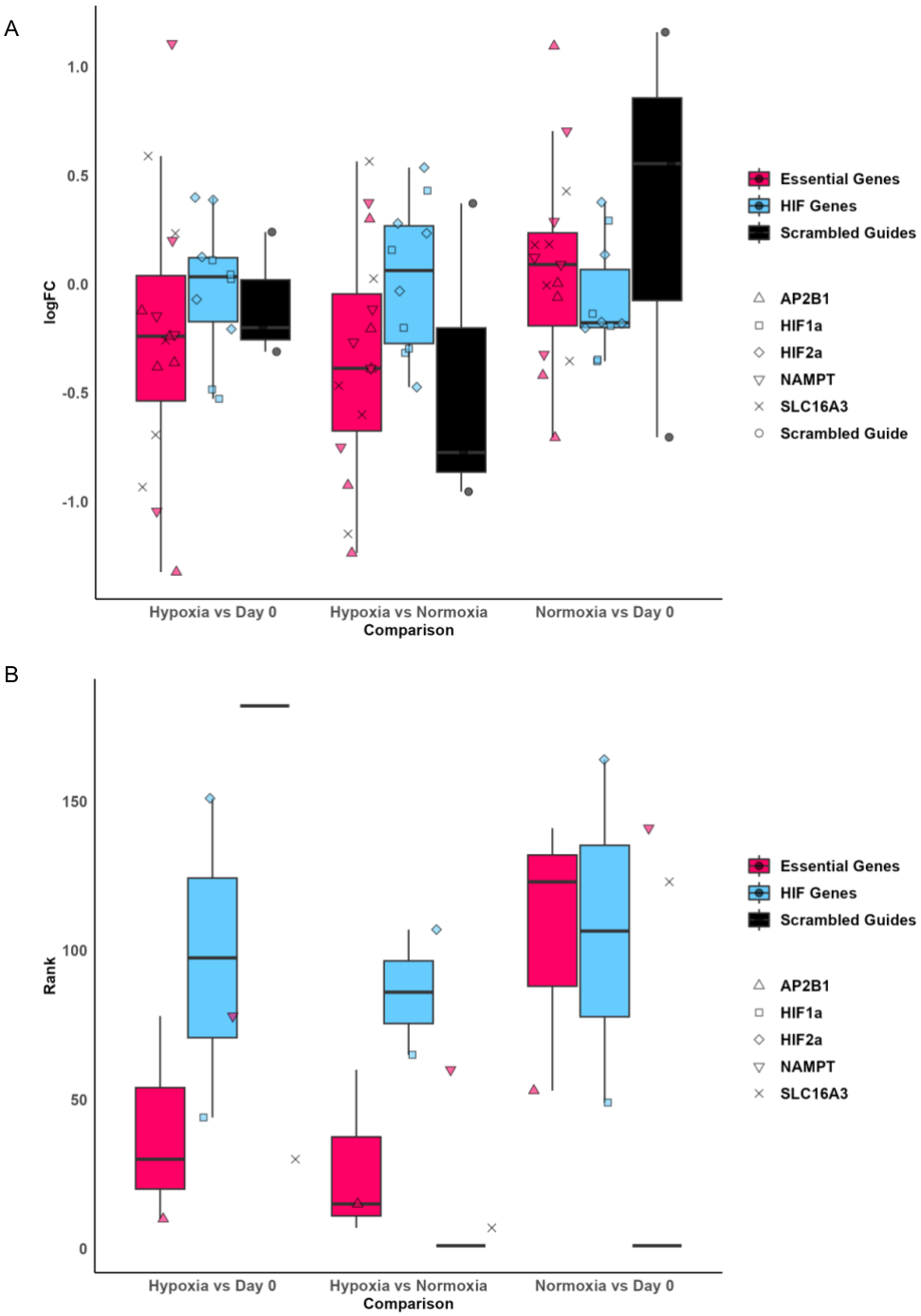


Figure 3.9. Control gRNA depletion and enrichment in MDA-MB-231.

(A) Log2 fold change (logFC) of control gRNAs across each comparison. Each data point represents pooled data from two replicates per comparison. (B) Rank of scores of each gene, mean of 5 gRNAs, for each comparison. Each bar represents pooled data from two replicates per comparison. Negative log2 fold change values represent depletion.

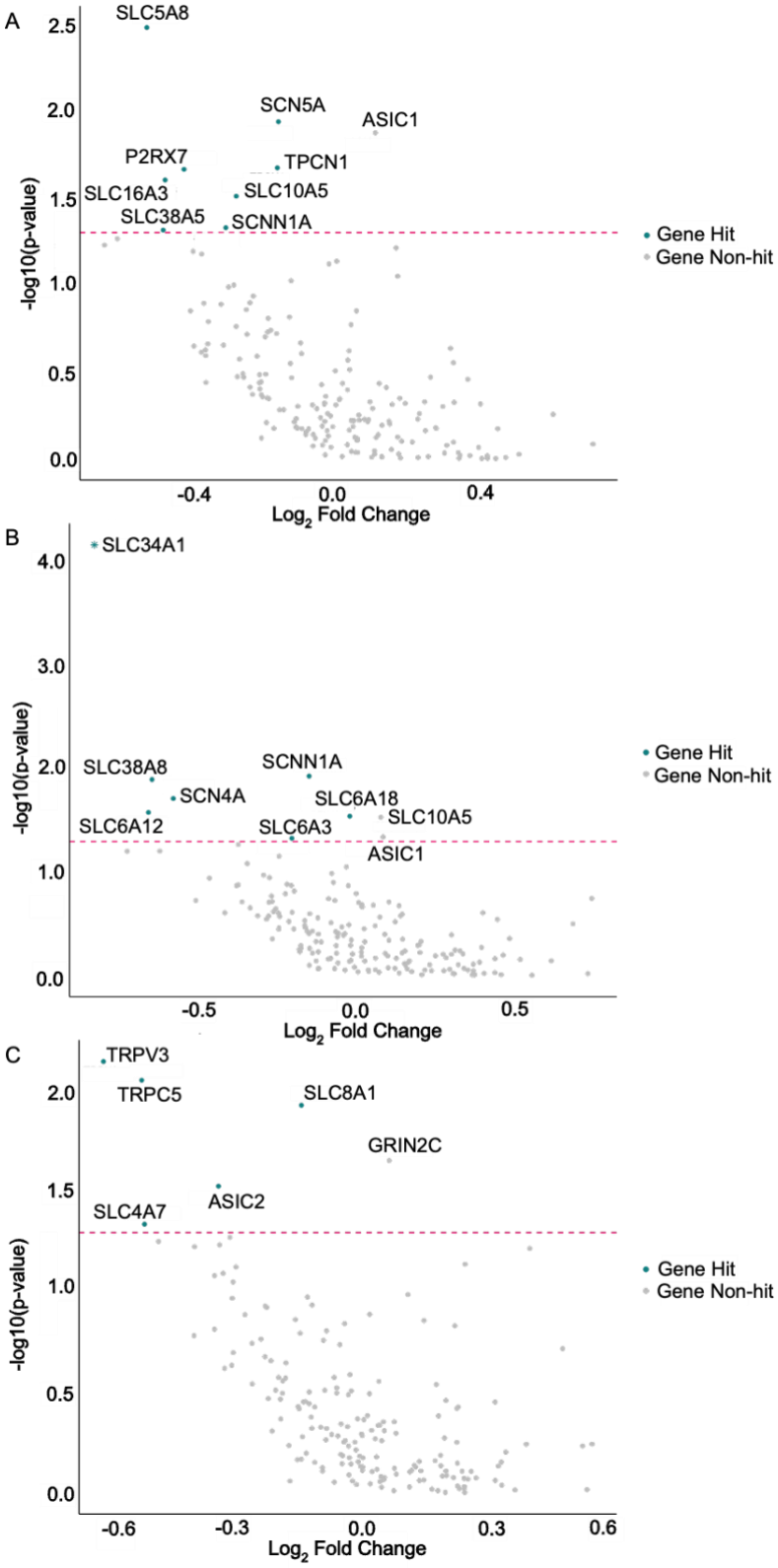


Figure 3.10. CRSIPR screen results in MDA-MB-231 considering all gRNAs.

Volcano plots show log2 fold change against -log10(p-value) for each gene (mean of 5 gRNAs). (A) Hypoxia vs normoxia, (B) hypoxia vs day 0 and (C) normoxia vs day 0 comparisons shown separately. The dashed red line indicates the significance threshold ($p < 0.05$). Genes with a significant false discovery rate (FDR < 0.05) are shown by stars. Scrambled gRNAs not shown. Negative log2 fold change values represent depletion. N = 2 replicates per comparison.

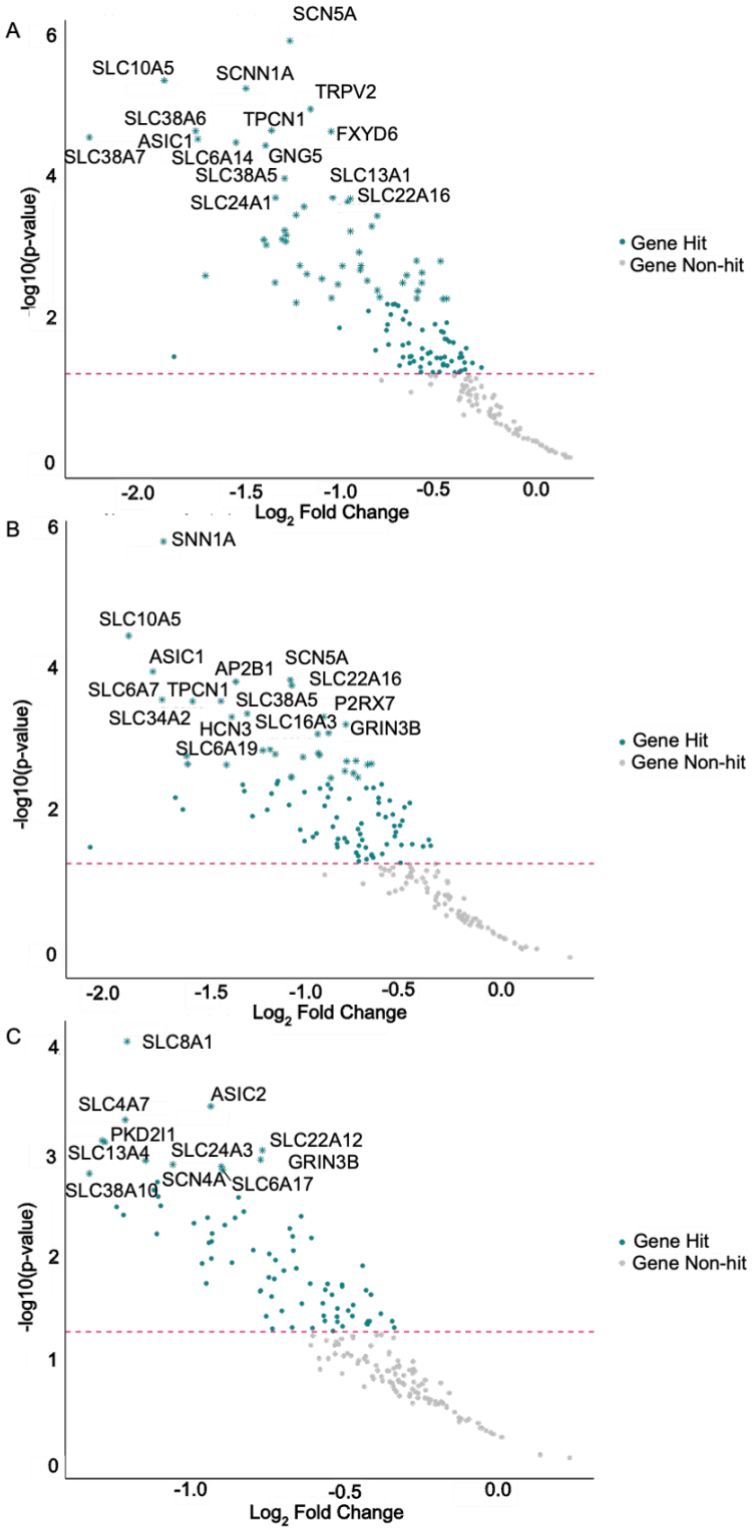


Figure 3.11. CRSIPR screen results in MDA-MB-231 using top depleted gRNA.

Volcano plots of the log2 fold against the -log10(p-value) for the top depleted gRNA for each gene. (A) Hypoxia vs normoxia, (B) hypoxia vs day 0 and (C) normoxia vs day 0 comparisons are shown separately. The dashed red line indicates the significance threshold ($p < 0.05$). Genes with a significant false discovery rate (FDR < 0.05) are shown by stars. Scrambled gRNAs not shown. Negative log2 fold change values represent depletion. N = 2 replicates per comparison.

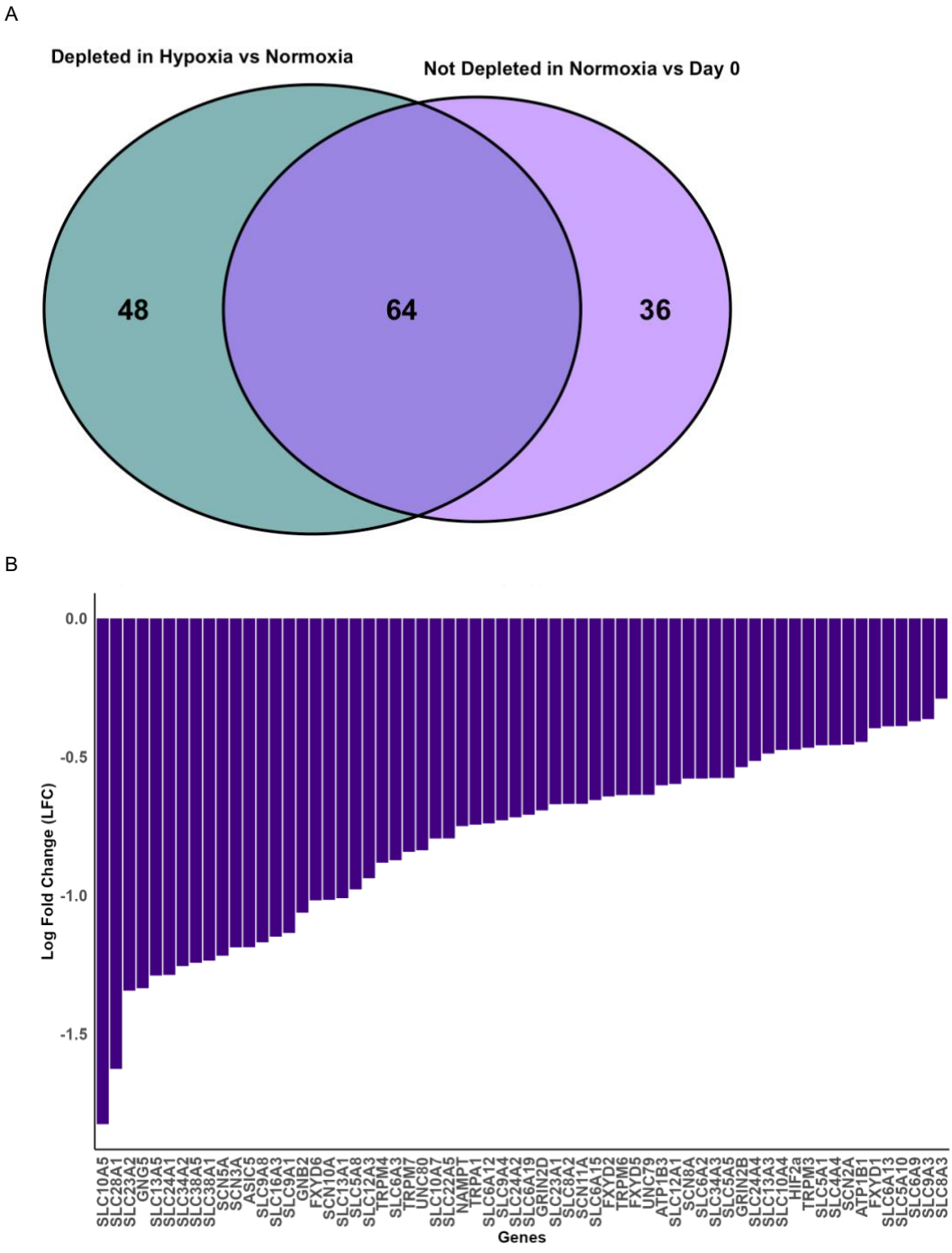


Figure 3.12. Genes selectively depleted under hypoxia in MDA-MB-231.

(A) Top depleted gRNA per gene identified from CRISPRi screen. Shown are 112 gRNAs significantly depleted in hypoxia compared to normoxia ($log_2FC < 0$, $p < 0.05$), and 100 gRNAs not depleted in normoxia compared to day 0 sample ($log_2FC \geq 0$). Of these, 64 gRNAs fall within the overlapping region of the two comparison sets. (B) The 64 identified genes from (A) shown from most to least depleted based on the log_2 fold change of their top depleted gRNA. Negative log_2FC values indicate gRNA depletion. N = 2.

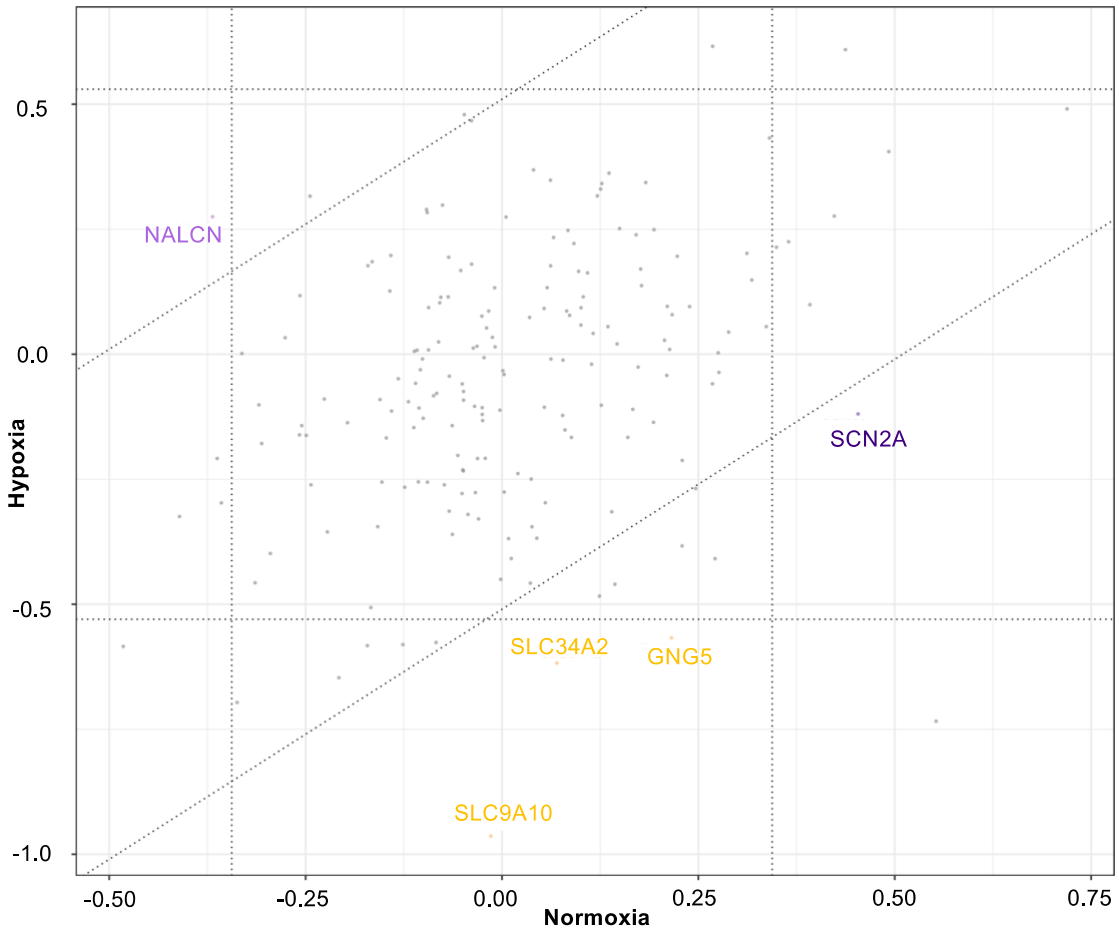


Figure 3.13. Comparison of gRNA depletion between hypoxia and normoxia in MDA-MB-231 cells.

Normoxia and hypoxia samples were independently analysed using the nf-core CRISPRseq v2.3.0 pipeline, with Day 0 samples serving as the baseline to control for initial gRNA abundance. The comparison between hypoxia and normoxia was visualized using the MAGeCKFlute ScatterView tool, based on MLE results. Genes were categorised using a ninesquare model to show their relative enrichment or depletion between conditions. Data are shown as $\log_2$ fold change for gene, based on five gRNAs per gene. Ninesquare plot generated by Data Science, Bioscience Technology Facility, University of York. Yellow indicates genes depleted in hypoxia but unaffected in normoxia; pink indicates genes depleted in normoxia but unaffected in hypoxia; purple indicates genes enriched in normoxia but unaffected in hypoxia. N = 2 replicates per condition.

3.7 Depleted gRNAs under hypoxia in MDA-MB-468

We next investigated a second TNBC cell line, MDA-MB-468. The initial three-way comparison between hypoxia, normoxia and day 0 samples in MDA-MB-468 cells found no significantly depleted gRNAs under hypoxic conditions compared to under normoxia, using FDR was used to determine significance (Figure 3.14A). There were also no significantly depleted gRNAs in the hypoxia against day0 and normoxia against day0 comparisons (Figure 3.14B,C)

In the MDA-MB-468 cell line, negative control gRNAs were again unexpectedly depleted or enriched in various comparisons (Figure 3.15A). Essential gene gRNAs were also not consistently depleted under hypoxia or normoxia compared to day 0, both when considered individually or combined (Figure 3.15). *HIF1A* and *HIF2A* gRNAs were not depleted under hypoxia either (Figure 3.15). Again, the surprising behaviour of the control gRNAs suggests caution in the interpretation of the screen results.

Again, since there were no significantly depleted gRNAs when combined, the $\log_2$ fold change and -log10(p-value) of the most depleted gRNA for each gene were plotted (Figure 3.16). However, even when just considering the top-depleted gRNA, no genes were identified as hits in the hypoxia against normoxia comparison (Figure 3.16A). Significantly depleted gRNAs in the hypoxia against day0 comparison include, *SCN5A,* which was identified in MDA-MB-231 cells under hypoxia both when compared with normoxia and day0, and *SLC34A1* which was also identified in MDA-MB-231 cells under hypoxia compared to day0 (Figure 3.16B). Under normoxia against day0 in MDA-MB-468, there was gRNA depletion for *SLC13A5* which encodes for a sodium-coupled citrate transporter (NaCT), (Pajor, 2014).

A Venn diagram was generated to identify 11 genes with gRNAs exclusively depleted under hypoxia (Figure 3.17A). These genes were then ranked based on their $\log_2$FC. Notably, *GRIN3A, SLC22A12* and *SLC34A3* were identified as depleted under hypoxic conditions exclusively (Figure 3.17B). These genes were identified with gRNA depletion under hypoxia against normoxia in MDA-MB-468 cells by the initial three-way comparison ($P < 0.05$; Figure 3.14A). *GRIN3A* encodes a subunit of the NMDA receptor (Sucher et al., 1995; Eriksson et al., 2002). *SLC22A12* encodes for URAT1, a urate-anion transporter (Enomoto et al., 2002). *SLC34A3* encodes for a Na^+-phosphate cotransporter NaP_i-IIc (Segawa et al., 2002). The only gene identified as depleted under hypoxia but not normoxia in both cell lines was

FXYD5, a regulatory subunit of the Na^+/K^+-ATPase (Garty and Karlish, 2006) (Figures 3.12B,3.17B).

The changes in gRNA abundance between hypoxic and normoxic conditions were further investigated in the MDA-MB-468 cell line using the ninesquare model carried out by the Data Science team at the University of York (Bioscience Technology Facility) (Figure 3.18). Notably, gRNAs targeting *GRIN3A* and *SLC6A7* were depleted under hypoxia but unaffected under normoxia (Figure 3.18). *SLC6A7* encodes a neurotransmitter L-proline transporter and is a member of the GABA neurotransmitter gene family. In the MDA-MB-468 cell line, there was no significant gRNA depletion under hypoxia compared to normoxia.

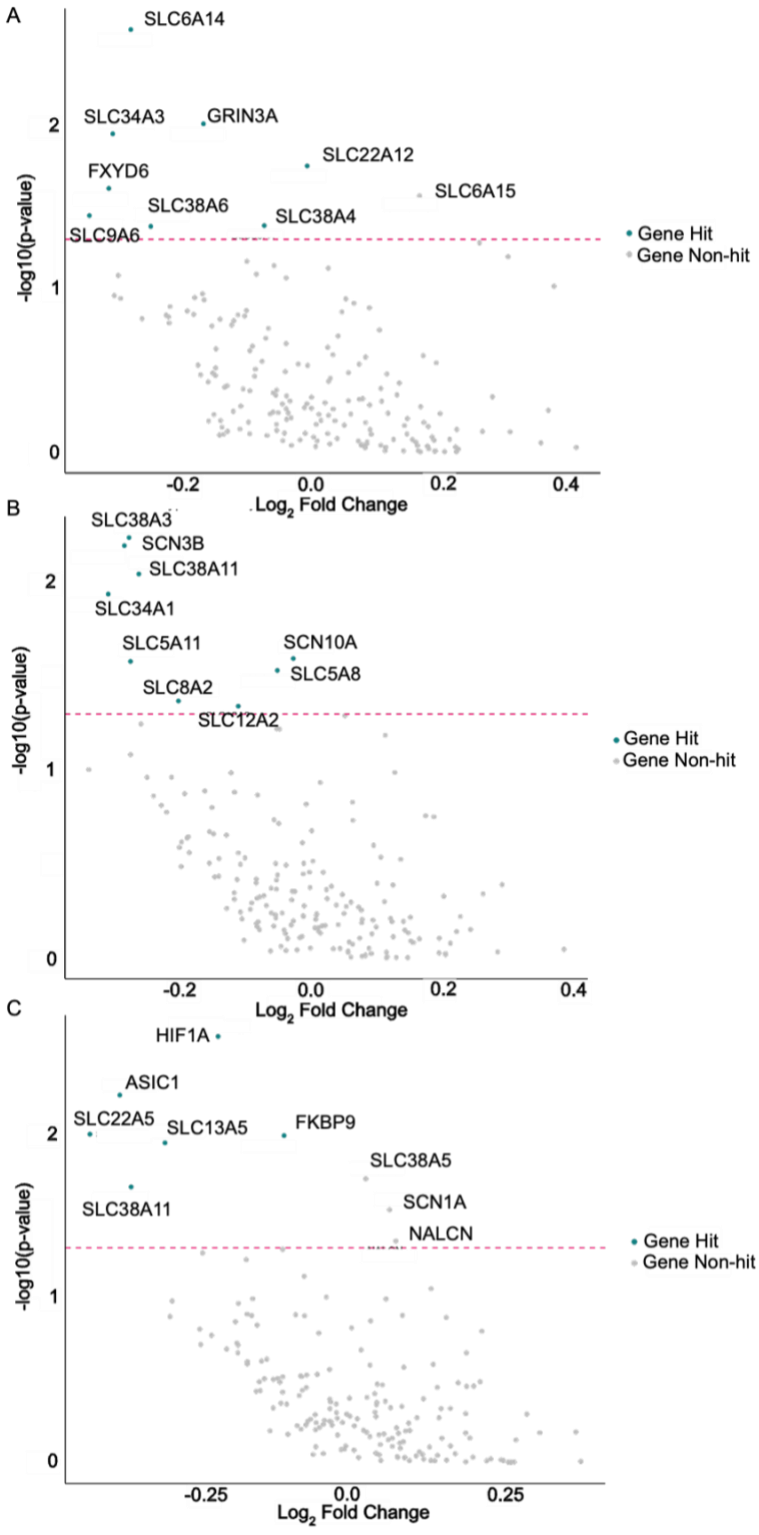


Figure 3.14. CRSIPR screen results in MDA-MB-468 considering all gRNAs.

Volcano plots show log2 fold change against -log10(p-value) for each gene (mean of 5 gRNAs). (A) Hypoxia vs normoxia, (B) hypoxia vs day 0 and (C) normoxia vs day 0 comparisons shown separately. The dashed red line indicates the significance threshold ($p < 0.05$). Genes with a significant false discovery rate (FDR < 0.05) are shown by stars. Scrambled gRNAs not shown. Negative log2 fold change values represent depletion. N = 2 replicates per comparison.

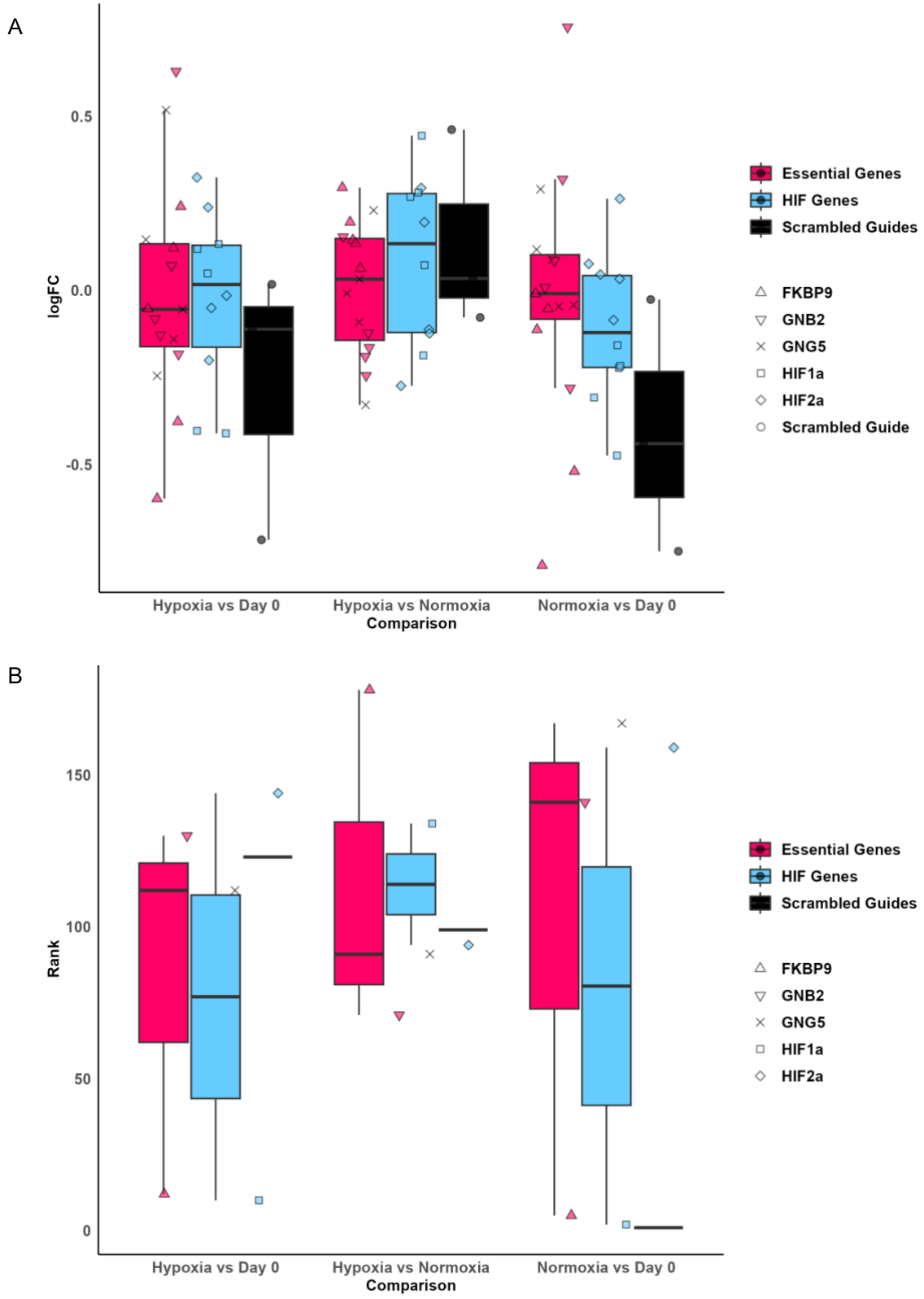


Figure 3.15. Control gRNA depletion and enrichment in MDA-MB-468.

(A) Log2 fold change (logFC) of control gRNAs across each comparison. Each data point represents pooled data from two replicates per comparison (B) Rank of scores of each gene, mean of 5 gRNAs, for each comparison. Each bar represents pooled data from two replicates per comparison Negative log2 fold change values represent depletion.

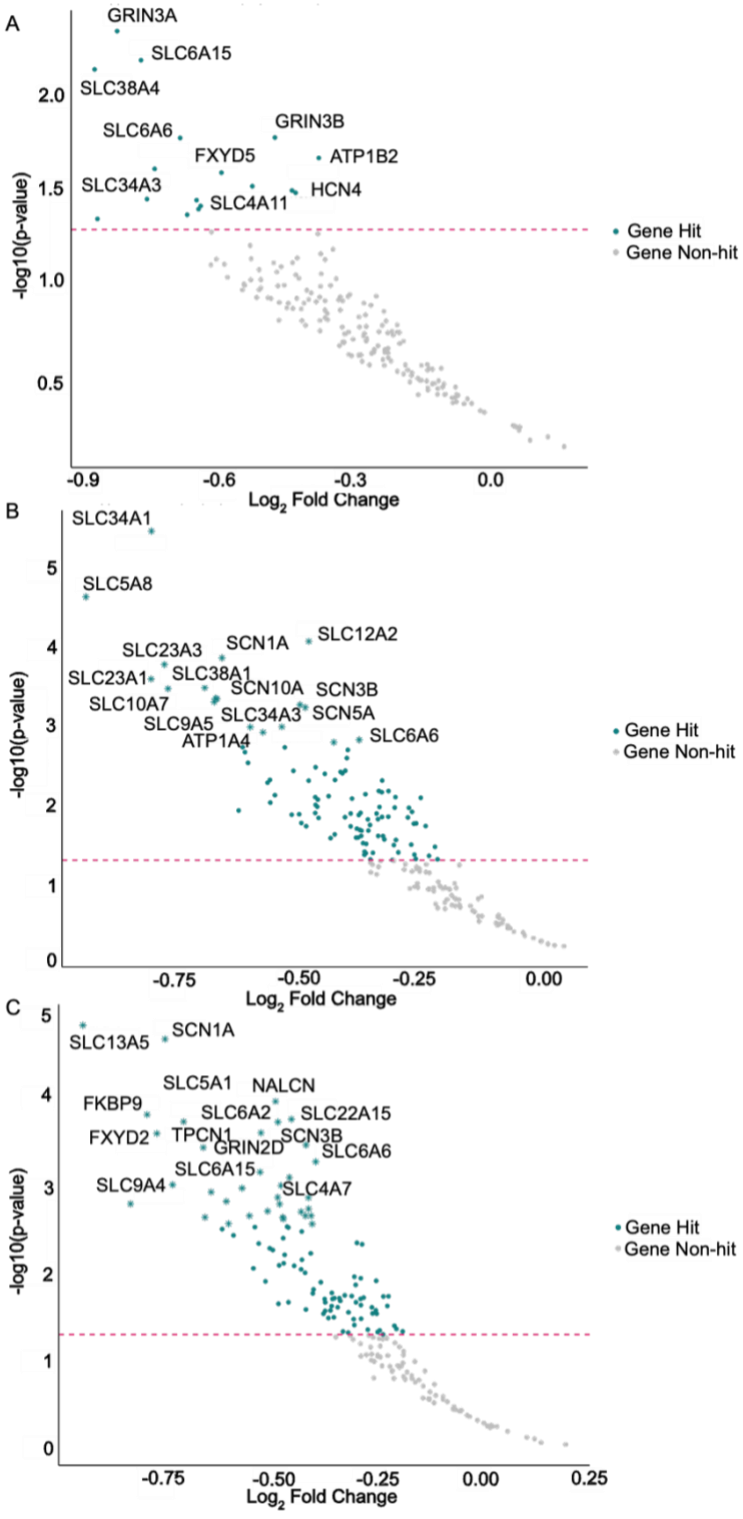


Figure 3.16. CRSIPR screen results in MDA-MB-468 using top depleted gRNA.

Volcano plots of the log2 fold against the -log10(p-value) for the top depleted gRNA for each gene. (A) Hypoxia vs normoxia, (B) hypoxia vs day 0 and (C) normoxia vs day 0 comparisons are shown separately. The dashed red line indicates the significance threshold ($p < 0.05$). Genes with a significant false discovery rate (FDR < 0.05) are shown by stars. Scrambled gRNAs not shown. Negative log2 fold change values represent depletion. N = 2 replicates per comparison.

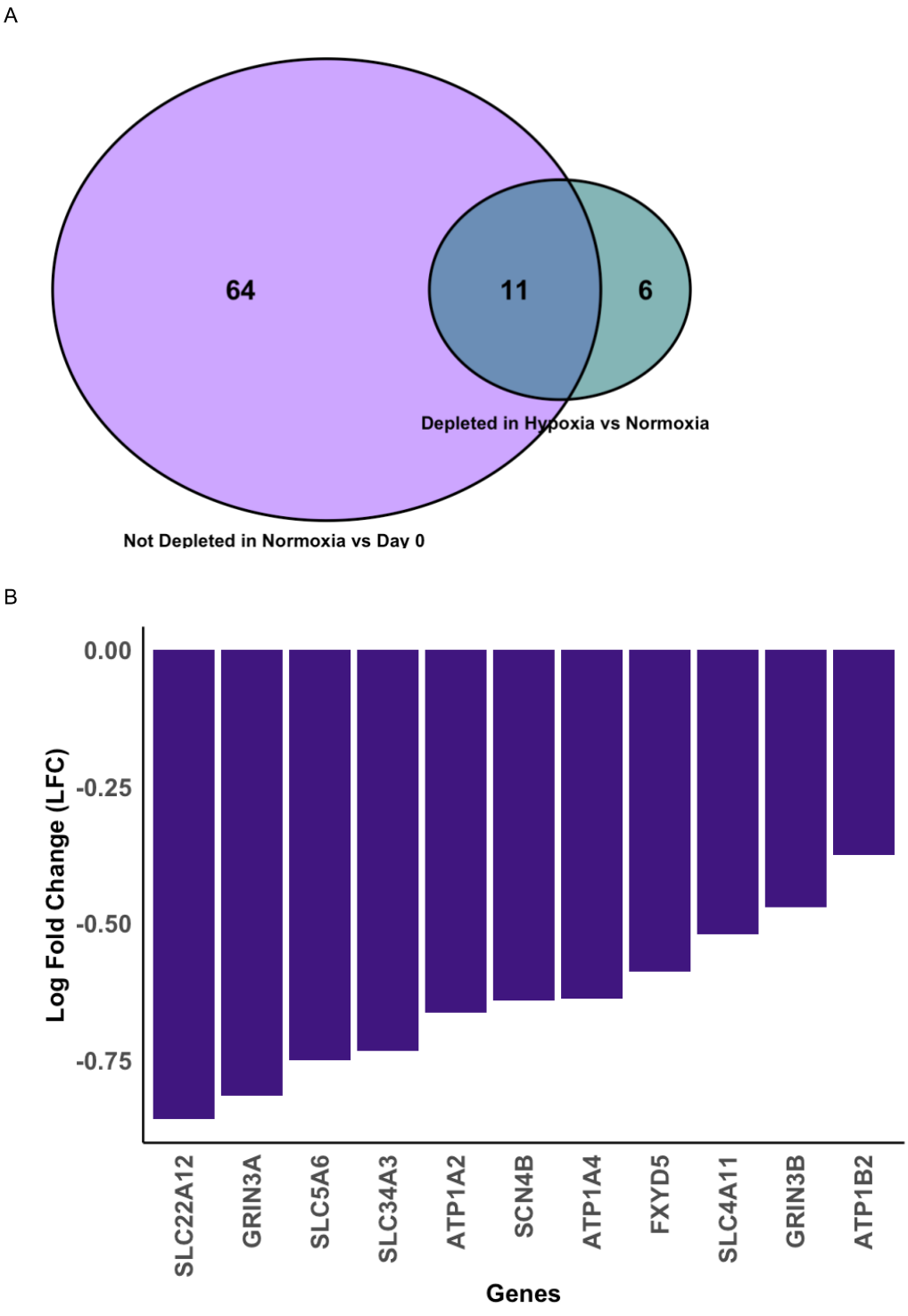


Figure 3.17. Genes selectively depleted under hypoxia in MDA-MB-468.

(A) Top depleted gRNA per gene identified from CRISPRi screen. Shown are 17 gRNAs significantly depleted in hypoxia compared to normoxia ($log_2FC < 0$, $p < 0.05$), and 75 gRNAs not depleted in normoxia compared to day 0 sample ($log_2FC \geq 0$). Of these, 11 gRNAs fall within the overlapping region of the two comparison sets. (B) The 11 identified genes from (A) shown from most to least depleted based on the log_2 fold change of their top depleted gRNA. Negative log_2FC values indicate gRNA depletion. N = 2.

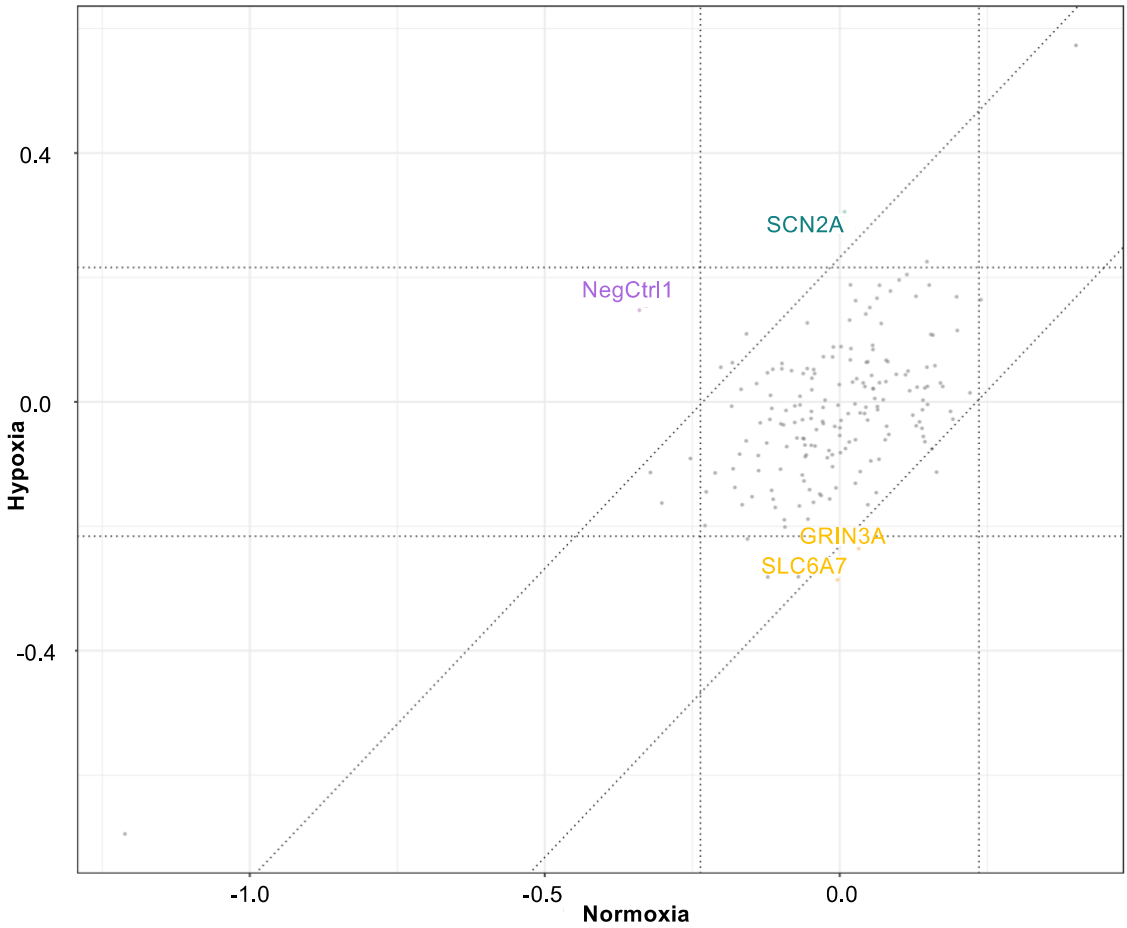


Figure 3.18. Comparison of gRNA depletion between hypoxia and normoxia in MDA-MB-468 cells.

Normoxia and hypoxia samples were independently analysed using the nf-core CRISPRseq v2.3.0 pipeline, with Day 0 samples serving as the baseline to control for initial gRNA abundance. The comparison between hypoxia and normoxia was visualized using the MAGeCKFlute ScatterView tool, based on MLE results. Genes were categorised using a ninesquare model to show their relative enrichment or depletion between conditions. Data are shown as log2 fold change for gene, based on five gRNAs per gene. Ninesquare plot generated by Data Science, Bioscience Technology Facility, University of York. Yellow indicates genes depleted in hypoxia but unaffected in normoxia; pink indicates genes depleted in normoxia but unaffected in hypoxia; purple indicates genes enriched in normoxia but unaffected in hypoxia. N = 2 replicates per condition.

3.8 Clinical relevance

To assess the clinical relevance of genes identified with significantly depleted gRNAs under hypoxia in either MDA-MB-231 or MDA-MB-468 cell lines, we analysed overall survival in TNBC patients using publicly available TCGA, GDC data (CBioPortal). Kaplan-Meier survival curves were generated for each gene, stratifying patients by high versus low mRNA expression levels based on Z-scores (Figure 3.19). The genes examined included *SCN5A*, *SLC10A5*, *SLC38A5*, *SLC34A2*, *GRIN3A*, *SLC22A12*, and *SLC34A3*. None of these genes showed a statistically significant link with overall survival (all $p > 0.05$; log-rank test; Figure 3.19), suggesting that while they may influence cancer cell proliferation under hypoxic conditions in vitro, their expression levels do not seem to predict patient outcomes in TNBC.

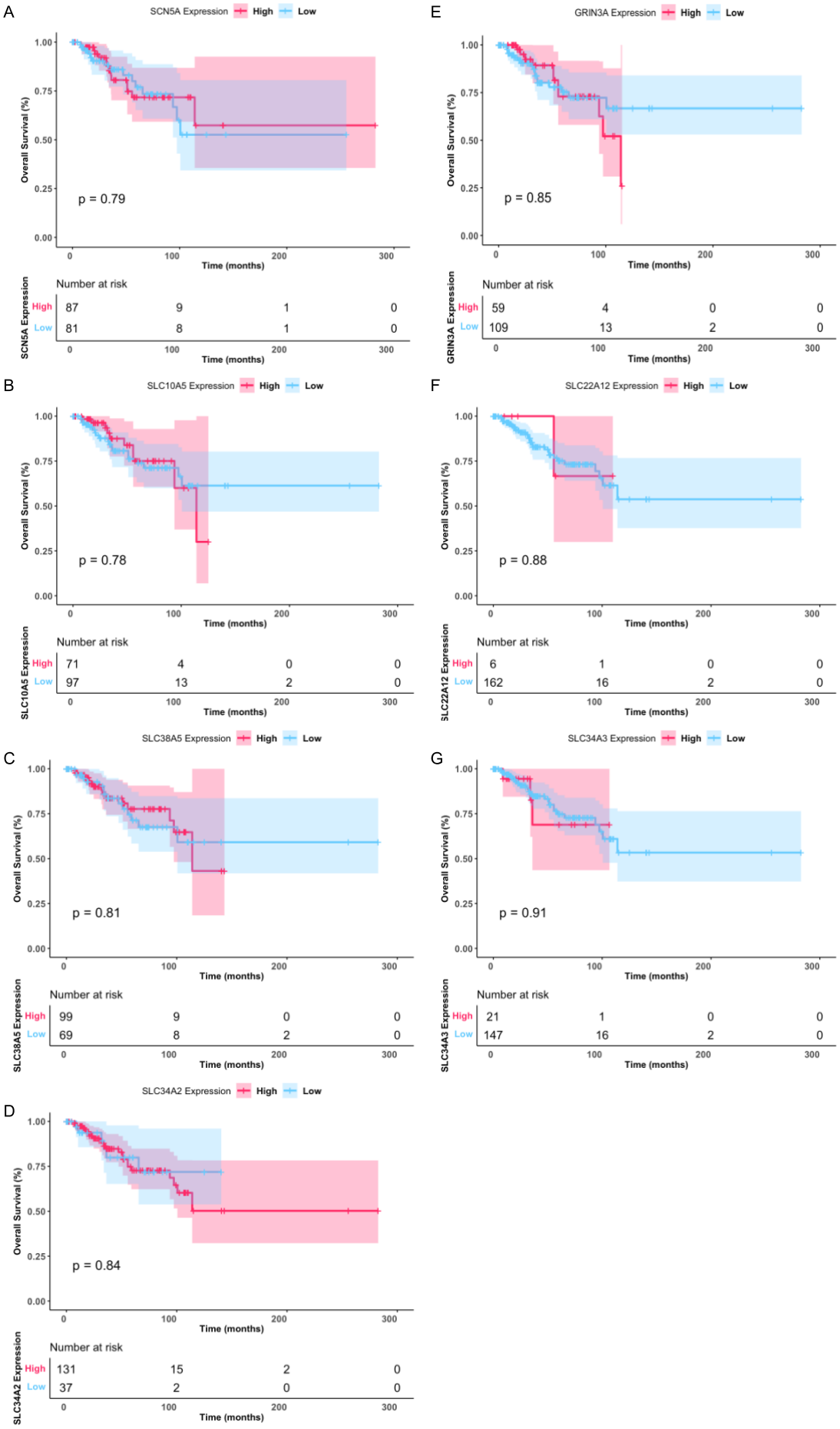

A
SCN5A Expression High Low
Overall Survival (%)
p = 0.79
Time (months)
Number at risk
SCN5A Expression
High 87 9 1 0
Low 81 8 1 0
B
SLC10A5 Expression High Low
p = 0.78
SLC10A5 Expression
High 71 4 0 0
Low 97 13 2 0
C
SLC38A5 Expression High Low
p = 0.81
SLC38A5 Expression
High 99 9 0 0
Low 69 8 2 0
D
SLC34A2 Expression High Low
p = 0.84
SLC34A2 Expression
High 131 15 2 0
Low 37 2 0 0
E
GRIN3A Expression High Low
p = 0.85
GRIN3A Expression
High 59 4 0 0
Low 109 13 2 0
F
SLC22A12 Expression High Low
p = 0.88
SLC22A12 Expression
High 6 1 0 0
Low 162 16 2 0
G
SLC34A3 Expression High Low
p = 0.91
SLC34A3 Expression
High 21 1 0 0
Low 147 16 2 0

Figure 3.19. Kaplan-Meier survival curves.

Kaplan-Meier survival curves stratified by mRNA expression levels of (A) *SCN5A*, (B) *SLC10A5*, (C) *SLC38A5*, (D) *SLC34A2*, (E) *GRIN3A*, (F) *SLC22A12*, and (G) *SLC34A3*. Plots show the proportion of patients surviving (Overall Survival, %) over time (months), comparing high (red) and low (blue) gene expression groups in a population of 168 patients. Expression groups were defined based on Z-scores, with positive Z-scores classified as high expression and negative Z-scores as low expression. Statistical significance between survival curves was evaluated using the log-rank test. Patient data were obtained from the TCGA Invasive Breast Carcinoma cohort (TCGA, GDC), and survival analysis was performed using ISB-CGC BigQuery tables (accessed July 2024). Dataset was filtered to include only TNBC cases using the Burnstein classification (Burstein et al., 2015; Kalecky et al., 2020)

3.9 Effect of propafenone on transient Na^+ current

SCN5A, the gene encoding $Na_v1.5$, emerged as a tentative hit in the CRISPRi screen performed in MDA-MB-231 cells. Although *SCN5A* was not statistically significant when considering all gRNAs, the top-deleted gRNA targeting *SCN5A* was significantly depleted, based on the FDR threshold, under hypoxia compared to normoxia (Figure 3.9A, 3.10A). $Na_v1.5$, expressed in the MDA-MB-231 cell line, promotes invasion, proliferation and migratory ability in breast cancer (Fraser et al., 2005; Brackenbury et al., 2007). Given its involvement in invasion, $Na_v1.5$ represents a promising therapeutic target. To explore this, the antiarrhythmic agent propafenone, previously untested in a cancer context, was selected for electrophysiological investigation to determine its effect on Na^+ current and its potential to inhibit $Na_v1.5$ in breast cancer cells.

The effect of propafenone on Na^+ current properties was evaluated using whole-cell patch clamp recording in the MDA-MB-231 breast cancer cell line. Initially we evaluated the effect of propafenone on the size of peak Na^+ current. Currents were elicited by depolarising the membrane potential from a holding potential of -120 mV to -10 mV. Application of propafenone at a concentration of 100 µM (Edrich et al., 2005; Seki et al., 1999) significantly inhibited the peak Na^+ current density from -7.812 ± 1.57 pA/pF to -0.9368 ± 0.24 pA/pF ($P < 0.05$; n = 6; ANOVA + Tukey test; Figures 3.20A,C). The inhibition of peak Na^+ current was reversible following washout of propafenone ($P < 0.05$; n = 6; ANOVA + Tukey test; Figure 3.20C)

Lower concentrations of propafenone (1, 3, 10, 30 µM) produced a similar, dose-dependent reduction of peak Na^+ current (Figures 3.21A; Table 3.1). Although only 30 and 100 µM elicited a significant reduction of peak current from -6.81 ± 0.88 pA/pF to -4.05 ± 0.89 pA/pF ($P < 0.05$) and -0.97 ± 0.30 pA/pF ($P < 0.001$) respectively (n = 7 – 13; LME; Table 3.1).

3.10 Effect of propafenone on persistent Na^+ current

We also evaluated the effect of propafenone on the persistent Na^+ current measured 20-25 ms following depolarisation from 120 mV to -10 mV. Treatment with 100 µM propafenone reversibly reduced persistent Na^+ current density from -0.7457 ± 0.21 pA/pF to -0.1728 ± 0.11 pA/pF ($P = 0.13$; n = 6; ANOVA + Tukey test; Figures 3.20B, D). A similar trend of

dose-dependent inhibition was observed at lower concentrations of propafenone (1, 3, 10, 30 μM) ($p < 0.001$; n = 6-13; LME; Figure 3.21B; Table 3.1).

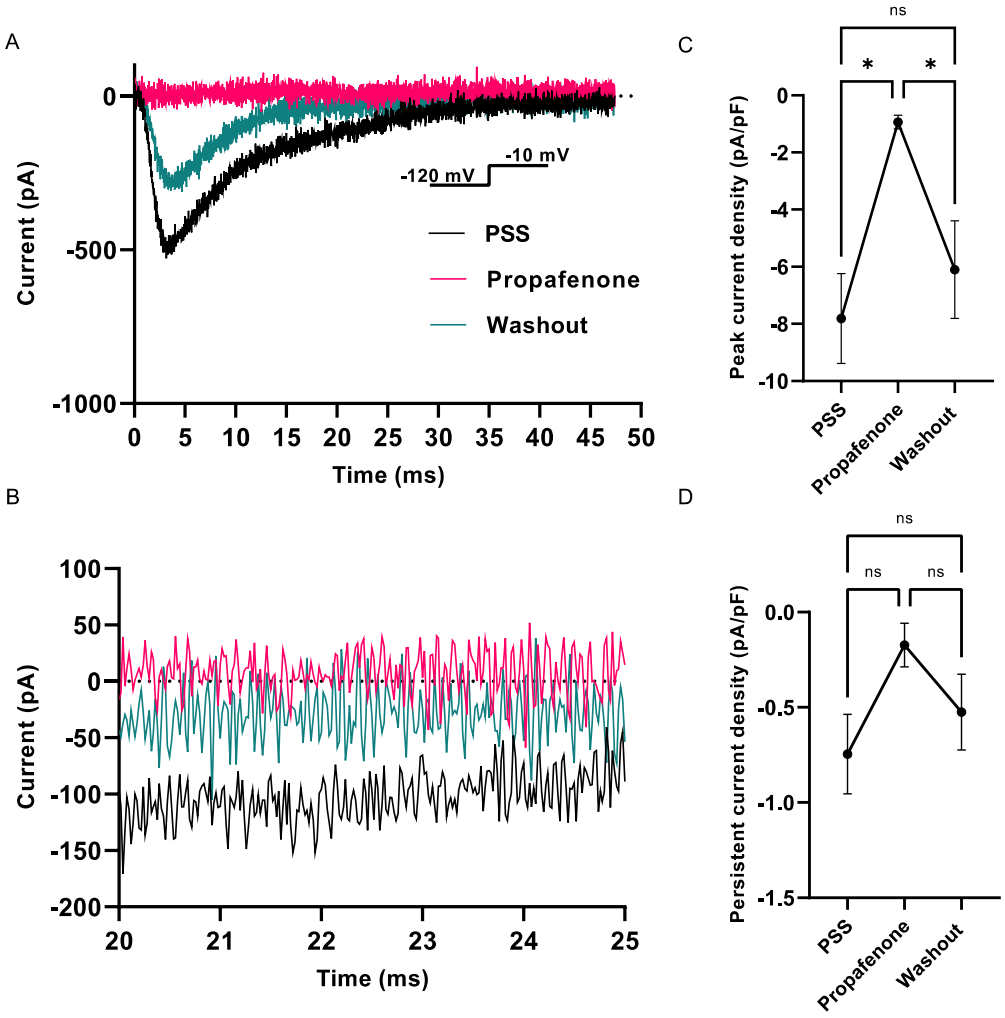


Figure 3.20. Effect of propafenone on Na^+ currents.

(A) Representative Na^+ currents in an MDA-MB-231 cell elicited by a depolarisation from -120 to -10 mV in physiological saline solution (PSS; black), propafenone (100 μM; pink) and after washout (green). (B) Representative persistent Na^+ currents, amplified from (A) between 20 and 25 ms, in an MDA-MB-231 cell elicited by a depolarisation from -120 to -10 mV. (C) Peak current density in MDA-MB-231 cells elicited by a depolarisation from -120 to -10 mV. (D) Persistent current density in MDA-MB-231 cells elicited by a depolarisation from -120 to -10 mV. Results are mean + SEM. *P ≤ 0.05; repeated measures one-way ANOVA with Tukey tests (n = 6). NS, not significant.

Table 3.1. Effect of propafenone on Na^+ current characteristics in MDA-MB-231 cells.

Parameter	*Control*	*1 uM*	*3 uM*	*10 uM*	*30 uM*	*100 uM*	*Overall Model Significance*	*N*
Peak current density at -10 mV (pA/pF)	-6.81 ± 0.88	-6.4 ± 1.24	-6.89 ± 0.84	-4.98 ± 1.11	-4.05 ± 0.89*	-0.97 ± 0.30***	F = 8.384, p < 0.001***	6 - 13
Persistent current density at -10 mV (pA/pF)	-1.17 ± 0.22	-0.63 ± 0.14*	-1.08 ± 0.27	-0.38 ± 0.09**	-0.59 ± 0.16*	-0.16 ± 0.06***	F = 5.472, p < 0.001***	6 - 13
Tp at -10 mV (ms)	6.09 ± 1.01	4.5 ± 0.4	5.58 ± 1.28	4.01 ± 0.27	5.38 ± 1.32	N/A	F = 0.6204, p = 0.6511	6 - 13
τf at -10 mV (ms)	4.27 ± 0.91	3.58 ± 0.45	3.78 ± 0.98	2.86 ± 0.23	3.28 ± 0.94	N/A	F = 0.3931, p = 0.8121	6 - 13
τs at -10 mV (ms)	21.58 ± 4.0	20.26 ± 4.27	15.17 ± 3.37	17.11 ± 4.07	17.13 ± 5.11	N/A	F = 0.3153, p = 0.8658	6 - 13

Electrophysiological parameters measured at –10 mV across treatment concentrations. Propafenone (1, 3, 10, 30, 100 µM); T_p, time to peak current; τ_f, fast time constant of inactivation; τ_s, slow time constant of inactivation. The holding potential was -120 mV. Results are mean ± SEM. Statistical comparisons were made by a one-way linear mixed effects model (LME) with the overall model F-test and p-value reported in the “Overall Model Significance” column (n = 6–13). *P ≤ 0.05; **P ≤ 0.01; ***P ≤ 0.001.

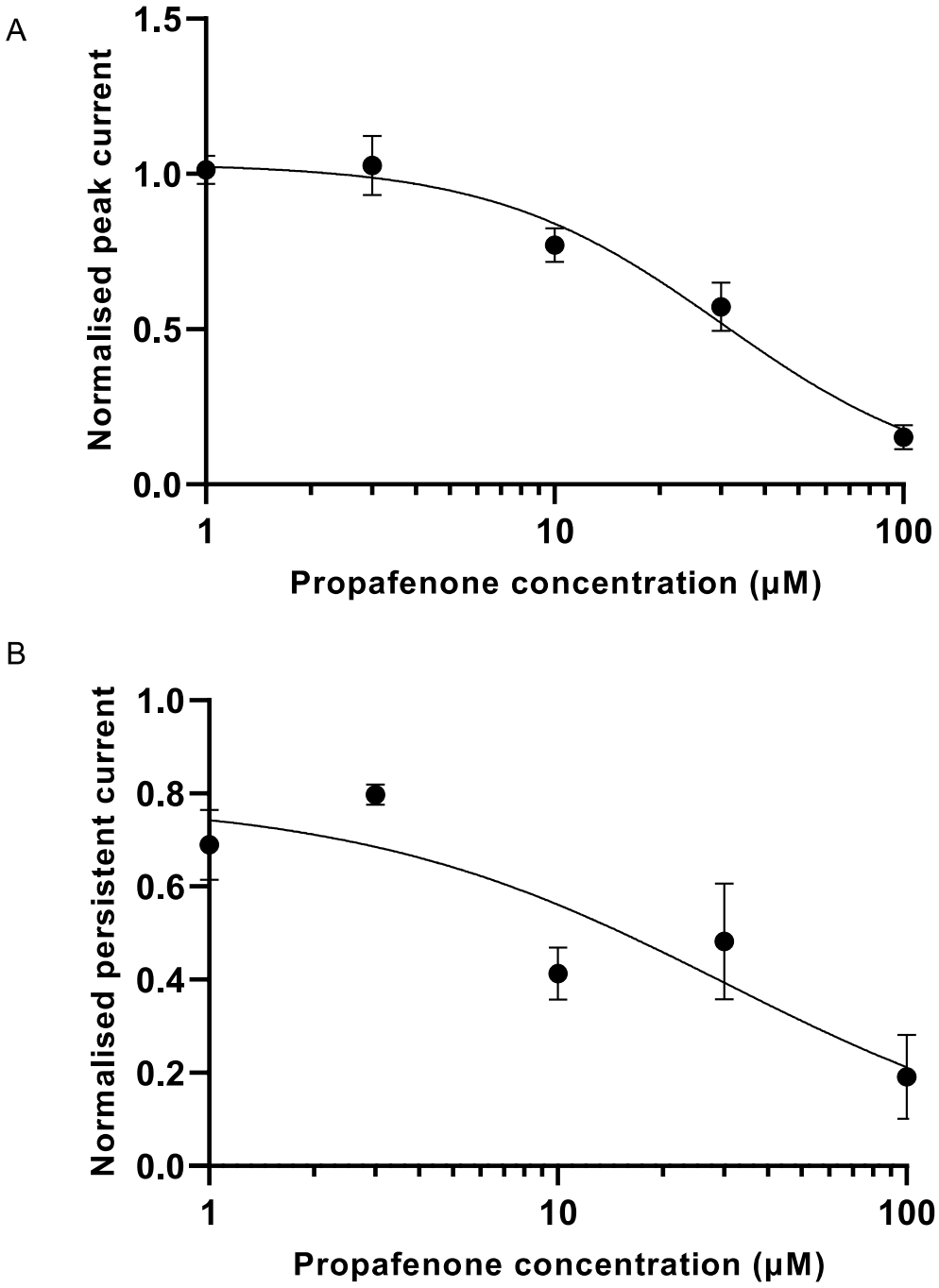


Figure 3.21. Dose-dependent inhibition of Na^+ currents by treatment with propafenone (1, 3, 10, 30, 100 μM).

(A) Normalised peak Na^+ current inhibition plotted against drug concentration. (B) Normalised persistent N Na^+ current inhibition plotted against drug concentration. Data were fitted with a Hill equation using non-linear regression. Data are presented as mean ± SEM (n = 6-11).

3.11 Effect of propafenone on voltage-current relationship

To investigate the effect of propafenone on the voltage dependence of Na^+ current activation, current-voltage curves were generated before and after application of propafenone (100 μM). Propafenone reduced Na^+ current across the voltage range tested, consistent with inhibition of channel activation (Figure 3.22). There was no evidence of any voltage dependent effect as current was ablated across the entire range of voltages tested.

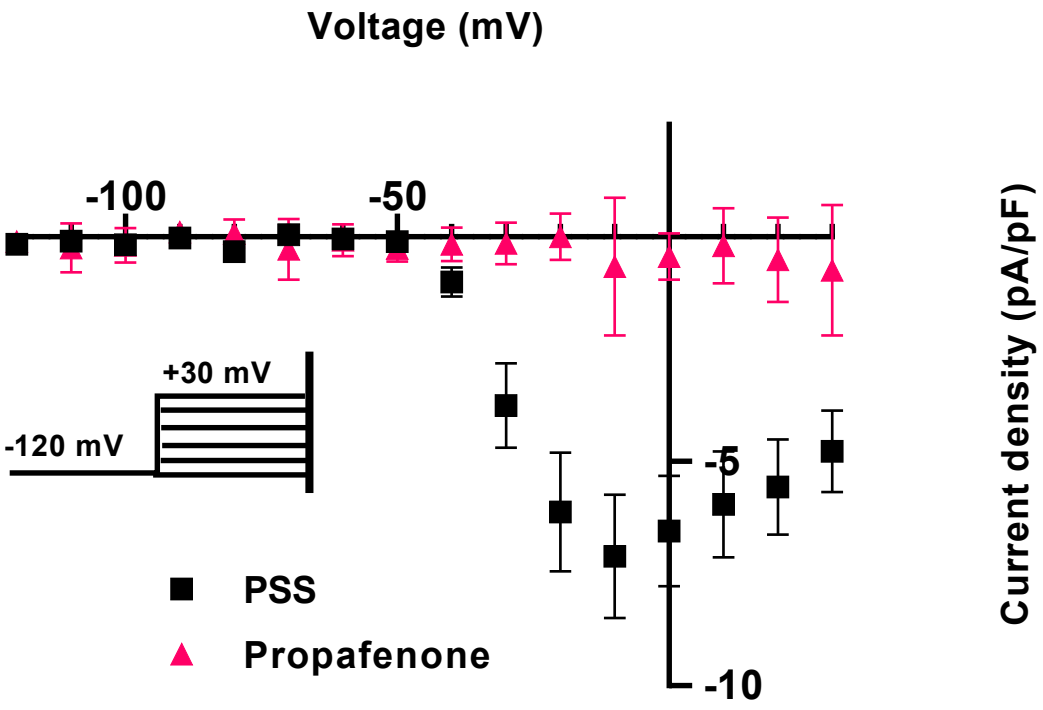


Figure 3.22. Effect of propafenone on the current-voltage relationship.

Current-voltage (I–V) plots of Na^+ currents in MDA-MB-231 cells in physiological saline solution (Control; black squares) and in propafenone (100 μM; pink triangles). Currents were elicited using 10 mV depolarising steps from -120 to +30 mV for 30 ms. Results are mean ± SEM (n = 8).

3.12 Effect of propafenone on activation and inactivation kinetics

Propafenone had no significant effect on the time to peak current (T_p), following depolarisation from -120 to -10 mV, across all concentrations tested (P = 0.6511; n = 6-13; LME; Table 3.1). Inactivation kinetics were analysed by fitting the current decay phase of the Na^+ current, following depolarisation from -120 to -10 mV, to a double exponential function to derive fast (τ_f) and slow (τ_s) time constants of inactivation. Propafenone did not significantly affect either τ_f or τ_s (P = 0.8121 and P = 0.8658, respectively; n = 6-13; LME; Table 3.1). In summary, propafenone does not affect VGSC kinetics in MDA-MB-231 cells.

4. Discussion

4.1 Summary of main findings

This study investigated the role of Na^+ transporters in TNBC cell proliferation under hypoxia using a custom CRISPRi screen. We screened 181 Na^+ transport-related genes in MDA-MB-231 and MDA-MB-468 cells which we established to stably express dCas9-KRAB through lentiviral transduction. These cells were cultured under normoxic or hypoxic conditions for seven days. We observed hypoxia-specific depletion of gRNAs targeting *SCN5A*, *SLC10A5*, *SLC38A5*, and *SLC34A2* in MDA-MB-231 cells, and *GRIN3A*, *SLC22A12* and *SLC34A3* in MDA-MB-468 cells. *FXYD5* was depleted exclusively under hypoxia in both cell lines when considering only the top-depleted gRNA. However, technical limitations, such as low gRNA representation and inconsistent control depletion, raised concerns of the robustness of the screen. Pharmacological inhibition of Na^+ currents confirmed the blocking of VGSCs, particularly $Na_v1.5$, using propafenone in MDA-MB-231 cells.

4.2 Key CRISPRi screen findings

4.2.1 Identification of Na^+ transporters which contribute to MDA-MB-231 cell proliferation under hypoxia

Several Na^+ transporters were exclusively depleted under hypoxia in MDA-MB-231 cells. Among them, *SCN5A*, which encodes the VGSC $Na_v1.5$, was a promising candidate. The top-depleted gRNA targeting *SCN5A* was significantly and exclusively depleted under hypoxia based on the FDR threshold. Furthermore, when considering all gRNAs targeting *SCN5A*, there was depletion under hypoxia based on the p-value threshold. $Na_v1.5$ is upregulated in breast cancer and has been linked to breast cancer invasiveness and metastasis (Fraser et al., 2005; Brackenbury et al., 2007; Yang et al., 2012). $Na_v1.5$ upregulation also increases breast cancer metastasis *in vivo* (Nelson et al., 2015). Our

findings align with prior research that shows hypoxia promotes $Na_v1.5$ expression (Plant et al., 2020), suggesting that *SCN5A* may be involved in proliferation in hypoxic TNBC.

In addition to *SCN5A*, *SLC10A5* and *SLC38A5* were identified as hypoxia-specific hits. When considering all gRNAs targeting each gene, significant depletion was observed under hypoxia based on the unadjusted p-value. For both genes, the most strongly depleted gRNA also met the FDR significance threshold. *SLC10A5* encodes a Na^+-bile acid cotransporter (Fernandes et al., 2007), although its role in cancer remains unexplored. *SLC38A5* encodes for SNAT5, a Na^+-coupled neutral amino acid transporter, and is involved in regulating the glutamate and glutamine cycle in the brain, (Nakanishi et al., 2001; Nakanishi et al., 2001; Ayka and Şehirli, 2020). *SLC38A5* is upregulated in several cancers, such as hepatocellular carcinoma, to mediate the influx of glutamine, serine, glycine, and methionine into cancer cells and has been shown to be upregulated by hypoxia and MYC (Taurino et al., 2023; Zhang et al., 2022; Girardi et al., 2020; Bode et al., 2002; Tian et al., 2017).

While TNBC cells already rely heavily on glycolysis due to the Warburg effect, glutamine metabolism becomes increasingly important under hypoxia (Warburg,1956). Glutamine can feed the TCA cycle through reductive carboxylation, especially under hypoxia, where mitochondrial entry of pyruvate is reduced by PDK1 activation and increased lactate production (Metallo et al., 2012; Kim et al., 2006; Le et al., 2012; Fan et al., 2013). Fan et al. (2013) showed the essential role of glutamine in maintaining oxidative phosphorylation under both normoxic and hypoxic conditions. In 4T1, a Akt-driven mouse mammary tumour cell line, and ASPC1, a K-Ras-driven human pancreatic cancer cell line, glutamine removal reduced oxygen consumption more than glucose removal, especially in hypoxia, demonstrating an important role for glutamine when glycolysis is limited (Fan et al., 2013).

Hypoxia-induced upregulation of glutamine transporters including *SLC1A5*, the *SLC1A5* variant, and *SLC38A2* has been observed in cancer cells with *SLC38A2* upregulation in TNBC cell lines MDA-MB-231 and MDA-MB-468 (Yoo et al., 2020; Morotti et al., 2019). *SLC38A5* may be similarly upregulated in TNBC cells although direct evidence remains to be demonstrated. Furthermore, HIF-1α activation under hypoxia in tumour cells induces glutaminase (GLS) transcription (Thorén et al., 2017). The increased dependence of glutamine metabolism has been linked to *BRAF* mutations in melanoma cells, where increased glutaminase activity promotes proliferation (Baenke et al., 2016). Therefore, *SLC38A5* may support glutamine metabolism under hypoxia in TNBC, possibly by complementing other glutamine transporters and supporting the metabolic shift toward reductive carboxylation (Metallo et al., 2012; Fan et al., 2013).

Interestingly, *SLC38A5* expression is reduced by BET inhibitors such as JQ1 and OTX-015, which inhibit cancer cell proliferation and migration, highlighting a *SLC38A5* as a potential therapeutic target (Taurino et al., 2023). JQ1 and OTX-015 treatment in hepatocellular carcinoma cells was shown to downregulated *SLC38A5*, at the mRNA level, through inhibition of bromodomain-containing protein BRD4 (Choi et al., 2021; Taurino et al., 2023). There may be a regulatory link between BET proteins and *SLC38A5* expression, although broader transcriptomic effects of BET inhibitors may contribute. BET inhibitors affect a broad range of genes (Doroshow et al., 2017; Pervaiz et al., 2018). Thus, the reduction in *SLC38A5* may be an indirect or off-target effect rather than a direct mechanism of action. Although reduced *SLC38A5* expression may not be the primary mechanism of BET inhibitors, our finding suggests that *SLC38A5* contributes to cancer cell proliferation under hypoxia and could be a druggable target in hypoxic TNBC.

SLC34A2, a Na^+-dependent phosphate cotransporter NaPi-2b, also showed depletion under hypoxia (Feild et al., 1999; Xu et al., 1999; Corut et al., 2006; Sabbagh et al., 2009). Although *SLC34A2* depletion under hypoxia did not reach statistical significance, the top-depleted gRNA targeting *SLC34A2* was depleted in hypoxia and not depleted in normoxia. *SLC34A2* is a phosphate transporter known to be overexpressed at the mRNA level in breast (Chen et al., 2010), thyroid (Jarząb et al., 2005), prostate (Lacerda-Abreu et al., 2018), and ovarian cancers (Rangel et al., 2003). However, *SLC34A2* has yet to show clinical relevance in breast cancer, as expression levels do not correlate with tumour grade, hormone receptor status, metastasis status, or patient survival (Chen et al., 2010).

Furthermore, inorganic phosphate has been shown to promote tumour progression in mouse lung cancer models (Jin et al., 2009; Camalier et al., 2010; Bobko et al., 2017). Jin et al. (2009) demonstrated that dietary phosphate intake increased lung tumour mass in K-ras^{LA1} mice, a spontaneous lung cancer model (Johnson et al., 2001). High phosphate intake led to increased Akt phosphorylation on Ser473 residue, indicating altered Akt signaling, which promotes cell migration and metastiasis (Jin et al., 2009). However, its role is context dependent as Akt1 inhibits breast cancer migration and metastasis, while Akt2 has the opposite effect (Qiao et al., 2008; Tsai et al., 2022). Camalier et al. (2010) demonstrated that extracellular phosphate levels activated N-Ras, increasing ERK1/2 phosphorylation through MAPK signalling. This signalling cascade increased proliferation and anchorage-independent growth in BALB/c mouse JB6 epidermal cells (Camalier et al., 2010).

Our findings of their exclusive depletion under hypoxia highlight the importance of Na^+ transporters, including $Na_v1.5$ and those involved in amino acid and phosphate transport, in TNBC cell proliferation under hypoxic conditions. These channels could be promising therapeutic targets in hypoxic TNBC.

4.2.2 Fewer Na^+ transporters identified as contributor to MDA-MB-468 cell proliferation under hypoxia

In contrast, MDA-MB-468 cells showed no significant hits and less depletion with a narrower log_2FC compared to MDA-MB-231 cells. *GRIN3A*, *SLC22A12*, and *SLC34A3* were identified through hypoxia-exclusive depletion. *GRIN3A* encodes a subunit of the NMDA receptor (Sucher et al., 1995; Eriksson et al., 2002). *SLC22A12* encodes for URAT1, a kidney urate-anion transporter (Enomoto et al., 2002). The role of SLC22A12 in breast cancer remains largely unexplored. However, according to the Human Protein Atlas, *SLC22A12* exhibits very low RNA expression levels in breast cancer tissues while protein expression data for *SLC22A12* in breast cancer is either absent or not well-characterised. *SLC34A3*, similarly to *SLC34A2*, encodes for a Na^+-phosphate cotransporter (NaP_i-IIc) (Segawa et al., 2002).

The top-depleted gRNA targeting *FXYD5*, which regulates NKA activity, was depleted exclusively under hypoxia in both cell lines, although there was no significant gRNA depletion based on the FDR threshold. Depletion of gRNAs targeting *FXYD5* may reflect the need to maintain Na^+ gradients, which are essential for normal cellular function, during hypoxia (Leslie et al., 2019; Bernal et al., 2023; Clausen and Poulsen, 2013). *FXYD5* encodes for FXYD domain-containing ion transport regulator 5, also called dysadherin. Dysadherin is overexpressed in many cancers and has been shown to downregulate E-cadherin, promoting EMT and metastasis (Ino et al., 2002; Lubarski et al., 2005).

4.2.3 Clinical relevance

Despite the identification of Na^+ transporters which appear involved in hypoxic TNBC cell proliferation, like *SCN5A*, analysis of TCGA data did not reveal a significant correlation between the mRNA levels of any of the genes of interest and overall survival (OS) in TNBC. This lack of correlation may reflect redundancy among Na^+ transporters or post-translational regulation, which cannot be captured by mRNA-based datasets such as TCGA. The roles of these transporters in metastasis or treatment response warrant further investigation. Additional endpoints, such as metastasis-free survival or recurrence, may provide more informative indicators of clinical relevance.

4.3 *SCN5A* and TNBC cell proliferation under hypoxia

In the context of the CRISPRi screen, *SCN5A* emerged as a hypoxia-specific hit in MDA-MB-231 cells, with one of the five targeting gRNAs meeting the FDR threshold and the overall set showing significant depletion based on the unadjusted p-value. The *SCN5A* gRNA depletion suggests a role of $Na_v1.5$ in supporting hypoxic TNBC cell proliferation in this cell line. $Na_v1.5$-mediated Na^+ influx can influence intracellular pH, cell volume, and metastatic potential (Roger et al., 2003; Brisson et al., 2013). Previous studies demonstrated that $Na_v1.5$ expression in breast cancer is linked to invasiveness and metastasis (Fraser et al., 2005; Brackenbury et al., 2007). Fraser et al. (2005) demonstrated *SCN5A* expression in metastatic breast cancer cell lines, showing that MDA-MB-231 cells exhibit large TTX-sensitive VGSC currents, which correlate with cell invasion in Matrigel assays. Brackenbury et al. (2007) further showed that silencing *SCN5A* by siRNA in MDA-MB-231 cells reduced invasion, linking the gene to metastatic behaviour in TNBC.

Notably, *SCN5A* was not a significant hit in MDA-MB-468 cells. MDA-MB-468 cells express $Na_v1.5$, but with smaller inward Na^+ currents, typically a peak current desnity of ~1–2 pA/pF compared to ~3–20 pA/pF in MDA-MB-231 cells (Roger et al., 2003; Fraser et al., 2005; Nelson et al., 2015; Aydar et al., 2016). This difference may reflect lower $Na_v1.5$ expression or activity in MDA-MB-468, potentially explaining the lack of depletion in our screen. This is consistent with previous reports that MDA-MB-231 cells exhibit a mesenchymal-like phenotype with higher invasiveness, compared to the more epithelial-like MDA-MB-468

(Gradek et al., 2019). Gradek et al. (2019) showed by scanning electron microscopy that MDA-MB-231 cells have a typical mesenchymal phenotype; spindle-shaped and multiple filopodia. *SCN5A* knockdown, using specific small-hairpin RNA, lead to a less elongated morphology, fewer filopodia and reduced cell invasiveness in a Matrigel assay. They also demonstrated reduced expression of *SNAI1*, an EMT-inducing transcription factor, in the *SCN5A* knock down cells.

Given that the screen was designed to uncover hypoxia-specific effects, the differential *SCN5A* dependency observed between MDA-MB-231 and MDA-MB-468 cells suggests intrinsic differences in Na^+ channel activity can influence the effects of hypoxia on proliferation between TNBC subtypes. Another consideration is that dCas9-KRAB expression can vary between cell lines, however, downregulation of target genes and phenotypic effects are typically still comparable (Edenhofer et al., 2024), supporting the conclusion that *SCN5A* contributes more to cell proliferation under hypoxia in MDA-MB-231 cells.

4.4 Technical strengths and limitations

4.4.1 gRNA representation and control performance

Our screen used five gRNAs per gene and three non-targeting scrambled controls. This approach balanced feasibility under time and financial constraints with reproducibility, although it limits statistical power compared to larger libraries such as those described by Horlbeck et al. (2016) or Sanson et al. (2018), which include hundreds of control gRNAs to better minimise bias from off-target effects and increase statistical power (Horlbeck et al., 2016; Sanson et al., 2018).

In our CRISPRi screen, scrambled control gRNAs displayed inconsistent behaviour in both cell lines, with some enriched by more than 1 $\log_2$ FC and others depleted by more than –0.5 $\log_2$ FC. As these gRNAs are designed to be non-targeting, such variability raises concerns about off-target, especially given that negative control gRNAs are expected to cluster around

0 $\log_2$ FC and define the baseline distribution in CRISPRi screen analyses (Usluer et al., 2023; Park et al., 2023).

In addition, using only the top-depleted gRNA for each gene introduces bias into the interpretation of results. If there are issues of off-target effects, the top-depleted gRNA may not accurately represent the importance of the gene.

To address these limitations, future studies could use larger gRNA libraries with additional non-targeting controls, and independently validate candidate hits using siRNA or individual gRNA knockdowns to ensure observed effects are reproducible and not due to off-target or library biases.

4.4.2 Timing of hypoxic culture

Essential genes were not consistently depleted over time; this may be due to insufficient library coverage or pre-hypoxia selection effects. After transduction with the gRNA library, there was an 11-day period before culture under hypoxia. This time included 7 days of hygromycin selection, followed by 4 days of culture to maintain a coverage of 500 for the screen. This approach was necessary to ensure library representation and sufficient antibiotic selection, which are critical for maintaining screen integrity. However, the 11-day period may have allowed selective pressures to alter gRNA representation before exposure to hypoxia. For example, gRNAs reducing proliferation in normoxia could have been lost before hypoxia, masking their effect. While our Day 0 control allowed us to partially correct for pre-hypoxia selection effects, hypoxic culture would ideally begin as soon as selection is complete to minimise early dropout. As Gilbert et al. (2014) and others have shown, gRNA-mediated effects on cell fitness typically manifest by 5–7 days post-transduction (Gilbert et al., 2014). Thus, future studies should aim to shorten the interval between selection and hypoxia and include intermediate timepoints to monitor gRNA representation, helping to ensure that early dropout does not mask hypoxia-specific hits.

Furthermore, *HIF1A* and *HIF2A* gRNAs were not depleted under hypoxia. Lack of depletion may reflect that, while HIF1α and HIF2α expression is indeed required, their activity is regulated by hypoxia at the protein level rather than at the transcriptional level. HIF1α and HIF2α mRNAs are constitutively transcribed and translated, but HIF-α proteins are regulated at the protein level by rapid degradation under normoxic conditions via the VHL–PHD pathway, whereas HIF-1α is induced under hypoxia by protein stabilisation (Wenger et al., 1997; Huang et al., 1998) Wang et al., 1995; Semenza, 2003; Cavadas et al., 2013). It has been shown that hypoxia-induced upregulation of HIF protein levels occurs without corresponding increases in RNA expression (Krieg et al., 2000). Our findings align with these reports; since CRISPRi represses transcription, depletion of HIF1A or HIF2A transcripts may not translate into a strong phenotypic effect in this screen, consistent with the lack of gRNA depletion observed in our data.

Lack of gRNA depletion under hypoxia could also be explained by compensatory mechanisms between *HIF1A* and *HIF2A*. Knockout studies suggest that loss of one HIF isoform can trigger upregulation of the other (Koh et al., 2011). Koh et al. (2011) demonstrated that in several cancer cell lines, including pancreatic (PANC-1), glioblastoma (LN229 and U87), and renal carcinoma (RCC4 and 786-O), loss of HIF-1α was lead to increased transactivation of HIF-2α. This compensatory shift was driven by hypoxia-associated factor (HAF)**,** which binds to both HIF isoforms. HAF is an E3 ubiquitin ligase that ubiquitinates HIF-1α, promoting its degradation. However, HAF increases HIF-2α transactivating activity. HAF switches the hypoxic response from HIF-1α–dependent to a HIF-2α–dependent which activates genes such as *MMP9*, *PAI-1*, and *OCT-3/4*, which are associated with invasion. The switch to a HIF-2α–dependent hypoxia response also resulted in highly aggressive tumours *in vivo*. Interestingly, HAF overexpression did not alter HIF-2α protein levels but was essential for its activation, indicating a role in maintaining hypoxic signalling in the absence of HIF-1α. These mechanistic insights help explain why *HIF1A* or *HIF2A* knockdown alone may not reduce proliferation in our screen. Dual knockdown of *HIF1A* and *HIF2A* could clarify whether compensatory mechanisms mask phenotypic effects in hypoxia, particularly when assessing proliferation.

The duration of hypoxia may not have been prolonged enough or too long to reveal effects on proliferation. Although we used a 7-day hypoxic exposure, some studies define chronic hypoxia as lasting up to several weeks (Muz et al., 2015). However, our choice of 7 days reflects a balance between ensuring sufficient phenotypic impact and limiting passaging. It also aligns with previous CRISPR-based proliferation screens showing that effects on proliferation typically become measurable between 5–7 days post-transduction (Gilbert et

al., 2014). Longer exposure to hypoxia could improve visualisation of gRNA depletion but our design remains justified for initial identification of hypoxia-specific hits.

4.4.3 Cell line-specific effects

MDA-MB-468 cells exhibited a narrower range of $\log_2$ FC and fewer significant hits compared to MDA-MB-231. This limited sensitivity to hypoxia in MDA-MB-468 could possibly be due to either intrinsic biological resistance to hypoxia-induced proliferation changes or technical limitations, such as low lentiviral transduction efficiency. Due to limited control lentivirus, we were unable to determine an MOI value that resulted in a transduction efficiency over 30% in MDA-MB-468 cells (Sanson et al., 2018). Future CRISPRi screens should optimise transduction efficiency and MOI in MDA-MB-468 cells, and could extend to additional TNBC lines to assess whether hypoxia-specific Na^+ transporter dependencies can be generalised.

4.5 Pharmacological inhibition of $Na_v1.5$ with propafenone

Propafenone inhibited both transient and persistent Na^+ currents in MDA-MB-231 cells, which endogenously express $Na_v1.5$, predominantly the neonatal splice variant (Roger et al., 2003; Fraser et al., 2005; Brackenbury et al., 2007). This result is consistent with prior work showing that propafenone blocks VGSCs, such as $Na_v1.5$, in MDA-MB-231, in a state-dependent manner (Edrich et al., 2005). MDA-MB-231 cells express both $Na_v1.5$ and $Na_v1.7$. However, $Na_v1.7$ contributes only ~9% of the total VGSC current (Fraser et al., 2005; Brackenbury et al., 2007), suggesting that our findings are predominantly driven by $Na_v1.5$ activity.

Current-voltage relationship analysis confirmed that 100 μM propafenone prevents activation following depolarisation from -120 mV to -10 mV, without significantly affecting time-to-peak

or the fast (τf) and slow (τs) inactivation constants. The observed inhibition pattern aligns with a model where propafenone preferentially binds to the open state of $Na_v1.5$. Our findings are consistent with previous studies inhibiting peak Na^+ currents with propafenone in cardiac myocytes (Kohlhardt 1984; Holmes 2021).

Interestingly, propafenone's reversible inhibition contrasts with the activity of other VGSC inhibitors such as eslicarbazepine acetate (S-Lic), which shows minimal recovery of peak Na^+ current following washout (Leslie et al., 2020). S-Lic preferentially blocks during slow inactivation and may be trapped in the cytoplasm (Hebeisen et al., 2015; Bonifacio et al., 2017). However, both propafenone and S-Lic have hydroxyl groups.

The *in vitro* concentrations used in this project (1–100 μM) were aligned with previous studies (Wang et al., 2013; Holmes et al., 2021). Although these concentrations exceed clinical plasma levels, 0.20 to 0.60 micrograms/ml (Steurer et al., 1991), this study demonstrated proof of concept for the inhibition of $Na_v1.5$-mediated Na^+ current using propafenone in TNBC cells. Further pharmacological studies should include dose-response testing at clinically relevant concentrations, isoform-specific evaluation of VGSC variants, and validation in additional TNBC cell lines or xenograft models to determine translational potential. Further studies of the inhibitory effects of propafenone in TNBC cells with differing $Na_v1.5$ expression are needed, particularly in MDA-MB-468, where $Na_v1.5$ is expressed but Na^+ currents are not detected (Fraser et al., 2005; Aydar et al., 2016).

4.6 Future directions

Future studies should validate CRISPRi hits using siRNA or individual gRNA knockdown. It would then be useful to evaluate the effects of these knockdowns on $[Na^+]_i$, using SBFI-AM imaging, and cell survival. This approach would help identify which Na^+ channels are physiologically relevant potential therapeutic targets in hypoxic breast cancer.

Functionally significant Na^+ channel knockdowns could be cultured in a TNBC spheroid model. Spheroid models better mimic the tumour microenvironment, often developing oxygen gradients, creating regions of hypoxia similar to those observed in solid tumours (Hirschhaeuser et al., 2010; Grimes et al., 2014). Viability, wound healing and invasion

assays would evaluate the impact of the channel knockdown on tumour behaviours. For 3D invasion, spheroids can be embedded into collagen or Matrigel matrices, and invasion measured as the outgrowth of cells from the spheroid. Alternatively, Transwell assays using spheroid-derived cells or cells with specific knockdowns can be used to assess invasion. For wound healing or migration, a scratch assay can be performed on monolayers derived from spheroid-dissociated cells or stable knockdowns.

To further evaluate propafenone's inhibition of $Na_v1.5$ in MDA-MB-231 cells, it is important to analyse current-voltage relationships using lower concentrations (1–30 μM). At these concentrations, incomplete inhibition would allow for evaluation of activation and inactivation kinetics. Additionally, isoform-specific testing using cells over expressing distinct $Na_v1.5$ splice variants would be valuable since some local anaesthetics, such as lidocaine, have different affinities for the neonatal and adult $Na_v1.5$ isoforms (Elajnaf et al., 2018). Testing propafenone on cells expressing the adult isoform would evaluate whether both variants are equally susceptible. It would also be valuable to validate findings in a second TNBC cell line, such as MDA-MB-468, which express $Na_v1.5$ but no inward Na^+ current is detected (Fraser et al., 2005; Aydar et al., 2016). Finally, xenograft mouse breast cancer models could be used to assess whether pharmacological inhibition of $Na_v1.5$ with propafenone reduces tumour progression or metastatic burden.

In addition, future work should address technical and biological limitations observed in this study. This includes increasing gRNA coverage and non-targeting controls, shortening the interval between library selection and hypoxic exposure, and monitoring gRNA representation over time. Dual knockdowns of HIF1A and HIF2A could clarify potential compensatory effects, while optimising MOI and transduction efficiency in MDA-MB-468 and testing additional TNBC lines would ensure generalisability. Collectively, these studies would strengthen the identification of Na^+ transporters as potential therapeutic targets and elucidate their functional relevance in hypoxic TNBC proliferation.

4.7 Clinical significance and conclusions

Our findings may support the involvement of various Na^+ channels and transporters in hypoxic TNBC cell proliferation. *SCN5A* was identified as a significant hit in the CRISPRi screen, although only one of five gRNAs met the FDR threshold. The lack of significance highlights a potential limitation in statistical power or variability in gRNA efficiency and

underscores the need for individual validation experiments. Nonetheless, gRNA depletion of *SCN5A* is consistent with the established role of $Na_v1.5$ in promoting cancer cell invasiveness and metastatic potential and supports the concept of $Na_v1.5$ as a promising therapeutic target for hypoxic TNBC.

While TCGA data did not support the use of the Na^+ transporter genes identified as prognostic markers based on mRNA expression, their functional relevance to proliferation under hypoxia suggests therapeutic potential. For example, pharmacological inhibition of $Na_v1.5$ with propafenone should be investigated further in preclinical models, particularly in hypoxic contexts. In summary, while our data provide preliminary support that Na^+ transporters may contribute to TNBC proliferation under hypoxia, these findings should be interpreted with caution given the limitations of the screen. Further work is needed to establish whether targeting these Na^+ transporters could complement existing therapies, by reducing cancer cell proliferation and invasiveness in hypoxic TNBC.

References

Allot, E., Denjoy, I., 1996. Comparison of the safety and efficacy of flecainide versus propafenone in hospital out-patients with symptomatic paroxysmal atrial fibrillation/flutter. The American Journal of Cardiology 77, 66A-71A. https://doi.org/10.1016/S0002-9149(97)89120-5

Andrejew, R., Oliveira-Giacomelli, Á., Ribeiro, D.E., Glaser, T., Arnaud-Sampaio, V.F., Lameu, C., Ulrich, H., 2020. The P2X7 Receptor: Central Hub of Brain Diseases. Front. Mol. Neurosci. 13, 124. https://doi.org/10.3389/fnmol.2020.00124

Armstrong, C.M., Bezanilla, F., 1977. Inactivation of the sodium channel. II. Gating current experiments. The Journal of general physiology 70, 567–590. https://doi.org/10.1085/jgp.70.5.567

Aydar, E., Stratton, D., Fraser, S.P., Djamgoz, M.B.A., Palmer, C., 2016. Sigma-1 receptors modulate neonatal Nav1.5 ion channels in breast cancer cell lines. Eur Biophys J 45, 671–683. https://doi.org/10.1007/s00249-016-1135-0

Ayka, A., Şehirli, A.Ö., 2020. The Role of the SLC Transporters Protein in the Neurodegenerative Disorders. Clin Psychopharmacol Neurosci 18, 174–187. https://doi.org/10.9758/cpn.2020.18.2.174

Baenke, F., Chaneton, B., Smith, M., Van Den Broek, N., Hogan, K., Tang, H., Viros, A., Martin, M., Galbraith, L., Girotti, M.R., Dhomen, N., Gottlieb, E., Marais, R., 2016. Resistance to BRAF inhibitors induces glutamine dependency in melanoma cells. Molecular Oncology 10, 73–84. https://doi.org/10.1016/j.molonc.2015.08.003

Barrett, T., et al., 2018. Quantification of Total and Intracellular Sodium Concentration in Primary Prostate Cancer and Adjacent Normal Prostate Tissue With Magnetic Resonance Imaging. Invest Radiol 53, 450–456. https://doi.org/10.1097/RLI.0000000000000470

Bates, D., Mächler, M., Bolker, B., Walker, S., 2015. Fitting Linear Mixed-Effects Models Using lme4. J. Stat. Soft. 67. https://doi.org/10.18637/jss.v067.i01

Befani, C., Liakos, P., 2018. The role of hypoxia-inducible factor-2 alpha in angiogenesis. Journal Cellular Physiology 233, 9087–9098. https://doi.org/10.1002/jcp.26805

Bellmunt, J., et al., 2017. Pembrolizumab as Second-Line Therapy for Advanced Urothelial Carcinoma. N Engl J Med 376, 1015–1026. https://doi.org/10.1056/NEJMoa1613683

Blancher, C., Harris, A.L., 1998. The molecular basis of the hypoxia response pathway: tumour hypoxia as a therapy target. Cancer and Metastasis Reviews 17, 187–194. https://doi.org/10.1023/A:1006002419244

Bobko, A.A., Eubank, T.D., Driesschaert, B., Dhimitruka, I., Evans, J., Mohammad, R., Tchekneva, E.E., Dikov, M.M., Khramtsov, V.V., 2017. Interstitial Inorganic Phosphate as a Tumor Microenvironment Marker for Tumor Progression. Sci Rep 7, 41233. https://doi.org/10.1038/srep41233

Bode, B.P., Fuchs, B.C., Hurley, B.P., Conroy, J.L., Suetterlin, J.E., Tanabe, K.K., Rhoads, D.B., Abcouwer, S.F., Souba, W.W., 2002. Molecular and functional analysis of glutamine uptake in human hepatoma and liver-derived cells. American Journal of Physiology-Gastrointestinal and Liver Physiology 283, G1062–G1073. https://doi.org/10.1152/ajpgi.00031.2002

Bonotto, M., Gerratana, L., Poletto, E., Driol, P., Giangreco, M., Russo, S., Minisini, A.M., Andreetta, C., Mansutti, M., Pisa, F.E., Fasola, G., Puglisi, F., 2014. Measures of Outcome in Metastatic Breast Cancer: Insights From a Real-World Scenario. The Oncologist 19, 608–615. https://doi.org/10.1634/theoncologist.2014-0002

Brackenbury, W.J., Chioni, A.-M., Diss, J.K.J., Djamgoz, M.B.A., 2007. The neonatal splice variant of Nav1.5 potentiates in vitro invasive behaviour of MDA-MB-231 human breast cancer cells. Breast Cancer Res Treat 101, 149–160. https://doi.org/10.1007/s10549-006-9281-1

Brackenbury, W.J., Djamgoz, M.B.A., 2006. Activity-dependent regulation of voltage-gated Na+ channel expression in Mat-LyLu rat prostate cancer cell line. The Journal of Physiology 573, 343–356. https://doi.org/10.1113/jphysiol.2006.106906

Brackenbury, W.J., Isom, L.L., 2011. Na+ Channel ? Subunits: Overachievers of the Ion Channel Family. Front. Pharmacol. 2. https://doi.org/10.3389/fphar.2011.00053

Bray, F., Ferlay, J., Soerjomataram, I., Siegel, R.L., Torre, L.A., Jemal, A., 2018. Global cancer statistics 2018: GLOBOCAN estimates of incidence and mortality worldwide for 36 cancers in 185 countries. CA A Cancer J Clinicians 68, 394–424. https://doi.org/10.3322/caac.21492

Breast Cancer Now. Available at: https://breastcancernow.org/about-us/media/facts-statistics#:~:text=Around%2055%2C000%20women%20and%20400,are%20diagnosed%20with%20breast%20cancer. Accessed August 2023

Brisson, L., et al., 2013. NaV1.5 sodium channels allosterically regulate the NHE-1 exchanger and promote breast cancer cell invadopodial activity. Journal of Cell Science jcs.123901. https://doi.org/10.1242/jcs.123901

Brisson, L., Gillet, L., Calaghan, S., Besson, P., Le Guennec, J.-Y., Roger, S., Gore, J., 2011. NaV1.5 enhances breast cancer cell invasiveness by increasing NHE1-dependent H+ efflux in caveolae. Oncogene 30, 2070–2076. https://doi.org/10.1038/onc.2010.574

Brouckaert, O., et al., 2012. Update on triple-negative breast cancer: prognosis and management strategies. International Journal of Women's Health, 511. https://doi.org/10.2147/IJWH.S18541

Burstein, M.D., et al., 2015. Comprehensive Genomic Analysis Identifies Novel Subtypes and Targets of Triple-Negative Breast Cancer. Clinical Cancer Research 21, 1688–1698. https://doi.org/10.1158/1078-0432.CCR-14-0432

Cai, S.-L., et al., 2023. Characteristics of recurrence, predictors for relapse and prognosis of rapid relapse triple-negative breast cancer. Front. Oncol. 13, 1119611. https://doi.org/10.3389/fonc.2023.1119611

Camalier, C.E., Young, M.R., Bobe, G., Perella, C.M., Colburn, N.H., Beck, G.R., 2010. Elevated Phosphate Activates N-ras and Promotes Cell Transformation and Skin Tumorigenesis. Cancer Prevention Research 3, 359–370. https://doi.org/10.1158/1940-6207.CAPR-09-0068

Capatina, A.L., Malcolm, J.R., Stenning, J., Moore, R.L., Bridge, K.S., Brackenbury, W.J., Holding, A.N., 2024. Hypoxia-induced epigenetic regulation of breast cancer progression

and the tumour microenvironment. Front. Cell Dev. Biol. 12, 1421629. https://doi.org/10.3389/fcell.2024.1421629

Carey, L.A., et al., 2006. Race, Breast Cancer Subtypes, and Survival in the Carolina Breast Cancer Study. JAMA 295, 2492. https://doi.org/10.1001/jama.295.21.2492

Carroll, C.P., Bolland, H., Vancauwenberghe, E., Collier, P., Ritchie, A.A., Clarke, P.A., Grabowska, A.M., Harris, A.L., McIntyre, A., 2022. Targeting hypoxia regulated sodium driven bicarbonate transporters reduces triple negative breast cancer metastasis. Neoplasia 25, 41–52. https://doi.org/10.1016/j.neo.2022.01.003

Catterall, W.A., 2000. From Ionic Currents to Molecular Mechanisms. Neuron 26, 13–25. https://doi.org/10.1016/S0896-6273(00)81133-2

Catterall, W.A., 2014. Structure and function of voltage-gated sodium channels at atomic resolution. Experimental Physiology 99, 35–51. https://doi.org/10.1113/expphysiol.2013.071969

Catterall, W.A., Lenaeus, M.J., Gamal El-Din, T.M., 2020. Structure and Pharmacology of Voltage-Gated Sodium and Calcium Channels. Annu. Rev. Pharmacol. Toxicol. 60, 133–154. https://doi.org/10.1146/annurev-pharmtox-010818-021757

Chang, X., Wang, J., Jiang, H., Shi, L., Xie, J., 2019. Hyperpolarization-Activated Cyclic Nucleotide-Gated Channels: An Emerging Role in Neurodegenerative Diseases. Front. Mol. Neurosci. 12, 141. https://doi.org/10.3389/fnmol.2019.00141

Chaudhary, L.N., Wilkinson, K.H., Kong, A., 2018. Triple-Negative Breast Cancer. Surgical Oncology Clinics of North America 27, 141–153. https://doi.org/10.1016/j.soc.2017.08.004

Chavez, K.J., Garimella, S.V., Lipkowitz, S., 2011. Triple negative breast cancer cell lines: One tool in the search for better treatment of triple negative breast cancer. BD 32, 35–48. https://doi.org/10.3233/BD-2010-0307

Chen, D.-R., Chien, S.-Y., Kuo, S.-J., Teng, Y.-H., Tsai, H.-T., Kuo, J.-H., Chung, J.-G., 2010. SLC34A2 as a novel marker for diagnosis and targeted therapy of breast cancer. Anticancer Res 30, 4135–4140.

Chen, H., Boutros, P.C., 2011. VennDiagram: a package for the generation of highly-customizable Venn and Euler diagrams in R. BMC Bioinformatics 12, 35. https://doi.org/10.1186/1471-2105-12-35

Choi, A.H., O'Leary, M.P., Lu, J., Kim, S.-I., Fong, Y., Chen, N.G., 2018. Endogenous Akt Activity Promotes Virus Entry and Predicts Efficacy of Novel Chimeric Orthopoxvirus in Triple-Negative Breast Cancer. Molecular Therapy - Oncolytics 9, 22–29. https://doi.org/10.1016/j.omto.2018.04.001

Choi, H.I., An, G.Y., Baek, M., Yoo, E., Chai, J.C., Lee, Y.S., Jung, K.H., Chai, Y.G., 2021. BET inhibitor suppresses migration of human hepatocellular carcinoma by inhibiting SMARCA4. Sci Rep 11, 11799. https://doi.org/10.1038/s41598-021-91284-2

Ciriello, G., Cerami, E., Sander, C., Schultz, N., 2012. Mutual exclusivity analysis identifies oncogenic network modules. Genome Res. 22, 398–406. https://doi.org/10.1101/gr.125567.111

Condorelli, R., et al., 2018. Polyclonal RB1 mutations and acquired resistance to CDK 4/6 inhibitors in patients with metastatic breast cancer. Annals of Oncology 29, 640–645. https://doi.org/10.1093/annonc/mdx784

Corbet, C., Feron, O., 2017. Tumour acidosis: from the passenger to the driver's seat. Nat Rev Cancer 17, 577–593. https://doi.org/10.1038/nrc.2017.77

Cortes, J., et al., 2020. Pembrolizumab plus chemotherapy versus placebo plus chemotherapy for previously untreated locally recurrent inoperable or metastatic triple-negative breast cancer (KEYNOTE-355): a randomised, placebo-controlled, double-blind, phase 3 clinical trial. The Lancet 396, 1817–1828. https://doi.org/10.1016/S0140-6736(20)32531-9

Corut, A., Senyigit, A., Ugur, S.A., Altin, S., Ozcelik, U., Calisir, H., Yildirim, Z., Gocmen, A., Tolun, A., 2006. Mutations in SLC34A2 Cause Pulmonary Alveolar Microlithiasis and Are Possibly Associated with Testicular Microlithiasis. The American Journal of Human Genetics 79, 650–656. https://doi.org/10.1086/508263

Cui, Z., et al., 2024. Lactylproteome analysis indicates histone H4K12 lactylation as a novel biomarker in triple-negative breast cancer. Front. Endocrinol. 15, 1328679. https://doi.org/10.3389/fendo.2024.1328679

De Heer, E.C., Jalving, M., Harris, A.L., 2020. HIFs, angiogenesis, and metabolism: elusive enemies in breast cancer. Journal of Clinical Investigation 130, 5074–5087. https://doi.org/10.1172/JCI137552

DeMichele, A., et al., 2015. CDK 4/6 Inhibitor Palbociclib (PD0332991) in Rb+ Advanced Breast Cancer: Phase II Activity, Safety, and Predictive Biomarker Assessment. Clinical Cancer Research 21, 995–1001. https://doi.org/10.1158/1078-0432.CCR-14-2258

Dent, R., et al., 2007. Triple-Negative Breast Cancer: Clinical Features and Patterns of Recurrence. Clinical Cancer Research 13, 4429–4434. https://doi.org/10.1158/1078-0432.CCR-06-3045

Dewadas, H.D., et al., 2019. The role of HIF-1α, CBP and p300 in the regulation of Nav1.5 expression in breast cancer cells. Gene Reports 16, 100405. https://doi.org/10.1016/j.genrep.2019.100405

Djamgoz, M.B.A., Fraser, S.P., Brackenbury, W.J., 2019. In Vivo Evidence for Voltage-Gated Sodium Channel Expression in Carcinomas and Potentiation of Metastasis. Cancers 11, 1675. https://doi.org/10.3390/cancers11111675

Doroshow, D.B., Eder, J.P., LoRusso, P.M., 2017. BET inhibitors: a novel epigenetic approach. Annals of Oncology 28, 1776–1787. https://doi.org/10.1093/annonc/mdx157

Edenhofer, F.C., Térmeg, A., Ohnuki, M., Jocher, J., Kliesmete, Z., Briem, E., Hellmann, I., Enard, W., 2024. Generation and characterization of inducible KRAB-dCas9 iPSCs from primates for cross-species CRISPRi. iScience 27, 110090. https://doi.org/10.1016/j.isci.2024.110090

Edrich, T., Wang, S.-Y., Wang, G.K., 2005a. State-dependent Block of Human Cardiac hNav1.5 Sodium Channels by Propafenone. J Membrane Biol 207, 35–43. https://doi.org/10.1007/s00232-005-0801-4

Edrich, T., Wang, S.-Y., Wang, G.K., 2005b. State-dependent Block of Human Cardiac hNav1.5 Sodium Channels by Propafenone. J Membrane Biol 207, 35–43. https://doi.org/10.1007/s00232-005-0801-4

Eggersmann, T.K., Degenhardt, T., Gluz, O., Wuerstlein, R., Harbeck, N., 2019. CDK4/6 Inhibitors Expand the Therapeutic Options in Breast Cancer: Palbociclib, Ribociclib and Abemaciclib. BioDrugs 33, 125–135. https://doi.org/10.1007/s40259-019-00337-6

Enomoto, A., Kimura, H., Chairoungdua, A., Shigeta, Y., Jutabha, P., Ho Cha, S., Hosoyamada, M., Takeda, M., Sekine, T., Igarashi, T., Matsuo, H., Kikuchi, Y., Oda, T., Ichida, K., Hosoya, T., Shimokata, K., Niwa, T., Kanai, Y., Endou, H., 2002. Molecular identification of a renal urate–anion exchanger that regulates blood urate levels. Nature 417, 447–452. https://doi.org/10.1038/nature742

Epstein, T., Xu, L., Gillies, R.J., Gatenby, R.A., 2014. Separation of metabolic supply and demand: aerobic glycolysis as a normal physiological response to fluctuating energetic demands in the membrane. Cancer Metab 2, 7. https://doi.org/10.1186/2049-3002-2-7

Eriksson, M., Nilsson, A., Froelich-Fabre, S., Åkesson, E., Dunker, J., Seiger, Å., Folkesson, R., Benedikz, E., Sundström, E., 2002. Cloning and expression of the human N-methyl-d-aspartate receptor subunit NR3A. Neuroscience Letters 321, 177–181. https://doi.org/10.1016/S0304-3940(01)02524-1

Ewels, P., Peltzer, A., Fillinger, S., Patel, H., Alneberg, J., Wilm, A., Garcia, M.U., Tommaso, P.D., Nahnsen, S., 2020. The nf-core framework for community-curated bioinformatics pipelines. Nat Biotechnol. doi: 10.1038/s41587-020-0439-x.

Fairhurst, C., Doran, T., Martin, F., Watt, I., Bland, M., Brackenbury, W.J., 2023. Sodium channel-inhibiting drugs and cancer-specific survival: a population-based study of electronic primary care data. BMJ Open 13, e064376. https://doi.org/10.1136/bmjopen-2022-064376

Fan, J., Kamphorst, J.J., Mathew, R., Chung, M.K., White, E., Shlomi, T., Rabinowitz, J.D., 2013. Glutamine-driven oxidative phosphorylation is a major ATP source in transformed mammalian cells in both normoxia and hypoxia. Molecular Systems Biology 9, 712. https://doi.org/10.1038/msb.2013.65

Fei, L., Gill, J.S., McKenna, W.J., Camm, A.J., 1993. Effects of propafenone on calcium currents in single ventricular myocytes of guinea-pig. British J Pharmacology 109, 178–182. https://doi.org/10.1111/j.1476-5381.1993.tb13550.x

Feild, J.A., Zhang, L., Brun, K.A., Brooks, D.P., Edwards, R.M., 1999. Cloning and Functional Characterization of a Sodium-Dependent Phosphate Transporter Expressed in Human Lung and Small Intestine. Biochemical and Biophysical Research Communications 258, 578–582. https://doi.org/10.1006/bbrc.1999.0666

Fernandes, C.F., Godoy, J.R., Döring, B., Cavalcanti, M.C.O., Bergmann, M., Petzinger, E., Geyer, J., 2007. The novel putative bile acid transporter SLC10A5 is highly expressed in liver and kidney. Biochemical and Biophysical Research Communications 361, 26–32. https://doi.org/10.1016/j.bbrc.2007.06.160

Finn, R.S., et al., 2009. PD 0332991, a selective cyclin D kinase 4/6 inhibitor, preferentially inhibits proliferation of luminal estrogen receptor-positive human breast cancer cell lines in vitro. Breast Cancer Res 11, R77. https://doi.org/10.1186/bcr2419

Forsythe, J.A., Jiang, B.-H., Iyer, N.V., Agani, F., Leung, S.W., Koos, R.D., Semenza, G.L., 1996. Activation of Vascular Endothelial Growth Factor Gene Transcription by Hypoxia-Inducible Factor 1. Molecular and Cellular Biology 16, 4604–4613. https://doi.org/10.1128/MCB.16.9.4604

Fouad, Y.A., Aanei, C., 2017. Revisiting the hallmarks of cancer. Am J Cancer Res 7, 1016–1036.

Fraser, S.P., et al., 2005. Voltage-Gated Sodium Channel Expression and Potentiation of Human Breast Cancer Metastasis. Clinical Cancer Research 11, 5381–5389. https://doi.org/10.1158/1078-0432.CCR-05-0327

Fraser, S.P., Salvador, V., Manning, E.A., Mizal, J., Altun, S., Raza, M., Berridge, R.J., Djamgoz, M.B.A., 2003. Contribution of functional voltage-gated Na+ channel expression to cell behaviors involved in the metastatic cascade in rat prostate cancer: I. lateral motility. Journal Cellular Physiology 195, 479–487. https://doi.org/10.1002/jcp.10312

Garon, E.B., et al., 2015. Pembrolizumab for the Treatment of Non–Small-Cell Lung Cancer. N Engl J Med 372, 2018–2028. https://doi.org/10.1056/NEJMoa1501824

Ge, J.Y., et al., 2020. Acquired resistance to combined BET and CDK4/6 inhibition in triple-negative breast cancer. Nat Commun 11, 2350. https://doi.org/10.1038/s41467-020-16170-3

Gentili, C., Giordano, F., Alois, A., Massa, E., Bianconi, L., 1992. Efficacy of intravenous propafenone in acute atrial fibrillation complicating open-heart surgery. American Heart Journal 123, 1225–1228. https://doi.org/10.1016/0002-8703(92)91026-W

Gholami, S., Chen, C.-H., Belin, L.J., Lou, E., Fujisawa, S., Antonacci, C., Carew, A., Chen, N.G., De Brot, M., Zanzonico, P.B., Szalay, A.A., Fong, Y., 2013. Vaccinia virus GLV-1h153 is a novel agent for detection and effective local control of positive surgical margins for breast cancer. Breast Cancer Res 15, R26. https://doi.org/10.1186/bcr3404

Girardi, E., César-Razquin, A., Lindinger, S., Papakostas, K., Konecka, J., Hemmerich, J., Kickinger, S., Kartnig, F., Gürtl, B., Klavins, K., Sedlyarov, V., Ingles-Prieto, A., Fiume, G., Koren, A., Lardeau, C.-H., Kumaran Kandasamy, R., Kubicek, S., Ecker, G.F., Superti-Furga, G., 2020. A widespread role for SLC transmembrane transporters in resistance to cytotoxic drugs. Nat Chem Biol 16, 469–478. https://doi.org/10.1038/s41589-020-0483-3

Goel, S., DeCristo, M.J., McAllister, S.S., Zhao, J.J., 2018. CDK4/6 Inhibition in Cancer: Beyond Cell Cycle Arrest. Trends in Cell Biology 28, 911–925. https://doi.org/10.1016/j.tcb.2018.07.002

Goldin, A.L., 2003. Mechanisms of sodium channel inactivation. Current Opinion in Neurobiology 13, 284–290. https://doi.org/10.1016/S0959-4388(03)00065-5

Goldin, A.L., Barchi, R.L., Caldwell, J.H., Hofmann, F., Howe, J.R., Hunter, J.C., Kallen, R.G., Mandel, G., Meisler, M.H., Netter, Y.B., Noda, M., Tamkun, M.M., Waxman, S.G., Wood, J.N., Catterall, W.A., 2000. Nomenclature of Voltage-Gated Sodium Channels. Neuron 28, 365–368. https://doi.org/10.1016/S0896-6273(00)00116-1

Gong, X., et al., 2017. Genomic Aberrations that Activate D-type Cyclins Are Associated with Enhanced Sensitivity to the CDK4 and CDK6 Inhibitor Abemaciclib. Cancer Cell 32, 761-776.e6. https://doi.org/10.1016/j.ccell.2017.11.006

Grimes, D.R., Kelly, C., Bloch, K., Partridge, M., 2014. A method for estimating the oxygen consumption rate in multicellular tumour spheroids. J. R. Soc. Interface. 11, 20131124. https://doi.org/10.1098/rsif.2013.1124

Gucalp, A., et al., 2020. Phase II trial of bicalutamide in combination with palbociclib for the treatment of androgen receptor (+) metastatic breast cancer. JCO 38, 1017–1017. https://doi.org/10.1200/JCO.2020.38.15_suppl.1017

Hallett, R.M., Dvorkin-Gheva, A., Bane, A., Hassell, J.A., 2012. A Gene Signature for Predicting Outcome in Patients with Basal-like Breast Cancer. Sci Rep 2, 227. https://doi.org/10.1038/srep00227

Hammarström, A., Gage, P., 2002. Hypoxia and persistent sodium current. European Biophysics Journal 31, 323–330. https://doi.org/10.1007/s00249-002-0218-2

Hart, T., Brown, K.R., Sircoulomb, F., Rottapel, R., Moffat, J., 2014. Measuring error rates in genomic perturbation screens: gold standards for human functional genomics. Molecular Systems Biology 10, 733. https://doi.org/10.15252/msb.20145216

Hibino, S., Kawazoe, T., Kasahara, H., Itoh, S., Ishimoto, T., Sakata-Yanagimoto, M., Taniguchi, K., 2021. Inflammation-Induced Tumorigenesis and Metastasis. IJMS 22, 5421. https://doi.org/10.3390/ijms22115421

Hille, B., 1978. Ionic channels in excitable membranes. Current problems and biophysical approaches. Biophysical Journal 22, 283–294. https://doi.org/10.1016/S0006-3495(78)85489-7

Hirschhaeuser, F., Menne, H., Dittfeld, C., West, J., Mueller-Klieser, W., Kunz-Schughart, L.A., 2010. Multicellular tumor spheroids: An underestimated tool is catching up again. Journal of Biotechnology 148, 3–15. https://doi.org/10.1016/j.jbiotec.2010.01.012

Hockings, J.K., Thorne, P.A., Kemp, M.Q., Morgan, S.S., Selmin, O., Romagnolo, D.F., 2006. The Ligand Status of the Aromatic Hydrocarbon Receptor Modulates Transcriptional Activation of BRCA-1 Promoter by Estrogen. Cancer Research 66, 2224–2232. https://doi.org/10.1158/0008-5472.CAN-05-1619

Hondeghem, L.M., Katzung, B.G., 1984. Antiarrhythmic Agents: The Modulated Receptor Mechanism of Action of Sodium and Calcium Channel-Blocking Drugs. Annu. Rev. Pharmacol. Toxicol. 24, 387–423. https://doi.org/10.1146/annurev.pa.24.040184.002131

Horlbeck, M.A., Gilbert, L.A., Villalta, J.E., Adamson, B., Pak, R.A., Chen, Y., Fields, A.P., Park, C.Y., Corn, J.E., Kampmann, M., Weissman, J.S., 2016. Compact and highly active next-generation libraries for CRISPR-mediated gene repression and activation. eLife 5, e19760. https://doi.org/10.7554/eLife.19760

Hu, Y., Gao, J., Wang, M., Li, M., 2021. Potential Prospect of CDK4/6 Inhibitors in Triple-Negative Breast Cancer. CMAR Volume 13, 5223–5237. https://doi.org/10.2147/CMAR.S310649

Huang, L.E., Arany, Z., Livingston, D.M., Bunn, H.F., 1996. Activation of Hypoxia-inducible Transcription Factor Depends Primarily upon Redox-sensitive Stabilization of Its α Subunit. Journal of Biological Chemistry 271, 32253–32259. https://doi.org/10.1074/jbc.271.50.32253

Huang, L.E., Gu, J., Schau, M., Bunn, H.F., 1998. Regulation of hypoxia-inducible factor 1α is mediated by an O_2 -dependent degradation domain via the ubiquitin-proteasome pathway. Proc. Natl. Acad. Sci. U.S.A. 95, 7987–7992. https://doi.org/10.1073/pnas.95.14.7987

Ino, Y., Gotoh, M., Sakamoto, M., Tsukagoshi, K., Hirohashi, S., 2002. Dysadherin, a cancer-associated cell membrane glycoprotein, down-regulates E-cadherin and promotes metastasis. Proc. Natl. Acad. Sci. U.S.A. 99, 365–370. https://doi.org/10.1073/pnas.012425299

Jacobs, M.A., Ouwerkerk, R., Kamel, I., Bottomley, P.A., Bluemke, D.A., Kim, H.S., 2009. Proton, diffusion-weighted imaging, and sodium (23Na) MRI of uterine leiomyomata after MR-guided high-intensity focused ultrasound: A preliminary study. J. Magn. Reson. Imaging 29, 649–656. https://doi.org/10.1002/jmri.21677

James, A.D., Leslie, T.K., Kaggie, J.D., Wiggins, L., Patten, L., Murphy O'Duinn, J., Langer, S., Labarthe, M.-C., Riemer, F., Baxter, G., McLean, M.A., Gilbert, F.J., Kennerley, A.J., Brackenbury, W.J., 2022. Sodium accumulation in breast cancer predicts malignancy and treatment response. Br J Cancer 127, 337–349. https://doi.org/10.1038/s41416-022-01802-w

Jarząb, B., Wiench, M., Fujarewicz, K., Simek, K., Jarząb, M., Oczko-Wojciechowska, M., Włoch, J., Czarniecka, A., Chmielik, E., Lange, D., Pawlaczek, A., Szpak, S., Gubała, E., Świerniak, A., 2005. Gene Expression Profile of Papillary Thyroid Cancer: Sources of Variability and Diagnostic Implications. Cancer Research 65, 1587–1597. https://doi.org/10.1158/0008-5472.CAN-04-3078

Jiang, D., Banh, R., Gamal El-Din, T.M., Tonggu, L., Lenaeus, M.J., Pomès, R., Zheng, N., Catterall, W.A., 2021. Open-state structure and pore gating mechanism of the cardiac sodium channel. Cell 184, 5151-5162.e11. https://doi.org/10.1016/j.cell.2021.08.021

Jiang, D., Zhang, J., Xia, Z., 2022. Structural Advances in Voltage-Gated Sodium Channels. Front. Pharmacol. 13, 908867. https://doi.org/10.3389/fphar.2022.908867

Jiang, Y.-Z., et al., 2019. Genomic and Transcriptomic Landscape of Triple-Negative Breast Cancers: Subtypes and Treatment Strategies. Cancer Cell 35, 428-440.e5. https://doi.org/10.1016/j.ccell.2019.02.001

Jin, H., Xu, C.-X., Lim, H.-T., Park, S.-J., Shin, J.-Y., Chung, Y.-S., Park, S.-C., Chang, S.-H., Youn, H.-J., Lee, K.-H., Lee, Y.-S., Ha, Y.-C., Chae, C.-H., Beck, G.R., Cho, M.-H., 2009. High Dietary Inorganic Phosphate Increases Lung Tumorigenesis and Alters Akt Signaling. Am J Respir Crit Care Med 179, 59–68. https://doi.org/10.1164/rccm.200802-306OC

Johnson, L., Mercer, K., Greenbaum, D., Bronson, R.T., Crowley, D., Tuveson, D.A., Jacks, T., 2001. Somatic activation of the K-ras oncogene causes early onset lung cancer in mice. Nature 410, 1111–1116. https://doi.org/10.1038/35074129

Ju, Y.K., Saint, D.A., Gage, P.W., 1996. Hypoxia increases persistent sodium current in rat ventricular myocytes. The Journal of Physiology 497, 337–347. https://doi.org/10.1113/jphysiol.1996.sp021772

Kalecky, K., Modisette, R., Pena, S., Cho, Y.-R., Taube, J., 2020. Integrative analysis of breast cancer profiles in TCGA by TNBC subgrouping reveals novel microRNA-specific clusters, including miR-17-92a, distinguishing basal-like 1 and basal-like 2 TNBC subtypes. BMC Cancer 20, 141. https://doi.org/10.1186/s12885-020-6600-6

Kassambara, A. and Kosinski, M. (2021) survminer: Drawing survival curves using ‘ggplot2’. Version 0.4.9. Available at: https://CRAN.R-project.org/package=survminer

(Accessed: 23 September 2025).

Kim, J., Tchernyshyov, I., Semenza, G.L., Dang, C.V., 2006. HIF-1-mediated expression of pyruvate dehydrogenase kinase: A metabolic switch required for cellular adaptation to hypoxia. Cell Metabolism 3, 177–185. https://doi.org/10.1016/j.cmet.2006.02.002

Kirchhof, P., et al., 2016. 2016 ESC Guidelines for the management of atrial fibrillation developed in collaboration with EACTS. Europace 18, 1609–1678. https://doi.org/10.1093/europace/euw295

Kolde, R., Laur, S., Adler, P., Vilo, J., 2012. Robust rank aggregation for gene list integration and meta-analysis. Bioinformatics 28, 573–580. https://doi.org/10.1093/bioinformatics/btr709

Kuht, H.J., Han, J., Maconachie, G.D.E., Park, S.E., Lee, S.-T., McLean, R., Sheth, V., Hisaund, M., Dawar, B., Sylvius, N., Mahmood, U., Proudlock, F.A., Gottlob, I., Lim, H.T., Thomas, M.G., 2020. SLC38A8 mutations result in arrested retinal development with loss of cone photoreceptor specialization. Human Molecular Genetics 29, 2989–3002. https://doi.org/10.1093/hmg/ddaa166

Lacerda-Abreu, M.A., Russo-Abrahão, T., Monteiro, R.D.Q., Rumjanek, F.D., Meyer-Fernandes, J.R., 2018. Inorganic phosphate transporters in cancer: Functions, molecular mechanisms and possible clinical applications. Biochimica et Biophysica Acta (BBA) - Reviews on Cancer 1870, 291–298. https://doi.org/10.1016/j.bbcan.2018.05.001

Latham, T., Mackay, L., Sproul, D., Karim, M., Culley, J., Harrison, D.J., Hayward, L., Langridge-Smith, P., Gilbert, N., Ramsahoye, B.H., 2012. Lactate, a product of glycolytic metabolism, inhibits histone deacetylase activity and promotes changes in gene expression. Nucleic Acids Research 40, 4794–4803. https://doi.org/10.1093/nar/gks066

Le, A., Lane, A.N., Hamaker, M., Bose, S., Gouw, A., Barbi, J., Tsukamoto, T., Rojas, C.J., Slusher, B.S., Zhang, H., Zimmerman, L.J., Liebler, D.C., Slebos, R.J.C., Lorkiewicz, P.K., Higashi, R.M., Fan, T.W.M., Dang, C.V., 2012. Glucose-Independent Glutamine Metabolism via TCA Cycling for Proliferation and Survival in B Cells. Cell Metabolism 15, 110–121. https://doi.org/10.1016/j.cmet.2011.12.009

Lehmann, B.D., Bauer, J.A., Chen, X., Sanders, M.E., Chakravarthy, A.B., Shyr, Y., Pietenpol, J.A., 2011. Identification of human triple-negative breast cancer subtypes and

preclinical models for selection of targeted therapies. J. Clin. Invest. 121, 2750–2767. https://doi.org/10.1172/JCI45014

Leslie, T.K., Brackenbury, W.J., 2023. Sodium channels and the ionic microenvironment of breast tumours. The Journal of Physiology 601, 1543–1553. https://doi.org/10.1113/JP282306

Leslie, T.K., Brückner, L., Chawla, S., Brackenbury, W.J., 2020. Inhibitory Effect of Eslicarbazepine Acetate and S-Licarbazepine on Nav1.5 Channels. Front Pharmacol 11, 555047. https://doi.org/10.3389/fphar.2020.555047

Leslie, T.K., James, A.D., Zaccagna, F., Grist, J.T., Deen, S., Kennerley, A., Riemer, F., Kaggie, J.D., Gallagher, F.A., Gilbert, F.J., Brackenbury, W.J., 2019. Sodium homeostasis in the tumour microenvironment. Biochimica et Biophysica Acta (BBA) - Reviews on Cancer 1872, 188304. https://doi.org/10.1016/j.bbcan.2019.07.001

Leslie, T.K., et al., 2023. A novel Na v 1.5-dependent feedback mechanism driving glycolytic acidification in breast cancer metastasis (preprint). Cancer Biology. https://doi.org/10.1101/2023.06.16.545273

Li, J., Chen, Z., Jin, M., Gu, X., Wang, Y., Huang, G., Zhao, W., Lu, C., 2024. Histone H4K12 lactylation promotes malignancy progression in triple-negative breast cancer through SLFN5 downregulation. Cellular Signalling 124, 111468. https://doi.org/10.1016/j.cellsig.2024.111468

Li, W., Köster, J., Xu, H., Chen, C.-H., Xiao, T., Liu, J.S., Brown, M., Liu, X.S., 2015. Quality control, modeling, and visualization of CRISPR screens with MAGeCK-VISPR. Genome Biol 16, 281. https://doi.org/10.1186/s13059-015-0843-6

Lin, N.U., Claus, E., Sohl, J., Razzak, A.R., Arnaout, A., Winer, E.P., 2008. Sites of distant recurrence and clinical outcomes in patients with metastatic triple-negative breast cancer: High incidence of central nervous system metastases. Cancer 113, 2638–2645. https://doi.org/10.1002/cncr.23930

Lisy, K., Peet, D.J., 2008. Turn me on: regulating HIF transcriptional activity. Cell Death Differ 15, 642–649. https://doi.org/10.1038/sj.cdd.4402315

Liu, Y., Xu, W., Li, M., Yang, Y., Sun, D., Chen, Lidian, Li, H., Chen, Lixia, 2023. The regulatory mechanisms and inhibitors of isocitrate dehydrogenase 1 in cancer. Acta Pharmaceutica Sinica B 13, 1438–1466. https://doi.org/10.1016/j.apsb.2022.12.019

Lobbezoo, D.J.A., et al., 2013. Prognosis of metastatic breast cancer subtypes: the hormone receptor/HER2-positive subtype is associated with the most favorable outcome. Breast Cancer Res Treat 141, 507–514. https://doi.org/10.1007/s10549-013-2711-y

Lopez-Charcas, O., Pukkanasut, P., Velu, S.E., Brackenbury, W.J., Hales, T.G., Besson, P., Gomora, J.C., Roger, S., 2021. Pharmacological and nutritional targeting of voltage-gated sodium channels in the treatment of cancers. iScience 24, 102270. https://doi.org/10.1016/j.isci.2021.102270

Lubarski, I., Pihakaski-Maunsbach, K., Karlish, S.J.D., Maunsbach, A.B., Garty, H., 2005. Interaction with the Na,K-ATPase and Tissue Distribution of FXYD5 (Related to Ion Channel). Journal of Biological Chemistry 280, 37717–37724. https://doi.org/10.1074/jbc.M506397200

Lu, C., Ward, P.S., Kapoor, G.S., Rohle, D., Turcan, S., Abdel-Wahab, O., Edwards, C.R., Khanin, R., Figueroa, M.E., Melnick, A., Wellen, K.E., O'Rourke, D.M., Berger, S.L., Chan, T.A., Levine, R.L., Mellinghoff, I.K., Thompson, C.B., 2012. IDH mutation impairs histone demethylation and results in a block to cell differentiation. Nature 483, 474–478. https://doi.org/10.1038/nature10860

Lundgren, K., Holm, C., Landberg, G., 2007. Common Molecular Mechanisms of Mammary Gland Development and Breast Cancer: Hypoxia and breast cancer: prognostic and therapeutic implications. Cell. Mol. Life Sci. 64, 3233–3247. https://doi.org/10.1007/s00018-007-7390-6

Marino, M.A., Helbich, T., Baltzer, P., Pinker-Domenig, K., 2018. Multiparametric MRI of the breast: A review. Magnetic Resonance Imaging 47, 301–315. https://doi.org/10.1002/jmri.25790

McLeod, A.A., Stiles, G.L., Shand, D.G., 1984. Demonstration of beta adrenoceptor blockade by propafenone hydrochloride: clinical pharmacologic, radioligand binding and adenylate cyclase activation studies. J Pharmacol Exp Ther 228, 461–466.

Menendez, J.A., Lupu, R., 2007. Fatty acid synthase and the lipogenic phenotype in cancer pathogenesis. Nat Rev Cancer 7, 763–777. https://doi.org/10.1038/nrc2222

Metallo, C.M., Gameiro, P.A., Bell, E.L., Mattaini, K.R., Yang, J., Hiller, K., Jewell, C.M., Johnson, Z.R., Irvine, D.J., Guarente, L., Kelleher, J.K., Vander Heiden, M.G., Iliopoulos, O., Stephanopoulos, G., 2012. Reductive glutamine metabolism by IDH1 mediates lipogenesis under hypoxia. Nature 481, 380–384. https://doi.org/10.1038/nature10602

Messier, T.L., Gordon, J.A.R., Boyd, J.R., Tye, C.E., Browne, G., Stein, J.L., Lian, J.B., Stein, G.S., 2016. Histone H3 lysine 4 acetylation and methylation dynamics define breast cancer subtypes. Oncotarget 7, 5094–5109. https://doi.org/10.18632/oncotarget.6922

Mittendorf, E.A., et al., 2014. PD-L1 Expression in Triple-Negative Breast Cancer. Cancer Immunology Research 2, 361–370. https://doi.org/10.1158/2326-6066.CIR-13-0127

Monteith, G.R., Prevarskaya, N., Roberts-Thomson, S.J., 2017. The calcium–cancer signalling nexus. Nat Rev Cancer 17, 373–380. https://doi.org/10.1038/nrc.2017.18

Morotti, M., Bridges, E., Valli, A., Choudhry, H., Sheldon, H., Wigfield, S., Gray, N., Zois, C.E., Grimm, F., Jones, D., Teoh, E.J., Cheng, W.-C., Lord, S., Anastasiou, D., Haider, S., McIntyre, A., Goberdhan, D.C.I., Buffa, F., Harris, A.L., 2019. Hypoxia-induced switch in SNAT2/SLC38A2 regulation generates endocrine resistance in breast cancer. Proc. Natl. Acad. Sci. U.S.A. 116, 12452–12461. https://doi.org/10.1073/pnas.1818521116

Morris, G.J., et al., 2007. Differences in breast carcinoma characteristics in newly diagnosed African–American and Caucasian patients: A single-institution compilation compared with the National Cancer Institute's Surveillance, Epidemiology, and end results database. Cancer 110, 876–884. https://doi.org/10.1002/cncr.22836

Müller, A., Homey, B., Soto, H., Ge, N., Catron, D., Buchanan, M.E., McClanahan, T., Murphy, E., Yuan, W., Wagner, S.N., Barrera, J.L., Mohar, A., Verástegui, E., Zlotnik, A., 2001. Involvement of chemokine receptors in breast cancer metastasis. Nature 410, 50–56. https://doi.org/10.1038/35065016

Nakanishi, T., Kekuda, R., Fei, Y.-J., Hatanaka, T., Sugawara, M., Martindale, R.G., Leibach, F.H., Prasad, P.D., Ganapathy, V., 2001a. Cloning and functional characterization

of a new subtype of the amino acid transport system N. American Journal of Physiology-Cell Physiology 281, C1757–C1768. https://doi.org/10.1152/ajpcell.2001.281.6.C1757

Nakanishi, T., Sugawara, M., Huang, W., Martindale, R.G., Leibach, F.H., Ganapathy, M.E., Prasad, P.D., Ganapathy, V., 2001b. Structure, Function, and Tissue Expression Pattern of Human SN2, a Subtype of the Amino Acid Transport System N. Biochemical and Biophysical Research Communications 281, 1343–1348. https://doi.org/10.1006/bbrc.2001.4504

Nanda, R., et al., 2016. Pembrolizumab in Patients With Advanced Triple-Negative Breast Cancer: Phase Ib KEYNOTE-012 Study. JCO 34, 2460–2467. https://doi.org/10.1200/JCO.2015.64.8931

Nelson, M., Yang, M., Dowle, A.A., Thomas, J.R., Brackenbury, W.J., 2015. The sodium channel-blocking antiepileptic drug phenytoin inhibits breast tumour growth and metastasis. Mol Cancer 14, 13. https://doi.org/10.1186/s12943-014-0277-x

Nelson, M., Yang, M., Millican-Slater, R., Brackenbury, W.J., 2015. Nav1.5 regulates breast tumor growth and metastatic dissemination in vivo. Oncotarget 6, 32914–32929. https://doi.org/10.18632/oncotarget.5441

Nishimura, M., Naito, S., 2008. Tissue-specific mRNA Expression Profiles of Human Solute Carrier Transporter Superfamilies. Drug Metabolism and Pharmacokinetics 23, 22–44. https://doi.org/10.2133/dmpk.23.22

Nishimura, M., Naito, S., 2008. Tissue-specific mRNA Expression Profiles of Human Solute Carrier Transporter Superfamilies. Drug Metabolism and Pharmacokinetics 23, 22–44. https://doi.org/10.2133/dmpk.23.22

Nyblom, M., Poulsen, H., Gourdon, P., Reinhard, L., Andersson, M., Lindahl, E., Fedosova, N., Nissen, P., 2013. Crystal Structure of Na+ , K+ -ATPase in the Na+ -Bound State. Science 342, 123–127. https://doi.org/10.1126/science.1243352

O'Leary, B., Finn, R.S., Turner, N.C., 2016. Treating cancer with selective CDK4/6 inhibitors. Nat Rev Clin Oncol 13, 417–430. https://doi.org/10.1038/nrclinonc.2016.26

Ouwerkerk, R., Bleich, K.B., Gillen, J.S., Pomper, M.G., Bottomley, P.A., 2003. Tissue Sodium Concentration in Human Brain Tumors as Measured with 23 Na MR Imaging. Radiology 227, 529–537. https://doi.org/10.1148/radiol.2272020483

Ouwerkerk, R., Jacobs, M.A., Macura, K.J., Wolff, A.C., Stearns, V., Mezban, S.D., Khouri, N.F., Bluemke, D.A., Bottomley, P.A., 2007. Elevated tissue sodium concentration in malignant breast lesions detected with non-invasive 23Na MRI. Breast Cancer Res Treat 106, 151–160. https://doi.org/10.1007/s10549-006-9485-4

Pajor, A.M., 2014. Sodium-coupled dicarboxylate and citrate transporters from the SLC13 family. Pflugers Arch - Eur J Physiol 466, 119–130. https://doi.org/10.1007/s00424-013-1369-y

Pandkar, M.R., Sinha, S., Samaiya, A., Shukla, S., 2023. Oncometabolite lactate enhances breast cancer progression by orchestrating histone lactylation-dependent c-Myc expression. Translational Oncology 37, 101758. https://doi.org/10.1016/j.tranon.2023.101758

Papoutsis, A.J., Borg, J.L., Selmin, O.I., Romagnolo, D.F., 2012. BRCA-1 promoter hypermethylation and silencing induced by the aromatic hydrocarbon receptor-ligand TCDD are prevented by resveratrol in MCF-7 Cells. The Journal of Nutritional Biochemistry 23, 1324–1332. https://doi.org/10.1016/j.jnutbio.2011.08.001

Pardee, A.B., 1989. G1 Events and Regulation of Cell Proliferation. Science 246, 603–608. https://doi.org/10.1126/science.2683075

Pardo, L.A., Stühmer, W., 2014. The roles of K+ channels in cancer. Nat Rev Cancer 14, 39–48. https://doi.org/10.1038/nrc3635

Pardoll, D.M., 2012. The blockade of immune checkpoints in cancer immunotherapy. Nat Rev Cancer 12, 252–264. https://doi.org/10.1038/nrc3239

Park, B.-S., Jeon, H., Chi, S.-G., Kim, T., 2023. Efficient prioritization of CRISPR screen hits by accounting for targeting efficiency of guide RNA. BMC Biol 21, 45. https://doi.org/10.1186/s12915-023-01536-y

Parker, J.S., et al., 2009. Supervised Risk Predictor of Breast Cancer Based on Intrinsic Subtypes. JCO 27, 1160–1167. https://doi.org/10.1200/JCO.2008.18.1370

Patel, S.A., Simon, M.C., 2008. Biology of hypoxia-inducible factor-2α in development and disease. Cell Death Differ 15, 628–634. https://doi.org/10.1038/cdd.2008.17

Perou, C.M., et al., 2000. Molecular portraits of human breast tumours. Nature 406, 747–752. https://doi.org/10.1038/35021093

Pervaiz, M., Mishra, P., Günther, S., 2018. Bromodomain Drug Discovery – the Past, the Present, and the Future. The Chemical Record 18, 1808–1817. https://doi.org/10.1002/tcr.201800074

Pillai, S.R., Damaghi, M., Marunaka, Y., Spugnini, E.P., Fais, S., Gillies, R.J., 2019. Causes, consequences, and therapy of tumors acidosis. Cancer Metastasis Rev 38, 205–222. https://doi.org/10.1007/s10555-019-09792-7

Plant, H.G., Lietz, H., Weymann, J., 1984. Studies on the metabolism of propafenone. 2nd comm.: studies on the biotransformation in the dog. Arzneimittelforschung 34, 972–979.

Plant, L.D., Xiong, D., Romero, J., Dai, H., Goldstein, S.A.N., 2020. Hypoxia Produces Pro-arrhythmic Late Sodium Current in Cardiac Myocytes by SUMOylation of NaV1.5 Channels. Cell Reports 30, 2225-2236.e4. https://doi.org/10.1016/j.celrep.2020.01.025

Plunkett-Jones, C., 2023. Characterising the effect of sodium channel inhibitors on viability and intracellular sodium content in triple-negative breast cancer cells. MSc by Research thesis. University of York.

Porterfield, J.G., Porterfield, L.M., 1989. Therapeutic efficacy and safety of oral propafenone for atrial fibrillation. The American Journal of Cardiology 63, 114–116. https://doi.org/10.1016/0002-9149(89)91091-6

Posit team (2023) RStudio: Integrated Development Environment for R. Boston, MA: Posit Software. Available at: https://posit.co
(Accessed: 23 September 2025).

Qiao, M., Sheng, S., Pardee, A.B., 2008. Metastasis and AKT activation. Cell Cycle 7, 2991–2996. https://doi.org/10.4161/cc.7.19.6784

Rangel, L.B.A., Sherman-Baust, C.A., Wernyj, R.P., Schwartz, D.R., Cho, K.R., Morin, P.J., 2003. Characterization of novel human ovarian cancer-specific transcripts (HOSTs) identified by serial analysis of gene expression. Oncogene 22, 7225–7232. https://doi.org/10.1038/sj.onc.1207008

R Core Team (2023) grid: The grid graphics package. Included in R version 4.3.0. Vienna: R Foundation for Statistical Computing.

R Core Team (2023) R: A language and environment for statistical computing. Vienna: R Foundation for Statistical Computing. Available at: https://www.R-project.org/ (Accessed: 23 September 2025)

Rocca, A., Schirone, A., Maltoni, R., Bravaccini, S., Cecconetto, L., Farolfi, A., Bronte, G., Andreis, D., 2017. Progress with palbociclib in breast cancer: latest evidence and clinical considerations. Ther Adv Med Oncol 9, 83–105. https://doi.org/10.1177/1758834016677961

Roger, S., Besson, P., Le Guennec, J.-Y., 2003. Involvement of a novel fast inward sodium current in the invasion capacity of a breast cancer cell line. Biochimica et Biophysica Acta (BBA) - Biomembranes 1616, 107–111. https://doi.org/10.1016/j.bbamem.2003.07.001

Sabbagh, Y., O'Brien, S.P., Song, W., Boulanger, J.H., Stockmann, A., Arbeeny, C., Schiavi, S.C., 2009. Intestinal Npt2b Plays a Major Role in Phosphate Absorption and Homeostasis. Journal of the American Society of Nephrology 20, 2348–2358. https://doi.org/10.1681/ASN.2009050559

Saleh, L., Wilson, C., Holen, I., 2021. CDK4/6 inhibitors: A potential therapeutic approach for triple negative breast cancer. MedComm 2, 514–530. https://doi.org/10.1002/mco2.97

Saman, H., Raza, S.S., Uddin, S., Rasul, K., 2020. Inducing Angiogenesis, a Key Step in Cancer Vascularization, and Treatment Approaches. Cancers 12, 1172. https://doi.org/10.3390/cancers12051172

Samanta, A., Hughes, T.E.T., Moiseenkova-Bell, V.Y., 2018. Transient Receptor Potential (TRP) Channels, in: Harris, J.R., Boekema, E.J. (Eds.), Membrane Protein Complexes: Structure and Function, Subcellular Biochemistry. Springer Singapore, Singapore, pp. 141–165. https://doi.org/10.1007/978-981-10-7757-9_6

Samanta, A., Hughes, T.E.T., Moiseenkova-Bell, V.Y., 2018. Transient Receptor Potential (TRP) Channels, in: Harris, J.R., Boekema, E.J. (Eds.), Membrane Protein Complexes: Structure and Function, Subcellular Biochemistry. Springer Singapore, Singapore, pp. 141–165. https://doi.org/10.1007/978-981-10-7757-9_6

San-Millán, I., Julian, C.G., Matarazzo, C., Martinez, J., Brooks, G.A., 2020. Is Lactate an Oncometabolite? Evidence Supporting a Role for Lactate in the Regulation of Transcriptional Activity of Cancer-Related Genes in MCF7 Breast Cancer Cells. Front. Oncol. 9, 1536. https://doi.org/10.3389/fonc.2019.01536

Sanson, K.R., Hanna, R.E., Hegde, M., Donovan, K.F., Strand, C., Sullender, M.E., Vaimberg, E.W., Goodale, A., Root, D.E., Piccioni, F., Doench, J.G., 2018a. Optimized libraries for CRISPR-Cas9 genetic screens with multiple modalities. Nat Commun 9, 5416. https://doi.org/10.1038/s41467-018-07901-8

Sanson, K.R., Hanna, R.E., Hegde, M., Donovan, K.F., Strand, C., Sullender, M.E., Vaimberg, E.W., Goodale, A., Root, D.E., Piccioni, F., Doench, J.G., 2018b. Optimized libraries for CRISPR-Cas9 genetic screens with multiple modalities. Nat Commun 9, 5416. https://doi.org/10.1038/s41467-018-07901-8

Sanvicente-García M, García-Valiente A, Jouide S, Jaraba-Wallace J, Bautista E, Escobosa M, et al., 2023. CRISPR-Analytics (CRISPR-A): A platform for precise analytics and simulations for gene editing. PLoS Comput Biol 19(5): e1011137. https://doi.org/10.1371/journal.pcbi.1011137

Segawa, H., Kaneko, I., Takahashi, A., Kuwahata, M., Ito, M., Ohkido, I., Tatsumi, S., Miyamoto, K., 2002. Growth-related Renal Type II Na/Pi Cotransporter. Journal of Biological Chemistry 277, 19665–19672. https://doi.org/10.1074/jbc.M200943200

Seki, A., Hagiwara, N., Kasanuki, H., 1999. Effects of propafenone on K currents in human atrial myocytes. British J Pharmacology 126, 1153–1162. https://doi.org/10.1038/sj.bjp.0702428

Semenza, G.L., 2003. Targeting HIF-1 for cancer therapy. Nat Rev Cancer 3, 721–732. https://doi.org/10.1038/nrc1187

Semenza, G.L., 2007. Hypoxia-Inducible Factor 1 (HIF-1) Pathway. Sci. STKE 2007. https://doi.org/10.1126/stke.4072007cm8

Semenza, G.L., 2016. The hypoxic tumor microenvironment: A driving force for breast cancer progression. Biochimica et Biophysica Acta (BBA) - Molecular Cell Research 1863, 382–391. https://doi.org/10.1016/j.bbamcr.2015.05.036

Shimoda, L.A., Fallon, M., Pisarcik, S., Wang, J., Semenza, G.L., 2006. HIF-1 regulates hypoxic induction of NHE1 expression and alkalinization of intracellular pH in pulmonary arterial myocytes. Am J Physiol Lung Cell Mol Physiol 291, L941-949. https://doi.org/10.1152/ajplung.00528.2005

Slawsky, M.T., Castle, N.A., 1994. K+ channel blocking actions of flecainide compared with those of propafenone and quinidine in adult rat ventricular myocytes. J Pharmacol Exp Ther 269, 66–74.

Slowikowski, K. (2023) ggrepel: Automatically position non-overlapping text labels with 'ggplot2'. Version 0.9.3. Available at: https://CRAN.R-project.org/package=ggrepel (Accessed: 23 September 2025).

Srivastava, N., Usmani, S.S., Subbarayan, R., Saini, R., Pandey, P.K., 2023. Hypoxia: syndicating triple negative breast cancer against various therapeutic regimens. Front. Oncol. 13, 1199105. https://doi.org/10.3389/fonc.2023.1199105

Stanton, S.E., Adams, S., Disis, M.L., 2016. Variation in the Incidence and Magnitude of Tumor-Infiltrating Lymphocytes in Breast Cancer Subtypes: A Systematic Review. JAMA Oncol 2, 1354. https://doi.org/10.1001/jamaoncol.2016.1061

Steurer, G., Weber, H., Schmidinger, H., Plass, H., Frey, B., Pürerfellner, H., Probst, P., 1991. Plasma propafenone concentration in the evaluation of anti-arrhythmic efficacy. European Heart Journal 12, 526–532. https://doi.org/10.1093/oxfordjournals.eurheartj.a059934

Steward, L., Conant, L., Gao, F., Margenthaler, J.A., 2014. Predictive Factors and Patterns of Recurrence in Patients with Triple Negative Breast Cancer. Ann Surg Oncol 21, 2165–2171. https://doi.org/10.1245/s10434-014-3546-4

Sucher, N., Akbarian, S., Chi, C., Leclerc, C., Awobuluyi, M., Deitcher, D., Wu, M., Yuan, J., Jones, E., Lipton, S., 1995. Developmental and regional expression pattern of a novel NMDA receptor- like subunit (NMDAR-L) in the rodent brain. J. Neurosci. 15, 6509–6520. https://doi.org/10.1523/JNEUROSCI.15-10-06509.1995

Sundberg, B.E., Wååg, E., Jacobsson, J.A., Stephansson, O., Rumaks, J., Svirskis, S., Alsiö, J., Roman, E., Ebendal, T., Klusa, V., Fredriksson, R., 2008. The Evolutionary History and Tissue Mapping of Amino Acid Transporters Belonging to Solute Carrier Families SLC32, SLC36, and SLC38. J Mol Neurosci 35, 179–193. https://doi.org/10.1007/s12031-008-9046-x

Takatani-Nakase, T., Matsui, C., Hosotani, M., Omura, M., Takahashi, K., Nakase, I., 2022. Hypoxia enhances motility and EMT through the Na+/H+ exchanger NHE-1 in MDA-MB-231 breast cancer cells. Experimental Cell Research 412, 113006. https://doi.org/10.1016/j.yexcr.2021.113006

Thakur, C., Qiu, Y., Fu, Y., Bi, Z., Zhang, W., Ji, H., Chen, F., 2022. Epigenetics and environment in breast cancer: New paradigms for anti-cancer therapies. Front. Oncol. 12, 971288. https://doi.org/10.3389/fonc.2022.971288

Therneau, T.M. (2023) A package for survival analysis in R. Version 3.5-7. Available at: https://CRAN.R-project.org/package=survival
(Accessed: 23 September 2025).

Thorén, M.M., Vaapil, M., Staaf, J., Planck, M., Johansson, M.E., Mohlin, S., Påhlman, S., 2017. Myc-induced glutaminolysis bypasses HIF-driven glycolysis in hypoxic small cell lung carcinoma cells. Oncotarget 8, 48983–48995. https://doi.org/10.18632/oncotarget.16904

Tian, Y., Du, W., Cao, S., Wu, Y., Dong, N., Wang, Y., Xu, Y., 2017. Systematic analyses of glutamine and glutamate metabolisms across different cancer types. Chin J Cancer 36, 88. https://doi.org/10.1186/s40880-017-0255-y

Tripathi, R., Aggarwal, T., Fredriksson, R., 2021. SLC38A10 Transporter Plays a Role in Cell Survival Under Oxidative Stress and Glutamate Toxicity. Front. Mol. Biosci. 8, 671865. https://doi.org/10.3389/fmolb.2021.671865

Tsai, P.-J., Lai, Y.-H., Manne, R.K., Tsai, Y.-S., Sarbassov, D., Lin, H.-K., 2022. Akt: a key transducer in cancer. J Biomed Sci 29, 76. https://doi.org/10.1186/s12929-022-00860-9

Tsung, K., Liu, K.Q., Han, J.S., Deshpande, K., Doan, T., Loh, Y.-H.E., Ding, L., Yang, W., Neman, J., Dou, Y., Attenello, F.J., 2024. CRISPRi screen of long non-coding RNAs identifies LINC03045 regulating glioblastoma invasion. PLoS Genet 20, e1011314. https://doi.org/10.1371/journal.pgen.1011314

Turner, N.C., et al., 2018. Overall Survival with Palbociclib and Fulvestrant in Advanced Breast Cancer. N Engl J Med 379, 1926–1936. https://doi.org/10.1056/NEJMoa1810527

Uphoff, C.C., Gignac, S.M., Drexler, H.G., 1992. Mycoplasma contamination in human leukemia cell lines. Journal of Immunological Methods 149, 43–53. https://doi.org/10.1016/S0022-1759(12)80047-0

Usluer, S., Hallast, P., Crepaldi, L., Zhou, Y., Urgo, K., Dincer, C., Su, J., Noell, G., Alasoo, K., El Garwany, O., Gerety, S.S., Newman, B., Dovey, O.M., Parts, L., 2023. Optimized whole-genome CRISPR interference screens identify ARID1A-dependent growth regulators in human induced pluripotent stem cells. Stem Cell Reports 18, 1061–1074. https://doi.org/10.1016/j.stemcr.2023.03.008

Wagner, J., et al., 2019. A Single-Cell Atlas of the Tumor and Immune Ecosystem of Human Breast Cancer. Cell 177, 1330-1345.e18. https://doi.org/10.1016/j.cell.2019.03.005

Walmsley, S.R., Print, C., Farahi, N., Peyssonnaux, C., Johnson, R.S., Cramer, T., Sobolewski, A., Condliffe, A.M., Cowburn, A.S., Johnson, N., Chilvers, E.R., 2005. Hypoxia-induced neutrophil survival is mediated by HIF-1α–dependent NF-κB activity. The Journal of Experimental Medicine 201, 105–115. https://doi.org/10.1084/jem.20040624

Wang, D., King, S.M., Quill, T.A., Doolittle, L.K., Garbers, D.L., 2003. A new sperm-specific Na+/H+ Exchanger required for sperm motility and fertility. Nat Cell Biol 5, 1117–1122. https://doi.org/10.1038/ncb1072

Wang, G.L., Jiang, B.H., Rue, E.A., Semenza, G.L., 1995. Hypoxia-inducible factor 1 is a basic-helix-loop-helix-PAS heterodimer regulated by cellular O2 tension. Proc. Natl. Acad. Sci. U.S.A. 92, 5510–5514. https://doi.org/10.1073/pnas.92.12.5510

Warburg, O., 1956. On the Origin of Cancer Cells. Science 123, 309–314. https://doi.org/10.1126/science.123.3191.309

Webb, B.A., Chimenti, M., Jacobson, M.P., Barber, D.L., 2011. Dysregulated pH: a perfect storm for cancer progression. Nat Rev Cancer 11, 671–677. https://doi.org/10.1038/nrc3110

Weber, S.L.K., Heinzel, T., Iyer-Bierhoff, A., 2025. Protocol for ecotropic pseudotyped lentiviral transduction of “murinized” human cells while decreasing risk of infection for laboratory personnel. STAR Protocols 6, 103708. https://doi.org/10.1016/j.xpro.2025.103708

Wei, Y., An, X., Cao, Q., Che, N., Xue, Y., Deng, H., Wang, Q., Zhou, R., 2022. Lentiviral vector–based xenograft tumors as candidate reference materials for detection of HER2-low breast cancer. Front. Oncol. 12, 955943. https://doi.org/10.3389/fonc.2022.955943

Wenger, R.H., Kvietiko, I., Rolfs, A., Gassmann, M., Marti, H.H., 1997. Hypoxia-inducible factor-1α is regulated at the post-mRNA level. Kidney International 51, 560–563. https://doi.org/10.1038/ki.1997.79

West, N.R., et al., 2011. Tumor-infiltrating lymphocytes predict response to anthracycline-based chemotherapy in estrogen receptor-negative breast cancer. Breast Cancer Res 13, R126. https://doi.org/10.1186/bcr3072

Wickham, H., 2016. ggplot2, Use R! Springer International Publishing, Cham. https://doi.org/10.1007/978-3-319-24277-4

Wickham, H. and Girlich, M. (2023) tidyr: Tidy messy data. Version 1.3.0. Available at: https://CRAN.R-project.org/package=tidyr
(Accessed: 23 September 2025).

Wickham, H., François, R., Henry, L. and Müller, K. (2023) dplyr: A grammar of data manipulation. Version 1.1.2. Available at: https://CRAN.R-project.org/package=dplyr
(Accessed: 23 September 2025).

Williams, E.M.V., 1984. A Classification of Antiarrhythmic Actions Reassessed After a Decade of New Drugs. The Journal of Clinical Pharma 24, 129–147. https://doi.org/10.1002/j.1552-4604.1984.tb01822.x

Xu, H., Bai, L., Collins, J.F., Ghishan, F.K., 1999. Molecular Cloning, Functional Characterization, Tissue Distribution, and Chromosomal Localization of a Human, Small Intestinal Sodium–Phosphate (Na+–Pi) Transporter (SLC34A2). Genomics 62, 281–284. https://doi.org/10.1006/geno.1999.6009

Xu, L., Luo, H., Wang, R., Wu, W.W., Phue, J.-N., Shen, R.-F., Juhl, H., Wu, L., Alterovitz, W., Simonyan, V., Pelosof, L., Rosenberg, A.S., 2019. Novel reference genes in colorectal cancer identify a distinct subset of high stage tumors and their associated histologically normal colonic tissues. BMC Med Genet 20, 138. https://doi.org/10.1186/s12881-019-0867-y

Xu, W., Song, C., Wang, X., Li, Y., Bai, X., Liang, X., Wu, J., Liu, J., 2021. Downregulation of miR-155-5p enhances the anti-tumor effect of cetuximab on triple-negative breast cancer cells via inducing cell apoptosis and pyroptosis. Aging 13, 228–240. https://doi.org/10.18632/aging.103669

Yamamoto, T., et al., 2019. Synergistic anti-cancer activity of CDK4/6 inhibitor palbociclib and dual mTOR kinase inhibitor MLN0128 in pRb-expressing ER-negative breast cancer. Breast Cancer Res Treat 174, 615–625. https://doi.org/10.1007/s10549-018-05104-9

Yang, M., James, A.D., Suman, R., Kasprowicz, R., Nelson, M., O'Toole, P.J., Brackenbury, W.J., 2020. Voltage-dependent activation of Rac1 by Na v 1.5 channels promotes cell migration. J Cell Physiol 235, 3950–3972. https://doi.org/10.1002/jcp.29290

Yang, M., Kozminski, D.J., Wold, L.A., Modak, R., Calhoun, J.D., Isom, L.L., Brackenbury, W.J., 2012. Therapeutic potential for phenytoin: targeting Nav1.5 sodium channels to reduce migration and invasion in metastatic breast cancer. Breast Cancer Res Treat 134, 603–615. https://doi.org/10.1007/s10549-012-2102-9

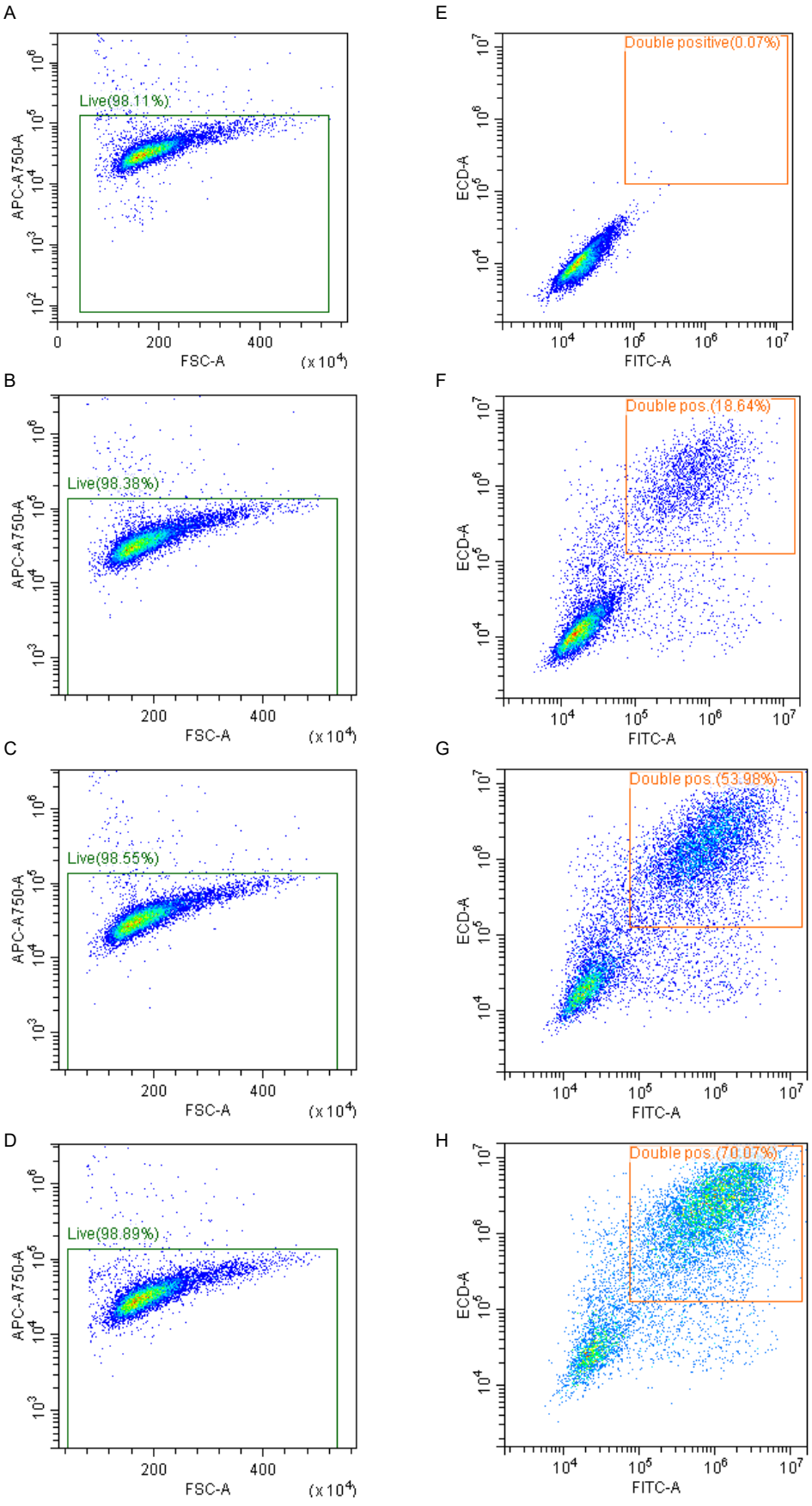
Yoo, H.C., Park, S.J., Nam, M., Kang, J., Kim, K., Yeo, J.H., Kim, J.-K., Heo, Y., Lee, H.S., Lee, M.Y., Lee, C.W., Kang, J.S., Kim, Y.-H., Lee, J., Choi, J., Hwang, G.-S., Bang, S., Han, J.M., 2020. A Variant of SLC1A5 Is a Mitochondrial Glutamine Transporter for Metabolic Reprogramming in Cancer Cells. Cell Metabolism 31, 267-283.e12. https://doi.org/10.1016/j.cmet.2019.11.020

Zhang, C., Moore, L.M., Li, X., Yung, W.K.A., Zhang, W., 2013. IDH1/2 mutations target a key hallmark of cancer by deregulating cellular metabolism in glioma. Neuro-Oncology 15, 1114–1126. https://doi.org/10.1093/neuonc/not087

Zhao, S., Lin, Y., Xu, W., Jiang, W., Zha, Z., Wang, P., Yu, W., Li, Z., Gong, L., Peng, Y., Ding, J., Lei, Q., Guan, K.-L., Xiong, Y., 2009. Glioma-Derived Mutations in IDH1 Dominantly Inhibit IDH1 Catalytic Activity and Induce HIF-1α. Science 324, 261–265. https://doi.org/10.1126/science.1170944

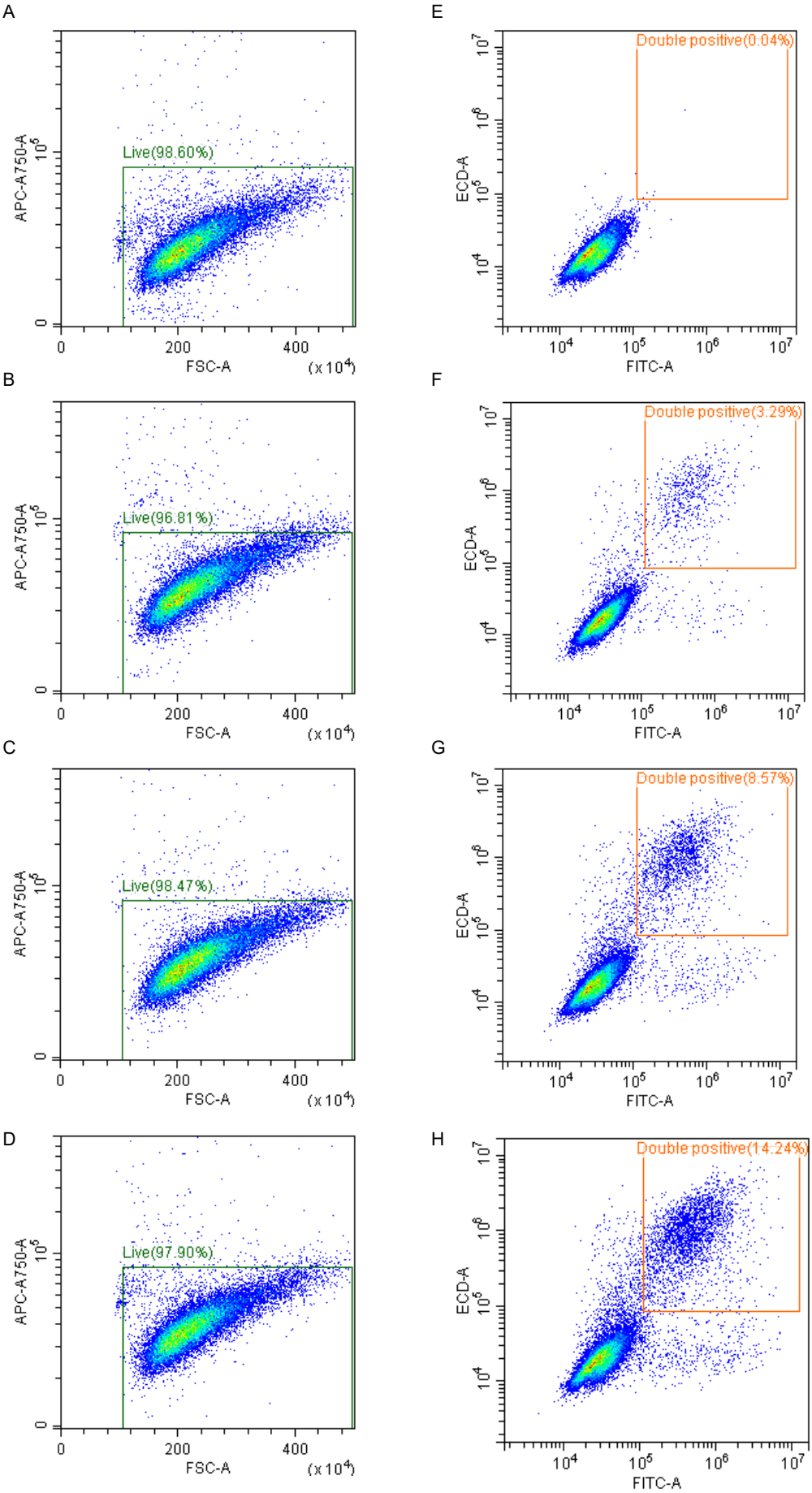
Zhao, W. 2024. Email to Rachael Moore, 24 February 2025. Personal communication.

Supplementary figures


A
Live(98.11%)
APC-A750-A
FSC-A
(x10^4)
B
Live(98.38%)
C
Live(98.55%)
D
Live(98.89%)
E
Double positive(0.07%)
ECD-A
FITC-A
F
Double pos.(18.64%)
G
Double pos.(53.98%)
H
Double pos.(70.07%)

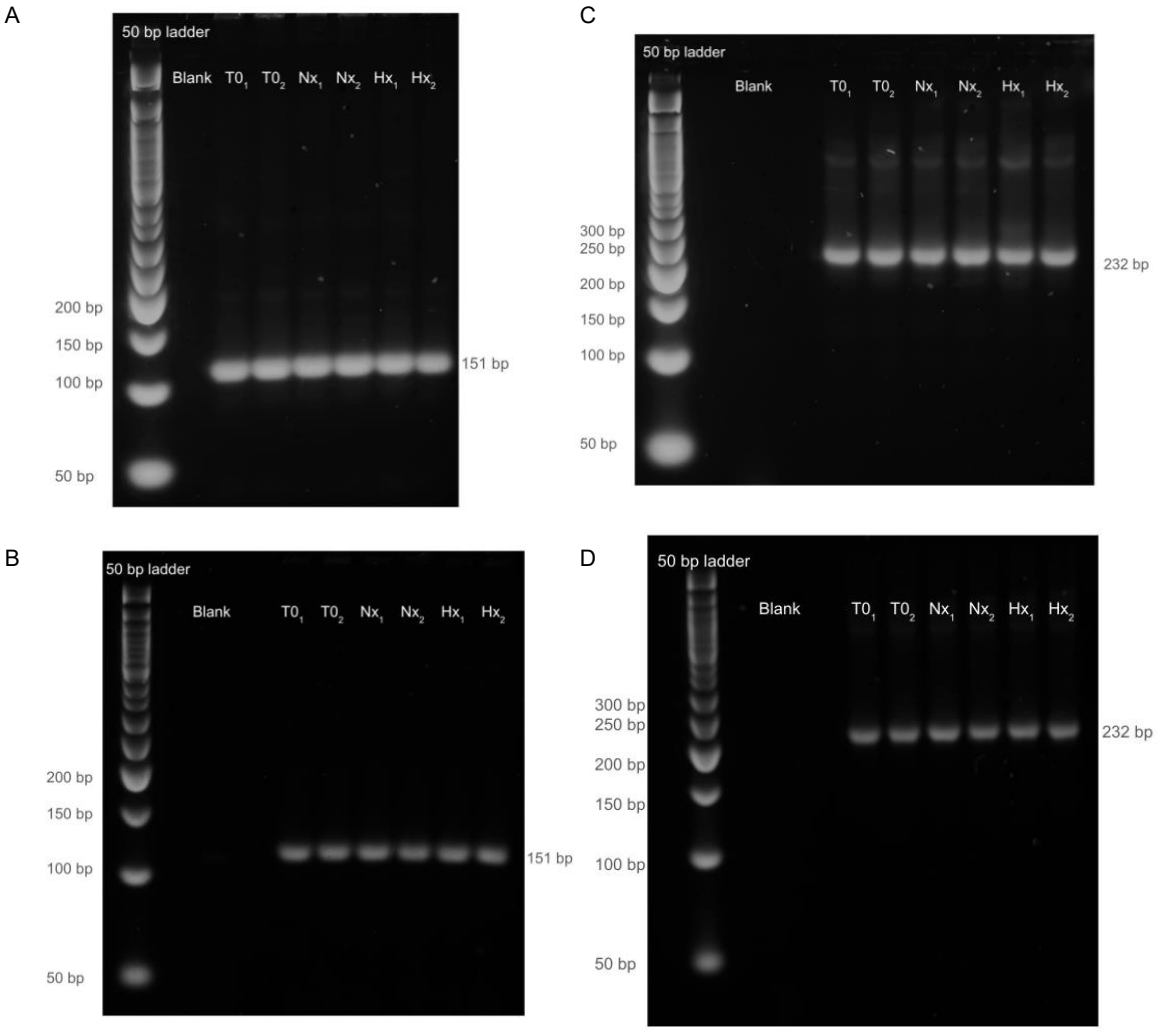
Supplementary Figure 1. Flow Cytometry Analysis of MDA-MB-231 Cells Transduced with eGFP/mCherry Lentivirus.

On day 1, MDA-MB-231 cells were transduced with a control eGFP/mCherry lentivirus at MOIs of 0, 1, 5, and 10. Cells were harvested on day 4 and processed for flow cytometry. Cells were stained with Far Red 638 Fixable Live Dead dye and fixed in 4% PFA. (A-D) Gating strategies were implemented (Fig.s ..). to identify live cells transfected at MOI of (A) 0, (B) 1, (C) 5, and (D) 10. (E-H) Live cells were then plotted on a dot plot where the x-axis represents e-GFP (FITC) intensity, and the y-axis represents mCherry (EDC) intensity. The percentage of cells in the upper right quadrant of the dot plot determined the percentage of live, transfected cells at each MOI; (E) 0, (F) 1, (G) 5, and (H) 10. The selected plots provide a representative snapshot of transduction efficiency at different MOIs (n=1, 3 technical replicates).


A
Live(98.60%)
APC-A750-A
FSC-A
(x10^4)
B
Live(96.81%)
C
Live(98.47%)
D
Live(97.90%)
E
Double positive(0.04%)
ECD-A
FITC-A
F
Double positive(3.29%)
G
Double positive(8.57%)
H
Double positive(14.24%)

Supplementary Figure 2. Flow Cytometry Analysis of MDA-MB-468 Cells Transduced with eGFP/mCherry Lentivirus.

On day 1, MDA-MB-468 cells were transduced with a control eGFP/mCherry lentivirus at MOIs of 0, 1, 3, and 5. Cells were harvested on day 4 and processed for flow cytometry. Cells were stained with Far Red 638 Fixable Live Dead dye and fixed in 4% PFA. (A-D) Gating strategies were implemented (Fig.s ..). to identify live cells transfected at MOI of (A) 0, (B) 1, (C) 3, and (D) 5. (E-H) Live cells were then plotted on a dot plot where the x-axis represents e-GFP (FITC) intensity, and the y-axis represents mCherry (EDC) intensity. The percentage of cells in the upper right quadrant of the dot plot determined the percentage of live, transfected cells at each MOI; (E) 0, (F) 1, (G) 3, and (H) 5. The selected plots provide a representative snapshot of transduction efficiency at different MOIs (n=1, 3 technical replicates).



Supplementary Figure 3. Gel electrophoresis analysis of CRISPRi screen PCR products.

3% agarose gel showing nested PCR products from the CRISPRi screen samples; 50 bp DNA ladder (50 bp ladder), negative control (Blank), T0 replicate 1 ($T0_1$), T0 replicate 2 ($T0_2$), normoxia replicate 1 (Nx_1), normoxia replicate 2 (Nx_2), hypoxia replicate 1 (Hx_1), hypoxia replicate 2 (Hx_2). (A-B) Initial amplification of gRNA cassettes from CRISPRi screen experiments with (A) MDA-MB-231 cells and (B) MDA-MB-468 cells. (C-D) Products of PCR adding illumina adapter sequences to gRNA cassettes in (C) MDA-MB-231 cells and (D) MDA-MB-468 cells. The base pair (bp) value to the right of each panel represents the expected product size.

Supplementary Table 1. Guide RNA library for CRISPRi screen

Gene	*Protein*	*gRNA 1*	*gRNA 2*	*gRNA 3*	*gRNA 4*	*gRNA 5*
ATP1A1	N/K-ATPase subunit alpha 1	ACCAGGGGAGCCAAGTGGA	GAAGGAGCCCCGAACCCGG	ggcggacacgtggcaacag	GAGGGAGCGCAGTAACGGG	acagcggtagcagcccggg
ATP1A2	N/K-ATPase subunit alpha 2	CCAGCCCGTCTGGGACAGT	GGGCTGTGGGTCTAACTGT	AGGGAAGGACTAGAGATGT	AGCCCACACCAGCCCGTCT	GGTCTCCGACTGTCCCAGA
ATP1A3	N/K-ATPase subunit alpha 3	CTCTGTGCGGTGGGACCAA	GGCCGCCGCAGCCTCTGTG	GTGCGGTGGGACCAACGGA	CGGACGCGCGCACCTACCG	GCAGCGCCCGCGCCTCGGT
ATP1A4	N/K-ATPase subunit alpha 4	GAGAAGGGCCCCAAAAGGT	GCAGGGCCAGACAACAGAC	GGCCCCAAAAGGTAGGCCA	TCATACAGGACTGAAGAAA	AGTGTGAGAAGGCTCATAC
ATP1B1	N/K-ATPase subunit beta 1	GACCCTGCGCCCCACTCTG	CCAGGCCGGAGAAGCCGAG	CGCACTCCGAGAGCCGCAG	CCGAGAGCCGCAGCGGCAG	GGAGCCCCCGACCCCCCAA
ATP1B2	N/K-ATPase subunit beta 2	GCAGCTGCATATCTGAGGG	AGGAGCGGAGCCTCCGCCT	GCAGCTGCTGCAGATTCCG	CGCGGGCCTCGCACTGCTG	CTGGGGGGCCCCCCATCCC
ATP1B3	N/K-ATPase subunit beta 3	AGCCCGGAGACGGCAGTGA	CAGGCTCCCGCGGCCCAAg	GACCGCCCGACCCTAACCC	CGGACGGCGAGAGGAGCTG	CGGCCCGGGGAGCAATGAA
FXYD1	Phospholemman	GCAGGCCAACCCAAGAGGG	GGCGGCCCAGCCAGACCAG	ACGTCCTGCTGTGCCCCGG	GCTGTCCCCTGCTGAAAGA	GGGGACGCTCACCCCAATC
FXYD2	N/K-ATPase subunit gamma	GCCTAGGAAGGCTGACCAG	GGTCCAGCTGACCCCACAA	GTCATTTCCCCAGGTGAAT	CTGGGTTGTCGATGGACGG	TGACTGGGTTGTCGATGGA
FXYD3		TGACCAAAGTCAGGAGATG	AGAGGTTCCGGGAGAAATC	TCTGGAGCCAGGAGATAAA	GGGGTGCCTGGGTAGGTAG	TAATTTAGGGGCAGAGACA

Gene	*Protein*	*gRNA 1*	*gRNA 2*	*gRNA 3*	*gRNA 4*	*gRNA 5*
FXYD4		AGCGCAGAGAACGGATCTG	TGGAGTTCCTGGAATACGA	ATACGAGGGTCTCAACTCT	AGGAGGCTGCTGGGCACGT	GGCGAGGGCTCACCTGAGC
FXYD5		CGGCAGCCTCGTGGAGAGA	CGTGGAGAGAGGGACGCGG	CTGGGGCAGAGGAGTAGAT	GCACGAGAGGGACTTACGT	GCCCACTGTAGCCCAGGAG
FXYD6		CCCCTCCGAGACTCCCAGG	CTCCTCATGGATAAAGGGT	GTCCTCCTGGGAGTCTCGG	GATCGGCGTCGGAAGAGAG	GGACTCGGCGGGTCCTCCT
FXYD7		ACCGTGGTGGTAGCAGACG	GGAGGTCCGCTCCTCCTGT	GTGTCCCAGAGACCCGGAG	GGCTGGTCCCGCACCGTGG	GGAGAAGGGATGCTCGGAC
SCN1A	$Na_v1.1$ alpha subunit	AATGTGCAGGATGACAAGA	TGAAGAAGTTGAAGCTGTC	TTGGTGCTACAACAGTCCA	TTCACCAGAGAATCTCTTG	CACCATGACAAATAAAAAG
SCN2A	Na_v 1.2 alpha subunit	GAACAGAAAGCTAAGGCAA	CAAAGGAGGGAGGATGCTG	TGTTCTGACAGTCATTCGA	AGCTGTTGGTCTCTGTCTC	GGTAAAGCTTTCAAAGTGA
SCN3A	$Na_v1.3$ alpha subunit	ATCTCAGAACAGGAAGCGG	TGTAAATTACAGGAACCAA	ACCTGGTAGCTAGGTTCTA	ATAGAGTGAATCTCAGAAC	AATAGAGCCTGTCTGGAAA
SCN4A	Na_v 1.4 alpha subunit	GGCTCAGAGACCAGAAGGG	TACGATGAAGGTCTAAGGT	CTGGCCATCCTCGCATCCT	TGAGTACGATGAAGGTCTA	CCTTCATCGTACTCAACAA
SCN5A	$Na_v1.5$ alpha subunit	AGCCGCGGAGCCGAGACGG	GGGAGCCCGAACAGAGCCG	GACAGCGCACCGGGAAACC	TGCAGGGATCGCTCCCCCG	GCGCACCGGGAAACCCGGA
SCN8A	$Na_v1.6$ alpha subunit	AGGCGCGGCCGGACTGCAA	GCCGCCGGGAGCGGATCAG	GCGAGAAGGGAAACCCGGA	TGCAAAGGCGCCGAGGATG	GAGGGCTGCACCGCGGAAG

Gene	*Protein*	*gRNA 1*	*gRNA 2*	*gRNA 3*	*gRNA 4*	*gRNA 5*
SCN9A	$Na_v1.7$ alpha subunit	GCGGTCGCCAGCGCTCCAG	CCACCTGGAAAGAAGAGAG	GTCGCCAGCGCTCCAGCGG	CCAGCAATGGGAGGAAGAA	TTCCAGGTGGCGTAATACA
SCN10A	$Na_v1.8$ alpha subunit	TGACTCCGGAGTAAAGCGA	GGAGCTCACCATAGAACTT	ACGGATCTAGATCCTCCAG	CCGGGTAAGAGCTACTAGT	CCCGGTGTGTGCTGTAGAA
SCN11A	$Na_v1.9$ alpha subunit	ATGGGTCCAAGTCTTCCAG	GTTCCTGCTATACCCACAG	CCAGAGAGTCGGAAGTGAA	CCTGCTATACCCACAGTGG	GGAAAGCCTCTGGAAGACT
SCN1B	Sodium channel subunit beta-1	tgcAGTGCGCAGGAGACCG	CCGAGCCGGAGCGGGACCG	CCGGGGTCGGTGCACCTAG	GCGCCGCGCAGCCATGGGG	GAGCGCGCCCGAGCCGGAG
SCN2B	Sodium channel subunit beta-2	agagagagggagtgtgtaa	CTGTGACTAAGTAGTCCCA	GCCGGCCATATTAGAGAGA	CCCTCTGTGTCCTTGGGAG	AAAGAGACTGAGCCCCGTG
SCN3B	Sodium channel subunit beta-3	GAGCCGCCTGCGCATGTCA	GCGCAAACGAGCGAGGCAG	GACAGCACACACGGCCTGG	ATCACCTGCCACCCAGGGT	CCCTGGGCGCAAACGAGCG
SCN4B	Sodium channel subunit beta-4	TGAGACTGGCGGGCTGATG	CGCGCTCTCCGCCCGAGGT	GTCGCGGGGATGGGATACT	TTTCCCGAGCCCCGACCGG	GCGGGTCTCCAGAGTTCAG
SCNN1A	ENaC-alpha	CAGAGGAGAGGCCGTTCTA	CCAGCCGCAACCTGGGAGT	TTCTAGGGAAGCCCAGCTC	CCTGGAGCCAGCAGACCTG	TCGAAAGGTGGCCCTATCA
SCNN1B	ENaC-beta	GGATGCGCGCTGTCGGCGG	GGTCCCAGGCGCCTCAGAC	AGAGACGGCGGCAAAGTCC	GAGCGCGGCGAGACCGACT	TGCGCGCTGTCGGCGGTGG

Gene	*Protein*	*gRNA 1*	*gRNA 2*	*gRNA 3*	*gRNA 4*	*gRNA 5*
SCNN1G	ENaC-gamma	AGGGTAGAAGGAACAGTAG	AAGGGTCCAAGGCTCGTGC	CCACGGCGTGGGTAGACCC	CTCTCGGGCTAGCATCCCC	GGCCCACAAGAGCCCGCGG
ASIC1	acid-sensing ion channel subunit 1	TCCAGAGGGAGGAGAGTCC	CGGCTCCGGGACTGGAGAG	GATCCATCGTCCGGCCGGG	CAGCCGGCGGCGGGTCCTG	TCAGCGCCGAGTCGCGGAG
ASIC2	acid-sensing ion channel subunit 2	GACCGGTATCTGGAGACTG	GGCGCGGAGAGGCGAGGAC	AGAGGCGAGGACCGGTATC	GGAAGCGGGGAGCTCAGAC	TCTAGTGGCGTGTGTAGGG
ASIC3	acid-sensing ion channel subunit 3	TACGCCAAGGAGCTCTCCA	CGGCTCGGGATCCGCACCA	CGCACCATGGAGAGCTCCT	GCCAGCACGCGCTACGCCA	CGCGATGTAGGCCTCGCTG
ASIC4	acid-sensing ion channel subunit 4	GCTGTGCTGGTGCTGATAA	CCCTCCCGAGTGGCAGTGG	GATGAGCAGAGCCTCCTCG	AGCCACAAGGAGACGATCG	GCCCTGGTGCCCTCCCGAG
ASIC5	acid-sensing ion channel subunit 5	AGTTAAGCAAGAGTCCTCA	TGAAAATTGGGTTACCCTG	CACTGTATATACTCCAGTC	TTGATCAGCACTCAATGCA	TTTGGTTTCTATTTATCCT
GRIN1	GluN1	CGTGAACCAGGCCAACAAG	ccggaaccagcgccgtccg	gacggcgctggttccggtc	gtcgccgcagcgtccggac	ggttccggtccggacgctg
GRIN2A	GluN2A	CCGGCGCGCTCAGAGGACC	TAGCGGGAGCTCCACTCCA	GCCACTGCTGAGAACTATG	CTCGTGGGTGGCCAACCTG	ACGAGCCAGCAGTAGGAGA
GRIN2B	GluN2B	GATTCGCGTGTCCCCCGGA	GATATGCAAGCGAGAAGAA	CTCTAGACGGACAGATTAA	GGGGAAAAAGAGGCGGTCA	GCAAGCGAGAAGAAGGGAC
GRIN2C	GluN2C	CGAGAGCCACCGTCACCCG	GTCCCCGCCCTGCCCGCGT	CTTGAGCCGCGGGTGACGG	GCAGGAAACAGGAGACTCG	GAGGGGCGGCTCACCGGAA

Gene	*Protein*	*gRNA 1*	*gRNA 2*	*gRNA 3*	*gRNA 4*	*gRNA 5*
GRIN 2D	GluN2D	AGCCTGCA GACCCTAT CAG	CTCACCAG AGACAGGA CGT	ACCAGAGA CAGGACGT GGG	AGTCGTAG CCCCAGAC CTC	GTGAGGGA GATGACCA CCA
GRIN 3A	GluN3A	CCTCCGAG GAAGCAAG CGG	GCTCCTCC GAGGAAGC AAG	AGCAGCCG GAGTTCCT CGG	CAGTCGCG TTGCTCCTC CG	AGCTGCGC GCGGGACC TGG
GRIN 3B	GluN3B	TCGGGCCG AGCCTCGG GAA	ACCCGCGC CGTGGTCC CGG	GGACCACG GCGCGGGT GGA	GCCACGGG GCGCAACC ACC	CGGAGGGC GCGTCGGA ACC
NALC N	NALCN	gacgcgggccc cTCACCTA	CCACGCGC AGGAATAG GGA	gcgggccccTC ACCTACGG	CGGCGCTC AGTGAGTG ACA	ACACCCAC GCGCAGGA ATA
UNC7 9	auxiliary subunit of NALCN	GTGCGTTC GCTGGATC CAT	CCCAAACAA GGGGCATC TA	TACTACACA AGTAGCAA GG	TCGGCGGC CGGCGTCC CTC	CATCTAGG GAAGAGCG ACT
UNC8 0	auxiliary subunit of NALCN	CAGAGCTG GGTCCTGC AGT	GCCACAGG AAGGTCTG GAT	TGAAGAGG AAGAGCTC CGA	GGTCCTGC AGTAGGAC TCC	tgtggcgcggcct cagcgg
TPCN 1	Two pore calcium channel protein 1, non-selective Ca^{2+}-permeable channel	GGGTTGCG GCGCAGCA CTC	CGGCGCAG CACTCTGGT GT	CAGGGAGA AGAGCGAG GGA	GCGCCAGG GAGAAGAG CGA	GGTCGCCC TAAGAAGTC GG
TPCN 2	Two pore calcium channel protein 2	TCGGCCCT GGTGAGCC GCC	GCGCCTGC GCAGTGAA GCT	CGGTGTTC TGAGGGCG AGT	AGGGTCGG GTCCAGCG CGT	TCAGAAGCT CAAGCCCC GA

Gene	*Protein*	*gRNA 1*	*gRNA 2*	*gRNA 3*	*gRNA 4*	*gRNA 5*
SLC1A5	SLC1A5 (ASCT2) amino acid transporter	AGGCGGTGGTCTGGTGTCC	TCTGCAGGAGGCTAGGTTC	GTCTGGTGTCCGGGAGTAG	GGCCCCTGTGTACGGAAGG	AGAGCCACGCGGCACGCCC
P2RX7	P2X7 receptor - triggered by extracellular ATP, induces formation of non-selective cation channel	GGCCTGAAGTAGAGCAGAA	GATCCTCGCCTCCTCCCTG	CACAGCCAGCTGGGCGGGA	AGGGAGGCTGTCACCATGC	AGGAATCCCGCTTGTCCTG
HCN1	Hyperpolarization Activated Cyclic Nucleotide Gated Potassium and Sodium Channel 1	CCCGGACCGCAGCCACTAA	CCGCCGCCGCTGCCCTTAG	GCTTCAGCACCAGCCGCAC	ccgcggccgagaagcgcct	AGACGCCGAGGGGCCCCGG
HCN2	Hyperpolarization Activated Cyclic Nucleotide Gated Potassium and Sodium Channel 2	tcgcgcccgggctctcccc	CAACGCCTcggcccggggc	gccgccggccggAGCCCGA	cggcACGAGAACGACACCT	CAGCCCGAACGGCGAGTGC

Gene	*Protein*	*gRNA 1*	*gRNA 2*	*gRNA 3*	*gRNA 4*	*gRNA 5*
HCN3	Hyperpolarization Activated Cyclic Nucleotide Gated Potassium and Sodium Channel 3	GCTCTAGCGGAGGCGTCGT	CAGGAGCGGGTGAAGTCAG	GCAGCCCCGCGGGCTCTAG	GCCCCGCGGGCTCTAGCGG	CGCCCCACCAAGGGACCCC
HCN4	Hyperpolarization Activated Cyclic Nucleotide Gated Potassium and Sodium Channel 4	GGCTCCCGCCGCAACCGAG	GCGCAGCCTGCCCAAGCAT	CCCGCCGGGCTTACATCAG	GCCTCAGGCGCCCATGCTT	GCCCGTCCGGCCCGTCCCG
TRPA1	TRPA1, Transient receptor potential cation channel	TGTGGGCGCGTCATTAGTA	GGTGTGTGCACAATCCAAG	CATTAGTAGGGTCACCTCT	CAGCGAAAAAGTCGCTCTG	CCAGGAGCAAGAATTCGGT
TRPC1	TRPC1	AGGAGCAGAGGATGACGTG	CGTCGCTACAGAGGAGCAG	CTCGAGCCGAGGCAGCAGT	CGTTCGGCgaggaagagga	CTCTGTAGCGACGACACTA
TRPC5	TRPC5, calcium- and sodium-permeable transient receptor	GCGCCGCAAAAGAGGAGTC	CCGGCCAGGATGCGTGGTG	GTGTCGTCTGGATGTCCAC	CAGGGATAGGACAAAGCTG	CTGTGGGCTCAGGGTGGTA

Gene	*Protein*	*gRNA 1*	*gRNA 2*	*gRNA 3*	*gRNA 4*	*gRNA 5*
	potential channel					
TRPM1	TRPM1 - non-selective cation channel	TGCGGGCAGCTGGGCGGAA	GCGGCAGCCCCACACTCGG	CACTGGCCTGGCCACCCGA	GCCTGATTACAGATGTTGG	CATCCCCAAAAGGTTTAGA
TRPM2	TRPM2 - non-selective cation channel	AGTGTAGCGAGCTGGAGAG	TCGGCAACAATGACAAGGT	CCCTTCGGCAACAATGACA	TGGGAGAACAGAACTGGGG	CTGGTTGCAGCTGGCGTGG
TRPM3	TRPM3 - non-selective cation channel	CCGTGGTGTCAGAGACAAG	GCACAAAACAGCCTGTGGT	ACACCTGCAAATTCCATTA	CTGCTTTGACTCCGACCAC	CAGCCCAAGTCCCCAAGTT
TRPM4	TRPM4 - non-selective cation channel	CGCAACCTCCTGCAGCCCA	GGGACAGGAACAAATGTAG	AGTTGACTCCACAGATCCG	ACTCCTCACCCCGGATCTG	AGCATGGTGGTGCCGGAGA
TRPM6	TRPM6 - non-selective cation channel	GCTTGAGCTGAGAATCCGG	CGGAGGGAGAGGAGTTCGG	AGGGAGAGGAGTTCGGAGG	TGAGAATCCGGAGGAGAGA	GGTAGTGTACGCTACTACA
TRPM7	TRPM7 - non-selective cation channel	CGGCCTGTAGCCATCTATC	GGAGACGCTTCCCGATAGA	CCTGTGGCCAGTCACCCGG	CGTCCCGAGAGGACAAATC	CACGGGGCGGACTCCGGAA

Gene	*Protein*	*gRNA 1*	*gRNA 2*	*gRNA 3*	*gRNA 4*	*gRNA 5*
TRPM8	TRPM8 - non-selective cation channel	GAGAGACCAGCAGGATCCT	GATGACATACCCTAAGTGA	CCTGCTGGTCTCTCCCCAC	TGACAAAAACCGTCACTTA	TGTGGGCATAAGCAAATGC
PKD2	TRPP2 - polycystin 2	cggcgggcgcccgggAAGAA	GAAAGGAACATGGCTCCTG	CCTCGGCCGTGAGCTCCGT	AGGCGCACAGCGCCGAGCG	TGGACGTAGAGTGGCGCCC
PKD2l1	polycystin 2 like 1	GGTGCCCACTCTCAGCTAG	GGTCATGCAGCACTACCAT	CATCAGAGGTACCAGATAG	TCTTCCTCTAGCTGAGAGT	GGAGAACTGTCCCCCTATC
PKD2l2	polycystin 2 like 2	GCGGTGAGGGGTCCTCTTA	GTGGCACCGAGGCGGTGAG	CATGGCTGAGGCGTCACGG	CGTCACGGTGGCACCGAGG	GTGTAGTGCAGGTCCGCCA
TRPV1	Transient receptor potential vanilloid 1	AGCGACTCCTGCTAGTGCA	CGGGCCCGGGACCCCACGG	CTCCTTGGAAGCACCTGGG	AGTCGCTGTGGACGCCCTT	GGACTCACCAGCTAGACGC
TRPV2	Transient receptor potential vanilloid 2	CAGCCGGCACGGTGGAGAA	TGGCTAGCCTGTCCTGACA	CCAGATGGTCAGTCTCTGG	CTGGAGCCAGGGTCTGTGT	CACCCTGGCAGCAGAGGAA
TRPV3	Transient receptor potential vanilloid 3	GGCTGGAATGAGGCGTCAG	CAGAGGGATGGCTGGAATG	GGCGGGAAGCTCTCATTGC	TCCCTGGGTCAGCCTCGGG	AGGCCCCCGGGTGGGACTG
SLC4A4	NBC1	CCCCAGCCTCCAACCCCGG	GCGCCGGGCAGCGCTTcgg	AGTTTGGCGGCGGAGTGTG	CCGGGCAGCGCTTcggtgg	GCTGCCGGGAGGGTCGATG
SLC4A5	Sodium Bicarbonate	GTGGAAGTAGCAGCCAGGG	ggattccagacttagggaa	accacatccctgaagagga	agcctaggggtcagtgaca	gttagggctatattatgag

Gene	*Protein*	*gRNA 1*	*gRNA 2*	*gRNA 3*	*gRNA 4*	*gRNA 5*
	Cotransporter					
SLC4A7	Sodium Bicarbonate Cotransporter	TGGCTTTAGTAGGAGAGCG	CGCGCTGCGACTGCTGGGC	TCGTTACCCGGGTGAGTAG	TAGTAGGAGAGCGAGGCCG	CTGCTGGGCTGGCTTTAGT
SLC4A8	Sodium Bicarbonate Cotransporter	GCTGCGAGAGAGTGACCTT	CGAACGGCGACCCCCACCC	CAGAGATGGGCCAGATCCC	CGCGGGCCGGTGGCTATGG	CAAGGGATGCGGCAGAGAT
SLC4A9	Sodium Bicarbonate Cotransporter	TCAGAACCTAGGACTGTAC	GGCAGTCACCCCTCATCTA	TCTGAAGCCAGGGGCCCTC	TGGCAGCTTCATTTCCATG	GAAGCGCTGGGGGGACATAT
SLC4A10	Sodium Bicarbonate Cotransporter	AGCAAGGTGCTTATTCCAG	CAGAGAGATAAGCAGTAAC	GAGATAAGCAGTAACAGGC	TACTAAGCAGAGCGAGTGC	CCAGAGGCGTTACAAAACA
SLC4A11	Sodium Bicarbonate Transporter-Like, Sodium Borate Transporter	GGTCCCCGACGGGAGACGG	GGGCGGGGAGCTCGAAAGT	TGGCACACTCGCGCACTCA	CGCTTCTGGACCCCAAACT	TGCGACTGAGGCAGACCCC
SLC5A1	Sodium/Glucose Cotransporter 1	CTGCCAGGAAGGACCAAGG	GACCGCTGGAAAGTGTAAG	ACAGGCCGGGTGACCGCGG	TGGAGCCCCAAGACCACCG	GCATTGCGAATGAGCTCGT
SLC5A2	Sodium/Glucose	GGCTCGGCACCAGAGATGG	GCAGGCTCGGCACCAGAGA	TCAGCAGGATTGTCAATCA	CCAGAGATGGGGGCCCAGA	GCTAGCACAGTCCCAAAGT

Gene	*Protein*	*gRNA 1*	*gRNA 2*	*gRNA 3*	*gRNA 4*	*gRNA 5*
	Cotransporter 2					
SLC5A3	Sodium/Glucose Cotransporter 3	TTCCTGCACTCCTCGGAgg	CCGCACTCGCCGATCCTCC	TCGCCGCCTGGGAGCCGTC	gcgtgtgcgcggtccggga	GCTGCGCCGGACGGCTCCC
SLC5A4	Sodium/Glucose Cotransporter 4	CCTGCAGCCATGGCCAGTA	GGATGTGGTCAGACAATGG	GGCTCTGGGGTCTCAGCTA	TGTGGTCAGACAATGGAGG	GTGCTGGGGCTAACCGTAC
SLC5A5	Sodium/Glucose Cotransporter 5	GTGGACACCAGGAGCATGA	AGTCCCAGGCTCCGAAGGT	GTCTCCACGGCCTCCATGA	CCGTAGTCCCAGGCTCCGA	ATGGAGGCCGTGGAGACCG
SLC5A6	Sodium/Glucose Cotransporter 6	TTTCCCGCTTCCCTCTACG	CTGATAGCGCATAGCGTCC	CTGCCCGGTCTCCACACGT	AGCGTGAGCCGGTGCCGAG	CTACCCACGTGTGGAGACC
SLC5A7	Sodium/Glucose Cotransporter 7	GCGCAGAGTTGACAGGTGT	CGCAGGAAATGGGTAGAGG	GCAAGAGGCTACAAAGTCT	CCACCACTCCAGGTAGGAG	TCGGCGTCTCCAAGAACCT
SLC5A8	Sodium/Glucose Cotransporter 8	TCTACACAGGGAGCGCTCT	GCGTAGTAGATGCCGATGG	CACCTGAGCAGATGAGAAC	GGAGTGGCCGAGTTCGCCA	GGCGGCCAGCAGACCTCCA
SLC5A9	Sodium/Glucose Cotransporter 9	CAAGGAGCTGGCAGCAATG	gagaggagtcaggagtcgg	GTGAGGCTCAGGGCAACca	CTAGCAGGGGAGGTAGTAG	CCTGGAGCTTCAGGGGACG

Gene	*Protein*	*gRNA 1*	*gRNA 2*	*gRNA 3*	*gRNA 4*	*gRNA 5*
SLC5A10	Sodium/Glucose Cotransporter 10	ATGAGCCCGAGGGACTGAG	CTGCCCAGCTGGAGTCCTT	GGCTGATGGGCCACACCCA	ACACCCAAGGACTCCAGCT	TGGAGGTCGCTGGTGGAGT
SLC5A11	Sodium/Glucose Cotransporter 11	GGCGGGACAGTGGAAGACT	TCACCTGCGTGGGGACCCA	GGGCTGTCAGTGGCTTCTA	ACCCATGGCATGGAGGGGT	TGCGTGGGGACCCATGGCA
SLC5A12	Sodium/Glucose Cotransporter 12	AGCAGACAGCTCTTAGCTA	CCCCCAACCAGGAACTCTC	TGTCAGAGACAAGCCGACA	CTTCCCGAGAGTTCCTGGT	AAGAATCTGGTGGTGGTAT
SLC6A1	Sodium-And Chloride-Dependent GABA Transporter 1	GTCCCCTGGGACACTCGGG	GAGCCACATGAAGGAGCAG	CCCGGCCGCAGGTAGGAAA	TACTGCGCTCCCGACTCCT	CCCCACTGGCCCCGCAAGT
SLC6A2	Sodium-Dependent Noradrenaline Transporter	TGTCTAAGGCGCTCCCGGG	GGCACGCCGAGGCTCTGCT	CCGCCCGAACGCCACACGG	GGCGCCTTGGCAGGCTCTA	GGCAGGGCGCAAGGCACCA
SLC6A3	Sodium-Dependent Dopamine Transporter	ATGCGCCGCACCCCTAGTA	CCCATGTGGCGCTATCGGG	TCCAGGCTCAGAACCGGGT	AAGCCCCCGCGAGATGGAG	AGGCTTCGCGGAACGCTCT
SLC6A4	Na+/Cl-Dependent Serotonin Transporter	GCGCCCTCGAGGCACCCGG	GTGCATGCGCCCCAGCGGT	GCGCCGCCGGGTGCCTCGA	AAGAAACGTGGGTTCGAGG	TCGAGGCGGAGAGGAAAAG

Gene	*Protein*	*gRNA 1*	*gRNA 2*	*gRNA 3*	*gRNA 4*	*gRNA 5*
SLC6A5	Sodium-And Chloride-Dependent Glycine Transporter 2	CACAGGCAACAGACTGAAC	TTAGACGAGAGGAGTGCGG	GAGTTGCTCTGGGTCCTAG	AACAGACTGAACTGGTGGA	GAGCAACTCGCCTCTGTAC
SLC6A6	Sodium-And Chloride-Dependent Taurine Transporter	GGTCCTCGGGGCTCGGCGT	ACAACAGACACGCGAGGTC	GGGATACGGAGGCACATGT	AGCCACCCCAGGTACCGGA	CGACTCTCGGTCCCTTCCG
SLC6A7	Sodium-Dependent Proline Transporter	CCCGGAGCGCAGAGAGCGA	CGCTGCGCAGGGACAGACA	CCGACTCAGCTGGATAACA	CAGAGCCCGAAGCTGGTCT	ACTCAGCTGGATAACAGGG
SLC6A8	Sodium-And Chloride-Dependent Creatine Transporter 1	GCCGCCGCCGGGAAGGAGA	CGGGGAAGAGAGGGATAGT	AGGGATAGTCGGAGCGAGG	ggtcgcggcgccTCACGgg	TGGCCCGCGACTCcggtgg
SLC6A9	Sodium-And Chloride-Dependent Glycine Transporter 1	GCGTGCTGGGTCCGCACCG	GGACCCAGCACGCCTGGGC	GCTGTGGAAGAGCTGCGAG	CGGGGGCTGCAGCATGGTA	CGTCGGTCTGAGTGTTCGG

Gene	*Protein*	*gRNA 1*	*gRNA 2*	*gRNA 3*	*gRNA 4*	*gRNA 5*
SLC6A11	Sodium-And Chloride-Dependent GABA Transporter 3	CGGAGAAGGCGCTGCCCCT	CTGCCCCTGGGCAATGGGA	GCAGCCAGCGCGGCCATGA	GCCAGCGCGGCCATGACGG	CGCGAGGTGCCTGGAGTCG
SLC6A12	Na^+/Cl^- Betaine/GABA Transporter	AGACCGGTGCCCTCCCCGT	ACGGGTATGTGCAGCACAG	TTCTGCGCTGGGAGGAACA	CCTGGGAAGCGAGACTCTG	GCACCGGTCTGGAGACAGT
SLC6A13	Sodium-And Chloride-Dependent GABA Transporter 2	CTGCCAGAGGTCCAGTCAG	TCTGGCAGCAGCTTCACTA	GGAGAAGAATTATCTAAGG	AGGGGAGAAGAATTATCTA	GAGAGAGCCCTAGATTGAG
SLC6A14	Sodium-And Chloride-Dependent Neutral and Basic Amino Acid	TCAGCCAGACTGCAAGAGG	CAGACTGCAAGAGGAGGCG	CAGCCGAGGGAGTGAACCA	CACTCTGGCAGGTAGGAAC	GTGGCTCACTCTGGCAGGT
SLC6A15	Sodium-And Chloride-Dependent Neurotransmitter Transporter NTT73	GCAGCTCAAAAGCCCTGGG	TCTGCCAGGGAAACAGCAC	GTTTCCCTGGCAGACACAC	TGGCAAGCGCCTACGCTAA	TACGCTAAGGGCACAACTG

Gene	*Protein*	*gRNA 1*	*gRNA 2*	*gRNA 3*	*gRNA 4*	*gRNA 5*
SLC6A16	Orphan Sodium-And Chloride-Dependent Neurotransmitter Transporter NTT5	GCGCGCCAGGCAGATCGAG	GATCTGTCGACGCCTGAAG	GCCAGTCGGACAAAAATGA	TACCCCCCACGTAGGACAG	CGGCGCATGCGCAGAGAAT
SLC6A17	Sodium-Dependent Neurotransmitter Transporter NTT4	CGCGGGATTGCGAAGACTG	CCGGCTCTGCGGAGCAGAA	TGAGGACCAAGGTGTGAGG	GGACGAGCGCAGGGTCGGG	GCGCTGCCAGGGCGCAGGG
SLC6A18	Sodium-And Chloride-Dependent Transporter XTRP2	CCAGGCTTCAGGGCAAGGG	GCAGTCTTCTGGGACCTCA	CAGGGTGCACCATTGCCCA	GGCAGAGTCAGTCCCCTCA	GAGACGGCTCTCTAGTGCT
SLC6A19	Sodium-Dependent Neutral Amino Acid Transporter B(0)AT1	CGGCTCCCCAAGCACGGAG	GTGGCTCTGACACAGGTAG	CACCAGCAGCCTAGGAACC	AGCCGTCCAGCGACCACCA	GCCTAGGAACCGGGCACGG
SLC6A20	Sodium/Imino-Acid Transporter 1	CAGGCGCGCCGTCCCACCC	GCCGCAGCCTGGCCAACAA	CAGCTAGCTGCGTCGGCGG	AACCAGCTAGCTGCGTCGG	GTTACAGAACGGCACACTG

Gene	*Protein*	*gRNA 1*	*gRNA 2*	*gRNA 3*	*gRNA 4*	*gRNA 5*
SLC8A1	NCX1	GGAAGCACAAAGCAGGCGG	GGTCGCTCCCATCTTCTGT	TACTAGCGTGGAGGAACGG	CTGGTGCGTCTGGGCGTGA	ACAGCTCCCGATCAGGAAG
SLC8A2	NCX2	CCCAGACACAGGAAGGCGG	GGACCGCCTGGGTACTGGG	CAGAGACCCCTGAGACATG	GCAGAGGTAGAGAGCGCGA	CAGCCGCCCGAGAACCAGG
SLC8A3	NCX3	GTCACCGCGGGAGACGTCT	GCTGCGAGCCCACGAACCC	GGCGCCTCACCGGTCGCAG	CCCTCCCGCCGGGGTTCGT	GACTGACATgccccggacg
SLC9A1	Sodium/Hydrogen Exchanger 1	GTGAAACCGGGAAGCGGCC	GACTGGCTCTCACCCCCTT	GCCCTAGGGATAGAGGAAG	CAGGATAGGGATAGTGCAA	GCGCCGGGCTGAGATTCCG
SLC9A2	NHE2	GAGAGCAGCGCACCGGCAT	GCACGTGCAGGGCGACGAG	CGGCTGGAGAGCAGCGCAC	TGAACGCGCCGAGGGCCAT	CCTAGCCCTGCGAGCGTGG
SLC9A3	NHE3	TGCACGTGGGCCCACTCGA	GTGGCCGCGCGCATCAGGT	AGAGCCGGACTCTcccggg	ATCGGACTGTAGCCGGTAC	TCCAGAGCGCGATGACGTA
SLC9A4	NHE4	GTAGGTAGGAGAAGCCCAC	TCCACACAGGGGTGTAGGT	GCAGTAGCAAACAATTCCA	TGCTCATTCCACAGATCAC	CTCCCCGACTTCAGATGTG
SLC9A5	NHE5	GGCAGCGCGAGCAGGGACA	CTTCGGCCGCCCCCGCCAG	GCTCCCAGGGGAGAAGACA	ccgTGCGGTGCCGGGAGGG	AAATCCTCAGAGCTCCCAG
SLC9A6	NHE6	GCGGCCGCCGGTGAGGTAG	CGGGAGGCGGGGGGAGACA	CAGCCGGCGGGCAGAGAAA	CCCGCCCCTACCTCACCGG	GCCGCCGGTGAGGTAGGGG
SLC9A7	NHE7	GTGCAGAAAGCGCACCCGG	GGCCACTCCGGCAGGTCCG	TGCTGCCAGAACCCGCCGA	GGGTGCTCACCATAGATCA	AGGGCGGGGGGTGTAACAG

Gene	*Protein*	*gRNA 1*	*gRNA 2*	*gRNA 3*	*gRNA 4*	*gRNA 5*
SLC9A8	NHE8	TCCTGGAGGAGGCGGAAGA	GACTGGCTACGTAGGAGGT	CCCGCGGCTCCGAACTCGG	AGGCGACTGGCTACGTAGG	GAGGTGGGTGTGGAGAACC
SLC9A9	NHE9	CCATCTGAATACTAAGCCA	CAGTTTCAACATCAGGGAG	AGGAATCCCAAGAAGACTG	GATAGCAAAGTACCGAAAC	CTTCACAAGCATTCTGCCC
SLC9A10	NHE10	TGTGCAAGTGAGAAGTGGG	GCCCTAGGGGAAAGCTCAC	GCTAACCGGTGCAGACTAG	GAGCAAGTAACTGTCAGTG	ACCAGTGAGCTTTCCCCTA
SLC9A11	NHE11	GGACCTGAAGGGCTACTGG	cctgtgcaaatctatgcag	accagctgaggtgagatac	ggcttggcatgtgactacc	CAAGGACCTGAAGGGCTAC
SLC9B1	Na^+/H^+ Exchanger-Like Domain-Containing Protein 1	AGCCACGCGCCACCCAGGT	TGGCGCGTGGCTTACGCAA	CCTGCGCGGAAGTCTATCC	GGGCTGCGAAAGAAGTTGT	AGAGGAGAGACAATGTCTG
SLC9B2	Na^+/H^+ Exchanger-Like Domain-Containing Protein 2	GAGGCCCCAGAGACACTAA	GCCTGGGTCCGCGCTCTCT	GCGGGTCCGCAGGCTTCTG	AGGCGGGGCCGACTACACG	CTGCAGATAAACGGTCTCA
SLC10A1	Sodium/Bile Acid Cotransporter	CCTGAGAGGTGATTAAAGA	TCAGCCGGAGAACAAGGAG	CGGAGTCAGCCGGAGAACA	GGGGACATGAACCTCAGGT	ATGGCCAGACTGAAGACAT
SLC10A2	Sodium/Bile Acid Cotransporter	ATTATCCAACAAACCCTCG	ACCCAATAGGCCAAGATAT	AGGTGATTGCAGTAGTTAG	CCAGGGACCAGCGCTTCTG	CACTACGGCCTGGAGCGGG

Gene	*Protein*	*gRNA 1*	*gRNA 2*	*gRNA 3*	*gRNA 4*	*gRNA 5*
SLC10A3	Sodium/Bile Acid Cotransporter	GAGGCCGCCTCCCTTCCGG	TAACTGGCAGTGCTAACAG	CCAGAGGCCGCCTCCCTTC	CGATCGCGGAGCAGGGTCG	CCTGACAGGCCGAGCTCGC
SLC10A4	Sodium/Bile Acid Cotransporter	ccccggAGCCCACGACCAG	CCGCGAGGCCGCTGGTCGT	GCGCCGCTGACGTGCTCGG	ACGCCGCCGAGCACGTCAG	GGACACGCCGCTGAACCAC
SLC10A5	Sodium/Bile Acid Cotransporter	TGTTCCAGTGACAGTCTGA	GAAAGAACATTCTTCATGC	TTCGTAGCTTGAACTTACA	TTCAAGCTACGAAAATAAA	TGTGACTATAGAAGAAGCA
SLC10A6	Sodium/Bile Acid Cotransporter	CGCACATCAGGAGACCCTG	TGGTGAGTAAGAACAGAAG	CACAGCTTCCGGATCTCCA	TAATAAACTGTGGTAAGTA	AAAAGGCATGAGCCCAAAC
SLC10A7	Sodium/Bile Acid Cotransporter	AAAGACCTGGGGGTTGCTC	GGCGGCTTTGAGGAGGGTT	GCTCCGGCGGCTTTGAGGA	AGCCGCCGGAGCAACCCCC	AGTAGTAGTAGCCAGTGAC
SLC12A1	NKCC2	ACCAAGGAGCCTTCTTCTG	GCGTCACCCAGGAATATAT	AATGTTCAACTTACCACCA	GTTACATTTCCTCAGAAGA	AGATTCTGAGGAGTAGGTG
SLC12A2	NKCC1	CTAGCCTGGACGGCCACAG	CGGCTGCCGGTGGCCTCTG	CCTCCCGGCGACATCACTG	TCGCGGGCGCAGCATCCTC	CCGACCCCGGCCAGTCCCG
SLC12A3	NCC	CCCCAGGCGTCTCTGTTGT	AAGCGCCCGCTGCACAAAG	TGCACAAAGTGGCGTCCCC	agacgctcctccatcccca	GCCCACAACAGAGACGCCT
SLC13A1	Sodium/Sulfate Symporter	TGTGGAGGACGATGGGCAG	CCTTGGTGTGGAGGACGAT	CTTTGCTGCCTATTCTCAG	TGCCTATCAACTAGATGAG	GCTGCCTATTCTCAGGGGA

Gene	*Protein*	*gRNA 1*	*gRNA 2*	*gRNA 3*	*gRNA 4*	*gRNA 5*
SLC13A2	Na^+/Dicarboxylate Cotransporter 1	CGCCATGGAGCCCAGTCCA	CCAGGAGCTGGGTAACAGA	GGCTAGGTGGGCACACAGT	TAGGAGCGATAGGCCCACA	GCCCAGTCCAGGGCTAGGT
SLC13A3	Na^+/Dicarboxylate Cotransporter 3	GCGGGAGGGCGAAGACCAC	CAGGCGATCGCGCTGATGG	GCGCGATCGCCTGGCGGTA	CCGCGGCAGGTGCAAGGGA	CGCCAGGCGATCGCGCTGA
SLC13A4	Na^+/Sulfate Cotransporter	TCAAGGCAAATTATAAGTA	GGGAAAGGATGATAAACGG	tactaatcaagccgagagg	TGCATGCGGACTTCAGGTG	TGATAAACGGGGgcatagt
SLC13A5	Sodium-Dependent Citrate Transporter	CGGGCATCAGAATGACGAG	GTGACGAACAAGATCACGA	GCCCTGTAAAGAATCTGAG	AGATTCGATTCGGAGCCAG	TGGCGGGCGAGACGAGTGA
SLC20A1	Sodium-Dependent Phosphate Transporter 1	TAGGACGCGCGAGAAGGAG	TCCCAGGAAGCAGCCGCGG	GCAGCCGCGGGGGGTTTCAG	CCGGCAGCCATCACTCCAG	TCGGCCGCTGAAACCCCCG
SLC20A2	Sodium-Dependent Phosphate Transporter 2	CTCACGCTGCCGGCTCCGG	ACTCCGGGGTAAAGAGCCC	TTGAGCCGGAGAGACGCAG	CGCGTGCCGCCTCCGGAGC	GGCGCCGCACGGCAAGCGA
SLC22A2	Organic Cation Transporter 2	CCCGGAGCGAGGCTGAGAG	GCCTCGCTCCGGGCACGTC	GTGGTGGGCATGATCCTGC	TCCAGGACATCGTCCACGG	TGCTCCAGGACATCGTCCA
SLC22A5	Organic Cation/Carnitine	TACATAGGGCGCACGACCA	TAGGGCGCACGACCAGGGA	GTCGCTATCAGGAACACGG	CCCTATGTAAGGCCAGCCG	GCACGACCAGGGAAGGTTG

Gene	*Protein*	*gRNA 1*	*gRNA 2*	*gRNA 3*	*gRNA 4*	*gRNA 5*
	Transporter 2					
SLC22A12	URAT1, Renal Specific Anion/Cation Transporter	GGCTCAGGCCAGCATCCTA	GCAGCTGCTCCAGACCTCC	CCGTGCTGTTGTCCAGGAG	AGAGGGGCCCACTTCACAA	ATTTGGAAAGTAGGGAATG
SLC22A15	Cation Transporter	GCCCAGCGCGGCAACCCCT	AGCGCCTGAGAGGGCGGTG	GCCGGTGCCGGGCGCCCAG	GGCCCGGCCGGCAGCGTCA	CTCCTTCCACCACTCAAGG
SLC22A16	Cation/Carnitine Transporter	GTGGCGGGACCCCATGGTG	TCGAAGTGGCGGGACCCCA	CAGTGCACGGCCGCACCAT	TAACTCGGCGCCCAGTGCA	GTCATAAATCCCCTCGAAG
SLC22A18	Cation transporter, Tumor-Suppressing Subchromosomal Transferable Fragment Candidate Gene 5 Protein	CCTGGAGCGCTCACCCCAC	CACTCCGCTGTGGGAGGTA	GCCGCAGCAGGCACGTCAG	CTTGGGCACGGGTGCCGGT	AGGTAAGGCAGAGCTACTG
SLC22A23	Ion Transporter Protein	TCCGGGAGGCGCCCGAAGT	AGGCTGGGTCCAGAGCTCG	AGAGGCGCATAGAGCGCGG	GGCCATGGCCATAGAccgg	AATACAGCGCGGCCACCCC
SLC23A1	Na^+/L-Ascorbic Acid	GGGCCCAGGAGGACCTCGA	TCCTGAGGGCTCTAGAAGC	AGCAGTTCCTGAGGAGAAG	CAGAAGTCTTGGAGACCAC	ACCTGTGCCCCAAAGATGA

Gene	*Protein*	*gRNA 1*	*gRNA 2*	*gRNA 3*	*gRNA 4*	*gRNA 5*
	Transporter 1					
SLC23A2	Na^+/L-Ascorbic Acid Transporter 2	CGGCTGTCGCGGGGACCGG	GAGGCTGCAGCGGGCACTG	GGCGCCCCCAGAACCCCAC	CTGTCGCGGGGACCGGAGG	GCAGCCAGTGGGGTTCTGG
SLC23A3	Na^+/L-Ascorbic Acid Transporter 3	GCAGCCAAGACAAAGCGAA	GGAGTTGGCTGGGATTGAG	GGAGCCCACTGATCGGAGT	CAAGACAAAGCGAAAGGCA	ATCCTGGGAGCCCACTGAT
SLC24A1	NCKX1	AGGGCAATGCAGAGAGACA	TGAGGCCCATGGGTCAGTG	GAGAATGGGGAGAGATTCA	AGGAAAGAGCCCGAGAATG	TCAGAGGATACGAGAGAGG
SLC24A2	NCKX2	CAGAGCCCGGGCCTCAGAG	CCCGGGCTCTGGCTCGCAC	CCAGCCCGGCTGGCGAGAG	CCCGGGCCTCAGAGCGGGT	CTCTGCGCGTCTCCCCCGA
SLC24A3	NCKX3	GAGCCGCAGCGCCCACTCG	CAGCAGAAGGTCCCTCcgg	GAGTAAGCAGCGCACAGGC	CGAGCCTGCGAGAGCAGAA	CCGGAGCCCCAGGATAAGC
SLC24A4	NCKX4	TCGACGTCGGCCCTCCCAG	CCAGGGGCGAGCTCTCCCC	CAGGCGGTGCGCGACTCAG	CATGGCCCGAGGGCGAGGT	GCCAGAGAGAAAGTTCCCG
SLC24A5	NCKX5	GGCCAAACATGGGCGAGAA	CAGATGTGCAGTGGCCCAC	GACAAAAGGGGGCCAAACA	GCAGGCCTGTGAACAATTT	CTGCCCCAACGTCTCCCAA
SLC24A6	NCKX6/SLC8B1/SLC24A6/NCLX	gcccggacgggaagagtag	TGGCGCAAGGTCGGTCCGG	CGCTGGCGCAAGGTCGGTC	GGCGGGGCACCCGGACTGG	CCAGCGAAGCCGCCAGTCC

Gene	*Protein*	*gRNA 1*	*gRNA 2*	*gRNA 3*	*gRNA 4*	*gRNA 5*
SLC28A1	CNT1, Sodium-Coupled Nucleoside Transporter	TGGATGCTGACAGAAACAA	GCGGGACTGAAGAAAGGAG	CCTGGAGCTGTCCTCGAAG	AGGGCCCACAACGATGTGA	GGTTATAAGCTGCACTGCA
SLC28A2	CNT2	CACAAGCTGGGGTAAGTAA	CACTGATGAGTTCTCTCTG	GAATCAATTCCACAAGCTG	CCCTCTGGCTCCTCAGTGA	GGTAAGTAAAGGTGTTTGG
SLC28A3	CNT3	TGCCAAGGGGCTAAGGAAA	AGGTCCCTGTAACAGCAGG	AAAGCCACCTGCTGTTACA	GGCACAGCTTGCTTCAGTT	CTGAGGGCTACAGCAACGT
SLC34A1	Na^+-Dependent Phosphate Cotransporter 2A	GTTGGGATGTGAGGGTCCT	GCAGCTCAATGAAGCCTCC	CAGATAGGACACAGATGAA	ATGTCAGTCCAGCCAATcg	GTTTCCTACTCAGAGCTGG
SLC34A2	Sodium-Dependent Phosphate Transport Protein 2B	TACACACGCAGGTGACACG	CAGCAGGCTTAGGACGGAG	GGATGTGAAACGAGCGCAG	CTGGTGAGTACCGCCGCCG	GCGCGCACCAGCCAGGCTA
SLC34A3	Sodium-Dependent Phosphate Transport Protein 2C	GGTAGGAGCTCCTAGGACC	CCTCACCACCCACACAGGT	CACACAGGTAGGAGCTCCT	CCCCGATGACACCAGATAG	AGCTCCTAGGACCAGGCTG
SLC38A1	SNAT1, Sodium-Coupled Neutral Amino Acid Transporter	AAGAGCGGGCGCACAGGAG	GCCCCCGTCAGTAAGGGTT	GAGGGTAAAAACCCCGGAA	CTGCCGAGGGTAAAAACCC	GACCGCGCGCGGGACGGGG

Gene	*Protein*	*gRNA 1*	*gRNA 2*	*gRNA 3*	*gRNA 4*	*gRNA 5*
SLC38A2	SNAT2	GGAGCAGCCCTGCGAGCGG	GAAAGGCGTTCTAAGGCGG	GTACTGGAAAGGCGTTCTA	GCTGCTAGCAGTACTGGAA	GTCCGCCGTGTCAAGGGAA
SLC38A3	SNAT3	GGAGCAGAGCGAACCGCAC	CCTCGCGGTTGGGAACGTG	GGCTCGGGCGGCACACCAC	TCCTGAGGCAGGGCCCATG	CGAACCGCACCGGCCCGAG
SLC38A4	SNAT4	AAGTCAGGAAAGCCTGCAC	AAAACTGCAATCAGGACCT	TTTCCTGACTTGTTTGGAA	TATATCTCCAGGTTGATCA	TAAATCAAAGCTGTTACAC
SLC38A5	SNAT5	TCTGGTCCTACCCTCTGTT	GTAGTAGCCAGGCTATTCC	CATGGGCAGCGGCATCCTG	CAGGAGCAGGACCACGACT	GGAGTCCCATagagaccga
SLC38A6	SNAT6	AGAGGCTCGTAGATGGAAC	GACCGACGACTGGAGCGCA	CAGTGAGTACATAATCCTA	TGCCCTGCGCTCCAGTCGT	AGGGGTAGAGGCTCGTAGA
SLC38A7	SNAT7	CTCGGGAAAGAATCCCCCA	GCCCTGAGATAGAAAGGGT	GGAAAGAATCCCCCAAGGT	TGGAGCCCTGAGATAGAAA	TCTCCGGCCACCTACCTTG
SLC38A8	SNAT8	GCGCCCATCGAGGACAGAG	GAGCTGACGCCAAGGAAGC	aaggggaCTAGAAGTCGT	CCCCGGGAAGTGAGTCCTG	GAAAAGCCTCACCCTGCCA
SLC38A9	SNAT9	CCCTCGGGTGAGAGAAGGA	CACGGCGCGCGCTCCTCAA	GTTTGGACTAGGAGCCCCG	GCAATAGCCTGGGTCGCAG	CTGACCCTCGGGTGAGAGA
SLC38A10	SNAT10	GTCACAGGTCCCAACGTCC	GATTCACAGGCGGCCCGCG	GAATCTCCGAGCCCAGACC	CCGCGGCGGCAGCTGAGTT	TCTGGGCTCGGAGATTCAC
SLC38A11	SNAT11	CCCCAAGATCTCTAGGCTG	TTGTCTGGGCGAACTCCGG	CTGCAGCCCCAAGATCTCT	GCCACAGCCTAGAGATCTT	CATTTGTCTGGGCGAACTC

Gene	*Protein*	*gRNA 1*	*gRNA 2*	*gRNA 3*	*gRNA 4*	*gRNA 5*
HIF1a	Hypoxia-Inducible Factor (HIF)-1 alpha subunit	CTGGCCGAAGCGACGAAGA	CCTCCTGTCCCCTCAGACG	CGGCTCCGAGCCTCTCCTC	CACAGTGCTGCCTCGTCTG	CTCCTCAGGTGGCTTGTCA
HIF2a	Hypoxia-Inducible Factor (HIF)-2 alpha subunit	GGCCGCCTCAGGAGCGCTG	GACACTGCCGAGGATTGTA	GAGGCGGCCGTACAATCCT	GGCGGGTGGTGAAGGTCCG	CGCCCCAGCGCTCCTGAGG
SLC16A3	Essential gene for MDA-MB-231 cells	CGGGGAGGCCACCCATACA	GAGGCCACCCATACAGGGA	GGAGCGGACCggcagaggc	CGGCGGCCAAGCCCGGTCC	CAGGGCGCGGAGCCACCTG
AP2B1	Essential gene for MDA-MB-231 cells	CTGGGTCGGAGACCGGCGG	CGGAGAGAAGGGTAACACC	TGCCAGGGACAAAGATGGT	AGAGCCTGGAGGCCGTGGG	TGTGGCAGCAGGTAGTTGG
NAMPT	Essential gene for MDA-MB-231 cells	GTCACTGCTCGGTCGGCGG	TGACTTAAGCAACGGAGCG	CGGCCCGAGATGAATCCTG	CTGCCGCAGGATTCATCTC	AGCCGCGCCAGGGAGCTCG
FKBP9	Essential gene for MDA-MB-468 cells	GGCGGAGCTAGGGGAGGTC	CGGGTAGGGCCAGGAGACC	CTGGGCAGCGGAAGAAGGG	GATCTGGGCAGCGGAAGAA	GCGCTCGGGCGGCACGGGT
GNB2	Essential gene for MDA-MB-468 cells	CGACAGTGGAGGACACGAG	CACGAGGGGTGCTCCCCGG	CAACTTCCGAGGGAGCAAG	GCGCTGTCTTCCTCCgcgg	GCGGCGCTGTCTTCCTCCg

Gene	***Protein***	***gRNA 1***	***gRNA 2***	***gRNA 3***	***gRNA 4***	***gRNA 5***
GNG5	Essential gene for MDA-MB-468 cells	CGGCCACGGTTCAACCCAG	CCAAGGGAGGTAGAGACGG	CGGAGGAGGACCGGAATGT	GGAAGTGAGGGGAGATACT	CCGGCGGCGGGTGACCAGG
	Negative control scrambled guides	GCGCTGACGTACGTAGCAT	TTTTTAGAAGCAAGTACTC	GCGGTCGACGTTGTAAGGA		